Università degli Studi di Padova
Dipartimento di Fisica ed Astronomia Galileo Galilei
Corso di Laurea Magistrale in Fisica

Master thesis

Development of a multivariate technique based trigger for the selection of D^{*+} meson at LHCb

Advisor: Prof. Donatella Lucchesi
Co-advisor: Dr. Silvia Amerio

Student: Emanuele Michielin

Academic year 2013 2014

Contents

List of Figures

List of Tables

Introduction

Studies of heavy flavor physics observables have provided critical input to the Standard Model (SM), which is one of the most successful physics theories concerning electromagnetic, strong and weak interactions. However, there are phenomena that call into question its completeness such as the dominance of matter in the universe with respect to the antimatter, the physics motivation of the three generations and what determines the hierarchy of quark masses. These are all issues associated with the heavy flavor sector. Physicists have thus developed many possible extensions of the SM in order to explain these discrepancies.

To test the truthfulness of these extensions and to search for new physics beyond the SM, particle physics experiments have been built through recent years. The Large Hadron Collider (LHC), the world's largest and most powerful particle accelerator, has pushed the limits in both energy and instantaneous luminosity.

This thesis has been developed within the Large Hadron Collider beauty (LHCb) experiment, which is one of the four detectors located at the LHC. LHCb is a particle detector, designed with the aim to observe and study decays of mesons and baryons containing b and c quarks and make precision measurements of their properties. b and c quark system are sensitive, through quantum loop processes, to energy scales well beyond the center of mass energy of LHC. In particular, the study of D mesons offers a unique opportunity to access up-type quarks in flavour-changing neutral current (FCNC) processes. It probes scenarios where up-type quarks play a special role, such as supersymmetric models with alignment [1][2]. Moreover, the neutral D system is the latest and last system of neutral mesons where mixing between particles and anti-particles has been established. The mixing rate is consistent with, but at the upper end of, SM expectations [3] and constrains many New Physics models [4]. More precise $D^0 - \bar{D}^0$ mixing measurements will provide even stronger constraints.

Therefore, large quantity of data is needed to test the predictions of the SM at a much higher precision. Since each event detected by LHCb has a size of about 60

kBytes and the maximum sustainable input rate for the acquisition system in 2012 was 300 MB/s[5], not all events produced in proton-proton interaction can be saved to tape for off-line analysis. Moreover most of the events are only background. This forces the development of an on-line selection system, which has to select and collect physically meaningful events at a set rate. The decision on whether to keep or discard any given event is made by the so called trigger system.

The aim of this thesis is to implement a new and more powerful algorithm to select events with D^{*+} meson, which has to replace the current D^{*+} trigger.

The first chapter presents the physics motivation and the formalism for measurements in the D^0 system. These are two of the most considerable analyses that will exploit the events collected using this trigger.

Chapter 2 introduces the LHCb detector, with a brief description of each sub-detector and an overview on the whole LHCb trigger, from the hardware Level 0 to the software High Level Trigger, where the algorithm developed in this thesis will be implemented.

For the selection of the events with a $D^{*\pm}$ the $D^{*\pm} \to D^0(\bar{D}^0)\,\pi^{\pm}$ channel is exploited. It is followed by a subsequent D^0 decay in two, three or four bodies. This trigger line has to be inclusive. It first reconstructs a two-tracks vertex consistent with decay of the D^0, but allowing for missing particles. The D^0 vertex is then combined with the π coming from the D^* decay to reconstruct the whole event. This allows for efficient selection of a broader decays modes, including modes with neutrals particles for which a full reconstruction is impossible. The third chapter describes in details the reconstruction strategy, the current trigger and the whole trigger strategy thought for this new line.

Chapter 4 focuses on the trigger implementation. The background and the signal samples used are presented. The first step of the selection criteria is a set of loose preliminary cuts. The motivation and effects of these on the variables distributions are shown. This chapter explains also the bulk of the trigger line: the use of a multivariate technique to separate the background from the signal events. The motivations for the particular multivariate tool, its training and the results are discussed.

The trigger performance and rate are presented in Chapter 5. These are compared to the current inclusive D^{*+} trigger performance. Some studies on the variables distributions of the selected events are also described.

The last Chapter summarizes the project developed through this thesis and presents the future prospects.

Chapter 1

The Standard Model and D physics

The purpose of any physics experiment has always been to observe natural phenomena and attempt to understand them. This understanding takes the form of a mathematical theory to describe the underlying physical mechanisms, which can then be used to predict future behaviour. In the 1960s and 1970s the first high energy particle accelerator experiments gave light to a plethora of newly observed particles and phenomena. Consequently, through the effort of many theoretical physicists, the 1970s gave birth to the mathematical theory that describes these observations: what has come to be known as the Standard Model of particle physics (SM) [6].

The Standard Model (SM) of particle physics is a mathematical description of the fundamental particles and their interactions. It is one of the most successful physics theories in history. The results of almost every particle physics experiment are consistent with its predictions. The most impressive example is probably the measure of the electron g-factor, where the concordance between experiment and theory is at the level of 10^{-13} [7]. However, there are phenomena that call into question its completeness, such as the dominance of matter in the universe with respect to the antimatter, the physics motivation of the three generations and what determines the hierarchy of quark masses.

In this context, studies of flavour physics observables have provided critical input in the construction of the Standard Model. Flavour measurements provided the first indications of the existence and nature of the charm quark [8], the third generation and the high mass scale of the top quark. Also in searching for physics beyond the Standard Model flavour observables will play a central role. Currently particular attraction is given by the opportunity to make measurements of CP-violating asymmetries with much

higher precision than has been ever possible. In particular, a field which could lead to an extension of the SM is the CP-violation in the D mesons system.

The LHCb experiment at the Large Hadron Collider (LHC) is designed to perform this kind of studies [9]. In this thesis an on-line selection system for the selection of events with the production of a D^{*+} meson at LHCb is developed. This system is necessary to collect and provide data for the analyses concerning the charm sector, such as studies on mixing and CP-violation of the D^0 system.

In this chapter, after a brief overview of the constituents of the SM in section 1.1, a more detailed description of the theory of the CKM matrix and CP-violation is given in the second section. The theory behind the mixing and the CP-violation of the D^0 system is then discussed in section 1.2.1.

1.1 The Standard Model constituents

The Standard Model (SM) is a gauge theory, a type of field theory in which the Lagrangian is invariant under a continuous group of local transformations, which successfully explains the dynamics of elementary particles. There are several different species of elementary particle, as shown in Figure 1.1. Each has a specific set of quantum numbers that determine how particles of that type interact with other particles. There are twelve spin-$\frac{1}{2}$ matter particles (fermions), divided into two groups: quarks and leptons. For each of the quarks and leptons there is a corresponding anti-quark or anti-lepton, with the same mass but opposite quantum numbers. One of the natural phenomena that the SM cannot explain is that quarks and leptons have three generations. The particles in each generation are identical except in their masses.

There are two leptons in each generation: one massive particle with electric charge -1 and one neutral particle with very little mass called neutrino. In the first generation there are the electron (e^-) and the electron neutrino (ν_e). The second and third generations consist of the muon (μ^-) and tau (τ^-) and their corresponding neutrinos (ν_μ and ν_τ). Lepton also has a flavour quantum number: the lepton-number. It is conserved in all interactions, excluding neutrino oscillations.

Similar to the leptons, there are two quarks in each generation: one up-type quark with electric charge $+\frac{2}{3}$ and one down-type with electric charge $-\frac{1}{3}$. These names come from the first, lightest generation, which consists of the up (u) and down (d) quarks. The second generation consists of the charm (c) and strange (s) quarks, and the third generation the top (t) and bottom (b) quarks. They also carry colour charge which takes three values: red, blue and green.

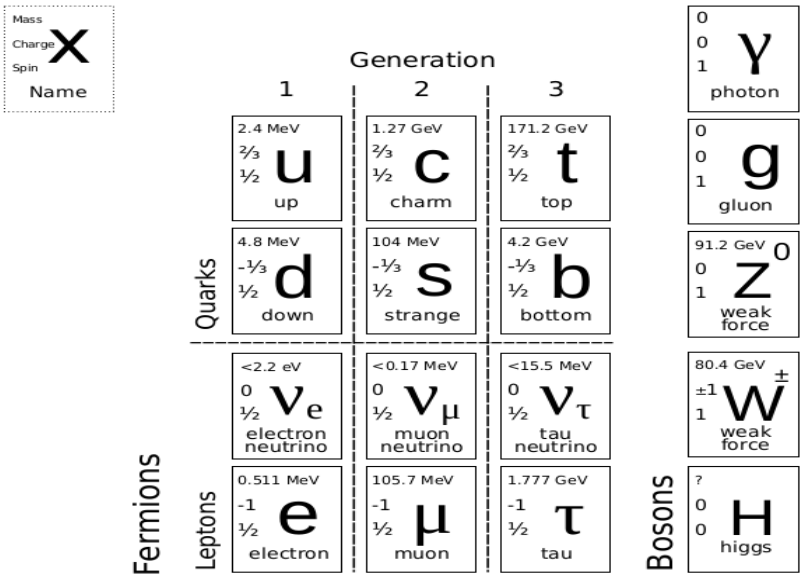

Figure 1.1: Fundamental particles of the Standard Model, showing their masses, electric and spin [10].

Quarks also have a flavour quantum number. This is isospin for the first generation, charm and strangeness for the second, topness and beauty for the third. Unlike the leptons in the SM, quark flavour is not strictly conserved in all interactions, and it is this aspect of the quark sector that makes it so interesting to study.

Three forces describe the interactions between fermions: weak force, strong force and electromagnetism. The interactions between fermions are transmitted via the exchange of spin-1 force mediators (bosons), but only if the fermions possess the type of charge associated with the given force. The strong interaction is mediated by gluons, which act on colour charge. The electromagnetic force is mediated by the photon, which acts on electric charge. The weak force is mediated by the $W^{\pm}$ and Z^0 bosons, which act on weak isospin and weak hypercharge. Quarks carry all three types of charge, so they can take part in all three interactions. The charged leptons can interact via the weak or electromagnetic interactions, and the neutrinos interact only weakly.

In their simplest form, the symmetries of the SM indicate that interactions should be identical regardless of which generation of fermion is involved. However this is not to be the case, due to the differing masses of the fermions in each generation and of the $W^{\pm}$ and Z^0 bosons. Thus the Higgs boson was proposed as an addition to the perfectly symmetric SM [11]. The Higgs boson breaks the gauge symmetry of the SM through

the Spontaneous Symmetry Breaking mechanisms (SSB) and via Yukawa interaction gives rise to the different masses of particles. On 4 July 2012, it was announced that a previously unknown particle with a mass between 125 and 127 GeV/c^2 had been detected by Atlas and CMS[12][13]. By March 2013, the particle had been proven to behave, interact and decay in many of the ways predicted for the Higgs boson of the Standard Model. It was also confirmed to have positive parity and zero spin [14], two fundamental attributes of a Higgs boson.

The bosons of the SM, and the exchanges of quantum numbers that they perform, can be represented as gauge groups. These describe the underlying symmetries, which transitions between states are allowed or forbidden and thus how the elementary particles interact. The whole Standard Model is described as a non-abelian theory with the symmetry group $SU(3)_C \times SU(2)_I \times U(1)_Y$. $SU(3)_C$ is the symmetry group for the strong interaction, $SU(2)_I \times U(1)_Y$ is the symmetry group of the electroweak interaction. This results in the conservation of the charges C (colour), I (weak isospin), and Y (weak hypercharge). Since the electric charge is derived from the weak hypercharge and the third component of weak isospin, $Q = Y + I_3$, it is also conserved.

1.2 Mixing and CP-violation in the charm sector

Symmetries play an important role in physics since they limit the possible terms which enter the Lagrangian and may be associated with conservation laws. CP violation is the violation of the combined conservation laws associated with charge conjugation (C) and parity (P) by the weak nuclear force. Before 1950s it was assumed that C and P were exact symmetries of elementary processes, namely those involving electromagnetic, strong, and weak interactions. A series of discoveries from the mid1950s caused physicists to alter significantly their assumptions about the invariance of C and P. An apparent lack of the conservation of parity in the decay of charged K mesons into two or three π mesons prompted the theoretical physicists C. N. Yang and T. D. Lee to examine the experimental foundation of parity itself. In 1956 they showed that there was no evidence supporting parity invariance in weak interactions [15]. Experiments conducted the next year verified decisively that parity was violated in both nuclear and pions beta decays [16]. Moreover, they revealed that charge conjugation symmetry was also broken during these decay processes.

The discovery that the weak interaction conserves neither C nor P separately, however, led to a quantitative theory establishing combined CP as a symmetry of nature. But further experiments, carried out in 1964, demonstrated that the electrically neutral

K meson, which was thought to break down into three π mesons, decayed a fraction of the time into only two such particles, thereby violating CP symmetry [20].

The phenomenology of CP violation is also nowadays particularly interesting since it could reveal the presence of physics beyond the Standard Model, as it actually did when it was firstly discovered. In particular the neutral D system is the only neutral meson system that mixes and consists of up-type quarks. It therefore provides a unique window on Flavour Changing Neutral Currents (FCNC) between up-type quarks, which can be affected by new physics in a very different way than those in down-type quarks, such as investigated in the $B^0_{s,d}$ and K^0 systems.

1.2.1 D^0 system physics

The D mesons were discovered in 1976 by the Mark I detector at the Stanford Linear Accelerator Center [18][19]. They are the lightest mesons containing a single charm quark, thus they must change the charm quark into a quark of another type to decay. Such transitions violate the internal charm quantum number, and can take place only via the weak interaction. This is the reason why they are often studied to gain knowledge on the weak interaction.

The D^0 system is interesting to analyze as a test of the SM and the Cabibbo Kobayashi Maskawa (CKM) mechanism, as CP-violation is predicted to be $O(10^{-13})$. Signs of significantly greater CP-violation than what is predicted by the SM could be achieved through contributions of additional, non-SM particles to the mixing and decay amplitudes.

The CKM matrix

The CKM is a unitary matrix which contains information on the strength of flavour-changing weak decays. This matrix was introduced for three generations of quarks by Makoto Kobayashi and Toshihide Maskawa, adding one generation to the matrix previously introduced by Nicola Cabibbo.

As introduced in previous section, the Yukawa couplings gives rise to the fermions mass. To take in account the different masses among the generations the couplings for each generation can be properly chosen. However, the Yukawa couplings can be expressed as matrices in flavour space and any non-zero off diagonal elements of the Yukawa matrices gives rise to mixing between the generations.

As the interactions of particles of one generation are the same as those in any other generation the fermion kinetic Lagrangian term is invariant under unitary rotations

between generations. Thus, one can rotate the flavour eigenstates to give the mass eigenstates, which correspond to the diagonalized Yukawa matrices. Consequently, the states with definite mass, in which the quarks propagate, are generally superpositions of those with definite flavour, in which the quarks interact.

Considering only the first two generations of quark, the most general 2×2 unitary matrix can be written as

$$\mathbf{V_C} = \begin{pmatrix} e^{-i\phi_1} & \\ & 1 \end{pmatrix} \begin{pmatrix} cos\,\theta_C & sin\,\theta_C \\ -sin\,\theta_C & cos\,\theta_C \end{pmatrix} \begin{pmatrix} e^{-i\phi_2} & \\ & e^{-i\phi_3} \end{pmatrix} \tag{1.1}$$

where θ_C is the Cabibbo angle, which determines the level of mixing between the two generations. The crucial point here is that the three phases $\phi_{1,2,3}$ can be eliminated by rotating the basis of the u, d, and s quarks respectively. Then the mass eigenstates of the d and s can be expressed as

$$\begin{pmatrix} d' \\ s' \end{pmatrix} = \mathbf{V_C} \begin{pmatrix} d \\ s \end{pmatrix} \tag{1.2}$$

where d' and s' are flavour eigenstates. θ_C has been measured to be (13.04 ± 0.05) [17], thus the mixing between d and s is large, but not maximal.

When the third generation is included the mixing matrix becomes:

$$\begin{aligned} \mathbf{V_{CKM}} &= \begin{pmatrix} cos\,\theta_{12} & sin\,\theta_{12} & 0 \\ -sin\,\theta_{12} & cos\,\theta_{12} & 0 \\ 0 & 0 & 1 \end{pmatrix} \begin{pmatrix} 1 & 0 & 0 \\ 0 & cos\,\theta_{23} & sin\,\theta_{23} \\ 0 & -sin\,\theta_{23} & cos\,\theta_{23} \end{pmatrix} \begin{pmatrix} cos\,\theta_{13} & 0 & sin\,\theta_{13}e^{-i\delta} \\ 0 & 1 & 0 \\ -sin\,\theta_{13}e^{i\delta} & 0 & cos\,\theta_{13} \end{pmatrix} \\ &= \begin{pmatrix} c_{12}c_{13} & s_{12}c_{13} & s_{13}e^{-i\delta} \\ -s_{12}c_{23} - c_{12}s_{23}s_{13}e{-i\delta} & c_{12}c_{23} - s_{12}s_{23}s_{13}e^{i\delta} & s_{23}c_{13} \\ s_{12}s_{23} - c_{12}c_{23}s_{13}e^{i\delta} & -c_{12}c_{23} - s_{12}s_{23}s_{13}e^{i\delta} & c_{23}c_{13} \end{pmatrix} \end{aligned} \tag{1.3}$$

where $\theta_{12} = \theta_C$, $c_{ij} = cos\theta_{ij}$ and $s_{ij} = sin\theta_{ij}$. The current measurements of the mixing angles and the complex phase are [17]

$$\theta_{13} = (0.201 \pm 0.011),\ \theta_{23} = (2.38 \pm 0.06),\ \delta = 1.20 \pm 0.08. \tag{1.4}$$

The matrix can also be written

$$\mathbf{V_{CKM}} = \begin{pmatrix} V_{ud} & V_{us} & V_{ub} \\ V_{cd} & V_{cs} & V_{tb} \\ V_{td} & V_{ts} & V_{tb} \end{pmatrix} \tag{1.5}$$

with $|V_{ij}|^2$ gives the probability of a transition $i \to j$. The Cabibbo-Kobayashi-Maskawa matrix parameterizes the mixing between three quark generations, and as a result it has nine parameters, five of which are relative phases between the quark states which can be factored out. This leaves four independent parameters, one of which complex. This allows for the phenomenon of CP-violation.

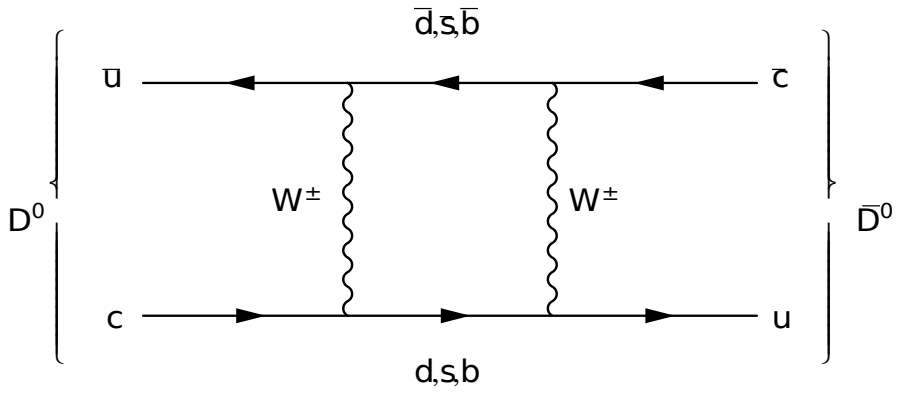

Figure 1.2: One of the dominant diagrams contributing to D^0 mixing.

Mixing in D^0 system

The efficient selection of a large dataset of charm candidates is needed for the study on the D^0 mixing, one of the most active research fields in charm physics. As they are neutral they can transform into their anti-particle via charged weak interactions, as shown Figure 1.2. Mixing in the D^0 system is relatively small and has only been observed in recent years. In 2007 both the Babar and Belle collaborations report of the evidence for $D^0 - \bar{D}^0$ mixing [21] [22]. At the end of 2007, the CDF collaboration found evidence for D^0 mixing in a different environment but in the same decay channel as Babar [23].

The latest analysis carried out by the LHCb collaboration measures the charm mixing parameters from the decay-time-dependent ratio of $D^0 \to K^+\pi^-$ to $D^0 \to K^-\pi^+$ rates and the charge-conjugate ratio [24]. The analysis uses data corresponding to $1\,\text{fb}^{-1}$ integrated luminosity from $\sqrt{s} = 7\,\text{TeV}$ pp collisions recorded by LHCb during 2011 and $2\,\text{fb}^{-1}$ from $\sqrt{s} = 8\,\text{TeV}$ collisions recorded during 2012. The neutral D flavor at production is indeed determined from the charge of the low-momentum pion π_s in the flavor-conserving strong interaction decay $D^{*\pm} \to D^0(\bar{D}^0)\pi_s^\pm$. The $D^{*+} \to D^0(K^-\pi^+)\pi_s^+$ process is denoted as right sign (RS), and $D^{*+} \to D^0(K^+\pi^-)\pi_s^+$ is denoted as wrong sign (WS).

Mixing occurs when an initially defined state of $\left|D^0\right\rangle$ or $\left|\bar{D}^0\right\rangle$ will evolve with time into a mixture of D^0 and $\bar{D}^0$. The time evolution can be described by an effective weak

Hamiltonianin the time dependent Schrodinger equation:

$$i\frac{\partial}{\partial t}\begin{pmatrix} D^0(t) \\ \bar{D}^0(t) \end{pmatrix} = (M - \frac{i}{2}\Gamma)\begin{pmatrix} D^0(t) \\ \bar{D}^0(t) \end{pmatrix} \tag{1.6}$$

where M and Γ are mass and decay width matrices. The solutions of the Schrodinger equation are the mass eigenstates

$$|D_{1,2}\rangle = p\left|D^0\right\rangle \pm q\left|\bar{D}^0\right\rangle \tag{1.7}$$

for some constants p and q such that $|p|^2 + |q|^2 = 1$. They are linear combinations of the flavor eigenstates D^0 and $\bar{D^0}$ The mass eigenstates, $|D_1\rangle$ and $|D_2\rangle$, propagate independently in time with their own lifetime $\Gamma_{1,2}$ and mass $M_{1,2}$,

$$|D_{1,2}(t)\rangle = e^{i(M_{1,2}-i\frac{\Gamma_{1,2}}{2})t}\,|D_{1,2}(t_0)\rangle \tag{1.8}$$

The ratio $x = 2\frac{(M_1-M_2)}{\Gamma_1+\Gamma_2}$ and $y = \frac{(\Gamma_1-\Gamma_2)}{\Gamma_1+\Gamma_2}$ are related to the difference in lifetime and mass of the mass eigenstates. These variables are referred to as mixing parameters and are the observables to be measured. The probability I to find the state $\left|D^0\right\rangle$ from a state $\left|D^0\right\rangle$ after a time t is

$$I(D^0 \to D^0, t) = |\left\langle D^0 \,\middle|\, D^0(t)\right\rangle|^2 = \frac{e^{\Gamma t}}{2}[cosh(y\Gamma t) + cos(x\Gamma t)] \tag{1.9}$$

and the one to find a $\left|\bar{D}^0\right\rangle$ is

$$I(D^0 \to \bar{D}^0, t) = |\left\langle \bar{D}^0 \,\middle|\, D^0(t)\right\rangle|^2 = \frac{e^{\Gamma t}}{2}\left|\frac{q}{p}\right|^2 [cosh(y\Gamma t) + cos(x\Gamma t)] \tag{1.10}$$

Thus mixing will occur if either the mass difference x or the lifetime difference y of the two states is non-zero.

The fit to the decay-time evolution of the WS/RS ratio is shown in Figure 1.3 (solid line). The measured x^2 value is $(-0.09 \pm 0.13) \times 10^{-3}$ and $y = (7.2 \pm 2.4) \times 10^{-3}$. To evaluate the significance of this mixing result, they determined the change in the fit χ^2 when the data are described under the assumption of the no-mixing hypothesis (dashed line in Figure 1.3). Under the assumption that the χ^2 difference, $\Delta\chi^2$, follows a χ^2 distribution, $\Delta\chi^2 = 86.8$ which corresponds to a p-value of 5.7×10^{-20}, which excludes the no-mixing hypothesis at 9.1 standard deviations. This is the first observation of $D^0 - \bar{D}^0$ oscillations in a single measurement. The measured values of the mixing parameters are compatible with and have substantially better precision than those from previous measurements.

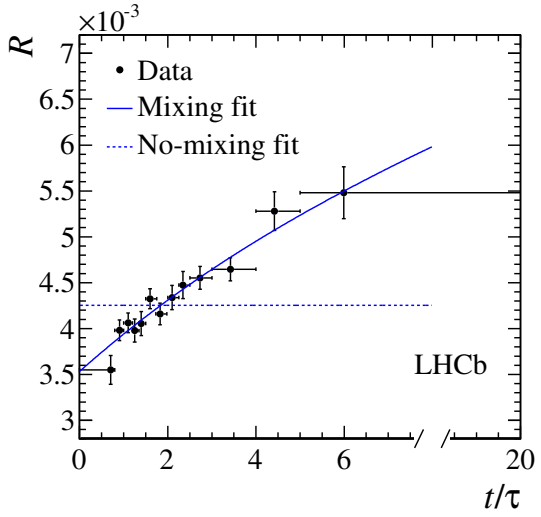

Figure 1.3: Decay-time evolution of the ratio, R, of WS $D^0 \to K^+\pi^-$ to RS $D^0 \to K^-\pi^+$ yields (points) with the projection of the mixing allowed (solid line) and no-mixing (dashed line) fits overlaid.

CP-violation in D^0 system

Performing the same calculation made in previous section for an initial state of pure $\bar{D}^0$ one finds that

$$I(\bar{D}^0 \to D^0, t) = |\left\langle D^0 \,\middle|\, \bar{D}^0(t)\right\rangle|^2 = \frac{e^{\Gamma t}}{2}\left|\frac{p}{q}\right|^2 [cosh(y\Gamma t) + cos(x\Gamma t)] \tag{1.11}$$

thus, comparing with Eq. 1.10, if

$$\left|\frac{q}{p}\right| \neq 1 \tag{1.12}$$

then

$$I(D^0 \to \bar{D}^0, t) \neq I(\bar{D}^0 \to D^0, t) \tag{1.13}$$

which constitutes CP-violation in the mixing rates, the indirect CP-violation. This type of CP-violation was the first of any to be discovered, and was observed by Christenson, Cronin, Fitch and Turlay in 1964, in the K^0 system [20].

While CP is conserved by electromagnetic and strong interactions, the symmetry is violated in weak interactions. In the SM, CP violation is accommodated by the complex phase in the CKM matrix, leading to $V_{ij} \neq V_{ij}^*$. There are two more different types of CP violation in addition to the CP-violation in mixing: the CP violation in decay (direct

CP violation), which occurs when the amplitude for a decay and its CP conjugate have different magnitudes and CP violation in the interference between mixing and decay.

For what concern CP-violation in D^0 system, lots of studies are still ongoing. In most analyses to tag the flavour of the D^0, i.e. to check if it is a D^0 or a $\bar{D}^0$, it is exploited the charge of the π_s of the $D^{*\pm} \to D^0(\bar{D}^0)\pi_s^{\pm}$ decay, as for the already introduced mixing analysis.

In CP-violation in $D^0 \to h^+h^-$ decays, where h can be either a pion or kaon, the parameter A_Γ gives access primarily to indirect CP violation:

$$A_\Gamma = \frac{\tau_{eff}(\bar{D}^0 \to h^+h^-) - \tau_{eff}(D^0 \to h^+h^-)}{\tau_{eff}(\bar{D}^0 \to h^+h^-) + \tau_{eff}(D^0 \to h^+h^-)} = \frac{1}{2}(A_m + A_d)ycos\phi - xsin\phi \qquad (1.14)$$

where τ_{eff} is the effective lifetime and

$$A_m = \frac{|q/p|^2 - |p/q|^2}{|q/p|^2 + |p/q|^2} \quad A_d = \frac{|A_f/\bar{A}_f|^2 - |\bar{A}_f/A_f|^2}{|A_f/\bar{A}_f|^2 + |\bar{A}_f/A_f|^2} \quad \phi = arg\left(\frac{q}{p}\frac{\bar{A}_f}{A_f}\right) \qquad (1.15)$$

with $A_f(\bar{A}_f)$ the amplitude of the $D^0(\bar{D}^0)$ meson decaying to the given final state. The latest results published by LHCb [26] for the study on indirect CP-violation with K^+K^- and $\pi^+\pi^-$ as final states are

$$A_\Gamma^{KK} = (-0.35 \pm 0.62 \pm 0.12) \times 10^{-3} \qquad A_\Gamma^{\pi\pi} = (0.33 \pm 1.03 \pm 0.14) \times 10^{-3} \qquad (1.16)$$

Thus, no evidence for indirect CP-violation is found. Also in direct CP-violation there is no evidence for CP-violation.

The ultimate goal of mixing and CP violation measurements in the charm sector is to reach the precision of the SM predictions. This requires large samples of charm events and measurements in several decay modes in order to distinguish enhanced contributions of higher order SM diagrams from eff ects caused by new particles. The online selection developed in this thesis aims at collecting inclusive samples of D^* mesons with higher efficiency and purity with respect to the current trigger, increasing the physics potential of LHCb in the charm sector.

Chapter 2

The LHCb detector

2.1 The Large Hadron Collider

The Large Hadron Collider (LHC) [27] is a synchrotron particle accelerator located at the European Organization for Nuclear Research (CERN) [28] near Geneva. LHC is housed in the tunnel that was once home to the Large Electron Positron(LEP) collider at a depths ranging between 45 m and 170 m. It is a 27 km circumference ring and it is part of a chain of accelerators at CERN designed to accelerate and collide bunches of protons.

The key figures of merit for such a particle accelerator are: the center-of-mass energy ($\sqrt{s}$) obtained as the total amount of energy available to create new particles in a single collision and the instantaneous luminosity ($\mathcal{L}$) delivered, which is the flux (the number of particles crossing a unit of area per unit time) of the circulating particles. The LHC is designed to operate at $\sqrt{s} = 14\,\text{TeV}$, with a bunch crossing rate of 40 MHz, and maximum $\mathcal{L}$ of $10^{34}\,cm^{-2}s^{-1}$. LHC has provided collisions at $\sqrt{s} = 7\,\text{TeV}$ throughout 2010 and 2011, operated at a bunch crossing rate of 20 MHz, and obtained a maximum $\mathcal{L}$ of about $3.65 \times 10^{33}\,cm^{-2}s^{-1}$ [29]. The $\sqrt{s}$ has been increased to 8 TeV for the 2012 run. After a shut-down period to allow to upgrade the LHC, from 2015 the $\sqrt{s}$ will be increased to 13 TeV, to be then finally increase up to the designed 14 TeV.

The proton bunches, prior to the injection into the LHC ring, are passed through a series of older, lower energy accelerators. The full acceleration chain is shown in Figure 2.1. At the start of the LHC injector chain is a cylinder of hydrogen gas which acts as a source of protons, produced by ionising the gas. The protons are fed into the LINear ACcelerator 2 (LINAC2) where they reach an energy of 50 MeV before they are injected into the Proton Synchrotron Booster (PSB). Once the protons reach an energy of 1.4 GeV

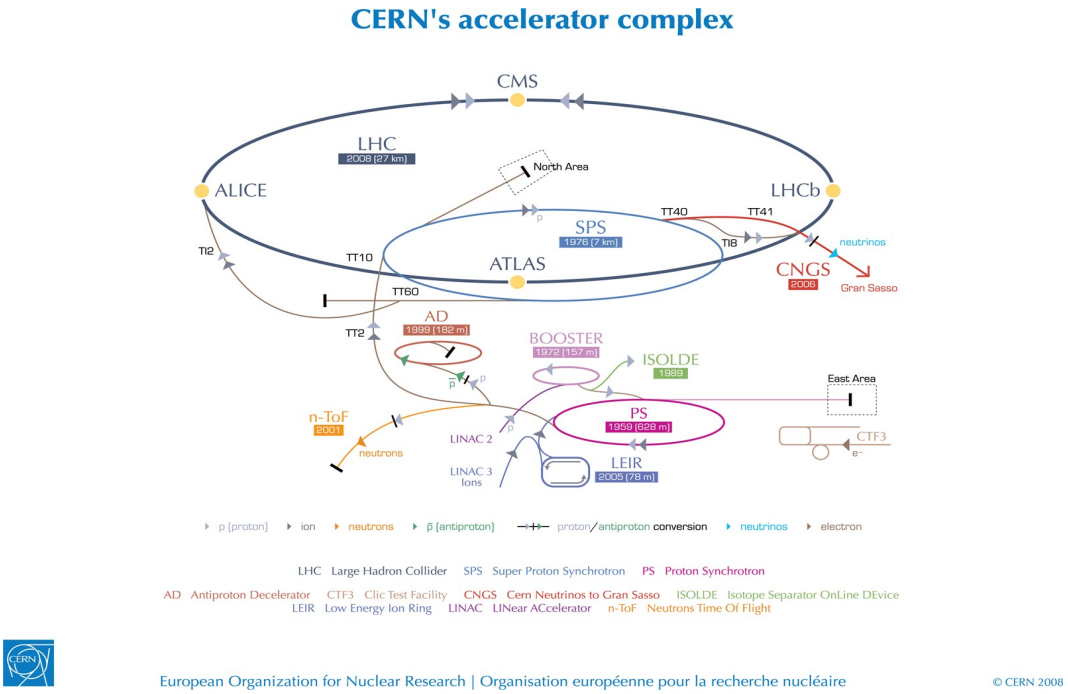

Figure 2.1: The CERN accelerator complex.

they are fed into the Proton Synchrotron (PS) followed by the Super Proton Synchrotron (SPS) where they are accelerated to energies of 25 GeV and 450 GeV respectively. They are then injected into the LHC in two counter rotating beams, where they are steered and accelerated by a total of 1232 superconducting dipole magnets up to a maximum energy of 7 TeV per beam. The protons complete their long journey when they are brought to collide at one of the four intersection points where the two beam lines cross.

It is at these intersection points that the four main LHC experiments are placed to record the remains of the collisions. The Compact Muon Solenoid (CMS) [30] and A Toroidal LHC ApparatuS (ATLAS) [31] are general purpose detectors. The LHC can also accelerate and collide lead nuclei. A Lead Ion Collision Experiment (ALICE) [32] is designed to examine such collisions, specifically looking for and examining the nature of the exotic state of matter known as quark-gluon plasma. The final of the four main LHC experiments is the LHC beauty detector (LHCb) [33]. This thesis has been developed within this experiment, and so this detector is described in detail in the following section.

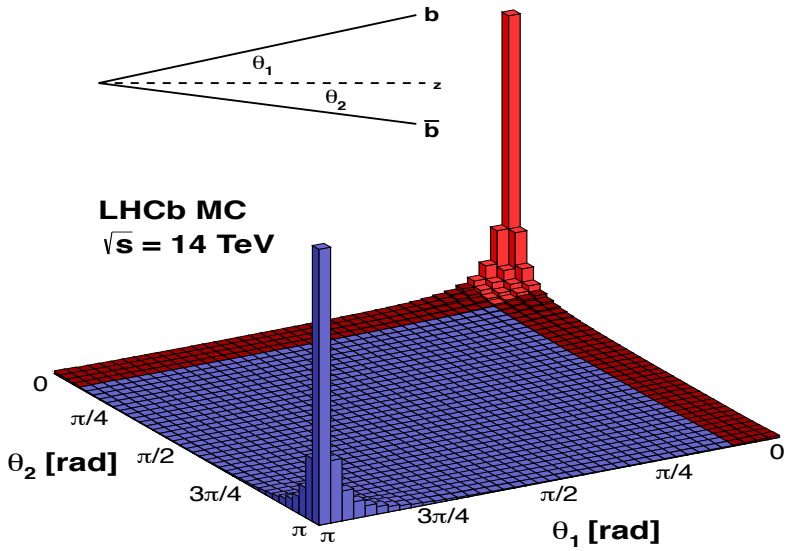

Figure 2.2: The production angles, relative to the beam-line, of bb pairs produced in proton-proton collisions at the LHC at $\sqrt{s} = 14\,\text{TeV}$.

2.2 The LHCb detector

The Large Hadron Collider Beauty (LHCb) experiment is designed to take advantage of the copious production of B mesons at the LHC. Because $b\bar{b}$ pairs are produced predominantly with highly correlated trajectories and are so highly boosted at LHC energies, the polar angles relative to the beam-line tend to be very small, as shown in Figure 2.2. To take advantage of this, the LHCb detector has its unique forward-arm design, as shown in Figure 2.3. LHCb covers only the region of high pseudo-rapidity, $1.6 < \eta < 4.9$, where $\eta = -ln(tan(\frac{\theta}{2}))$ and θ is the polar angle from the beam-line. About 27% of b quarks produced in LHC collisions fall within the acceptance of LHCb.

At LHCb it is advantageous to run with a much lower luminosity with respect to the one provided by LHC, of about $4 \times 10^{33}\, cm^{-2}s^{-1}$, which can be achieved by defocussing the beams. At this value, the probability of having only one inelastic pp collision dominates the probabilities of multiple interactions. This leads to a cleaner environment (or lower track multiplicity) allowing for more precise reconstruction of multi-body decays.

To facilitate a clear frame of reference when discussing the LHCb detector a global

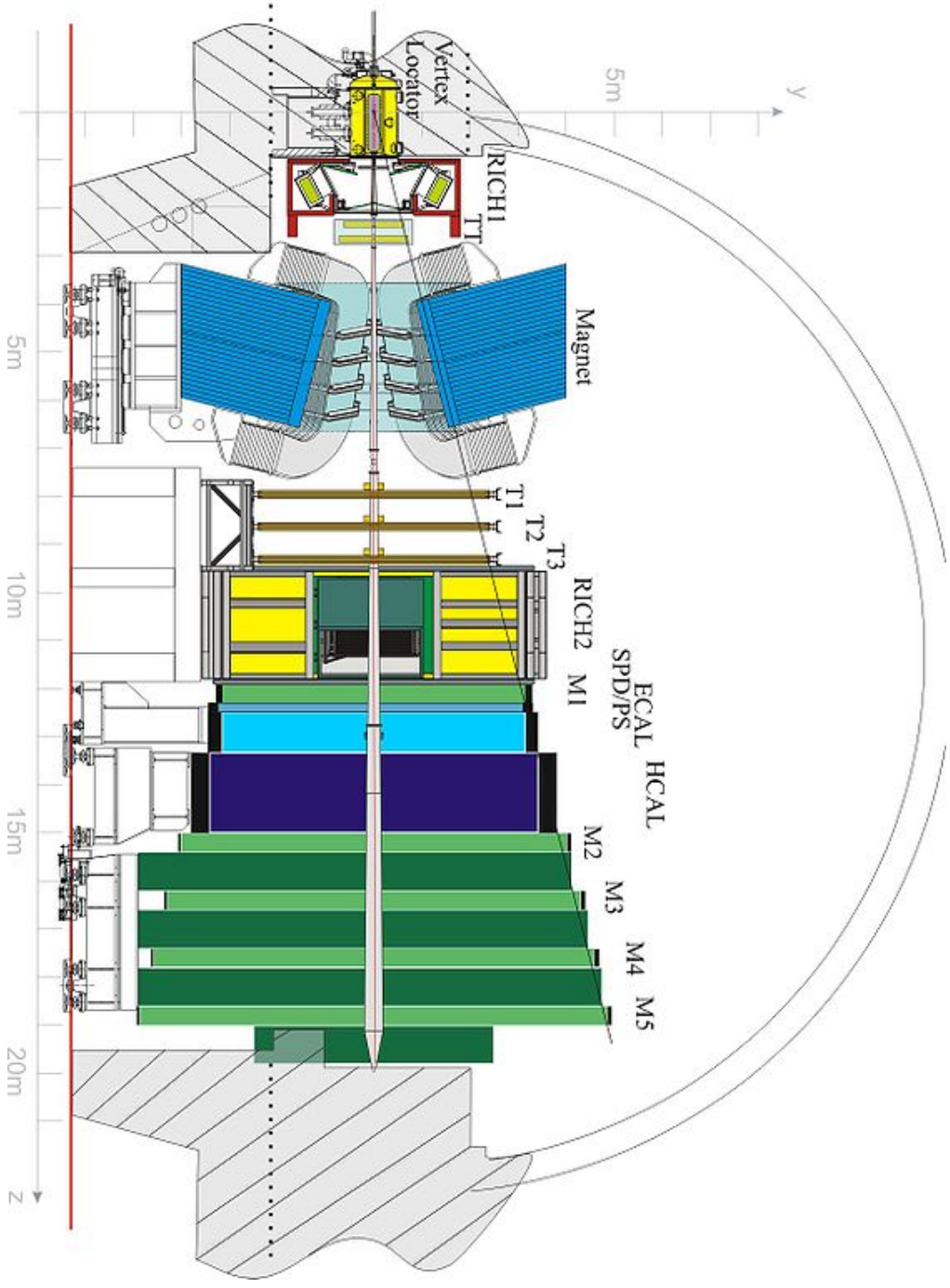

Figure 2.3: A side view of the LHCb detector.

coordinate system is defined, and it is also shown in Figure 2.3. The origin is located at the point at which the two LHC proton beams intersect each other and the protons collide. The z-axis is parallel to the line of the proton beams, with positive z pointing into the main LHCb detector, also called the downstream region. The y-axis is in the vertical direction, with positive y pointing upwards, and the x-axis is horizontal, with positive x pointing into the page.

As Figure 2.3 shows, LHCb is comprised of different sub-detectors, each designed for a precise purpose. The design and performance of each of these sub-detectors are here briefly discussed in turn, with particular attention paid to the tracking system. It is comprised of the VErtex Locator (VELO), the Tracker Turicensis (TT) and the Outer and Inner Tracker (OT and IT). The trigger line here developed exploits the information coming from these sub-detectors.

2.2.1 VErtex LOcator

The LHCb VErtex LOcator (VELO) [34] is a silicon microstrip vertex detector designed to provide precise track coordinate measurements close to the interaction region. As its name suggests, it is used to locate the position of any proton-proton collisions within LHCb, known as primary vertices (PV), as well as the decay points of any long lived particles produced in the collisions, such as B and D mesons, known as secondary (SV). Identifying displaced decay vertices is of great importance to the LHCb trigger, including to the D^{*+} trigger which exploits the long lived D^0.

The VELO consists of two sets of 21 modules, located on either side of the beam line (see Figure 2.4). To minimise the extrapolation distance between the first hit of a reconstructed track and the interaction point the active regions of the VELO sensors start at just 8 mm from the beam-line. Each module comprises two semicircular sensors (one R sensor and one ϕ sensor), each approximately 300 µm in thickness and with a diameter of 84 mm. The R sensors are embedded with silicon in concentric semicircles centred on the beam axis, allowing for determination of the r coordinates of track points. The orthogonal coordinates are supplied by the ϕ sensors in which the silicon strips run radially out from the beam axis.

During LHC injection, the width of the beam increases significantly. Therefore it is necessary to horizontally retract each half of the VELO by ~ 3 cm to avoid damage to the sensors. Once the beam is stable, the aperture reduces to ~ 100 µm and the two halves are moved back together so that they overlap slightly in order to ensure coverage of the full azimuthal acceptance and to aid with module alignment. A vacuum is maintained within the VELO to minimise interactions before charged particles reach

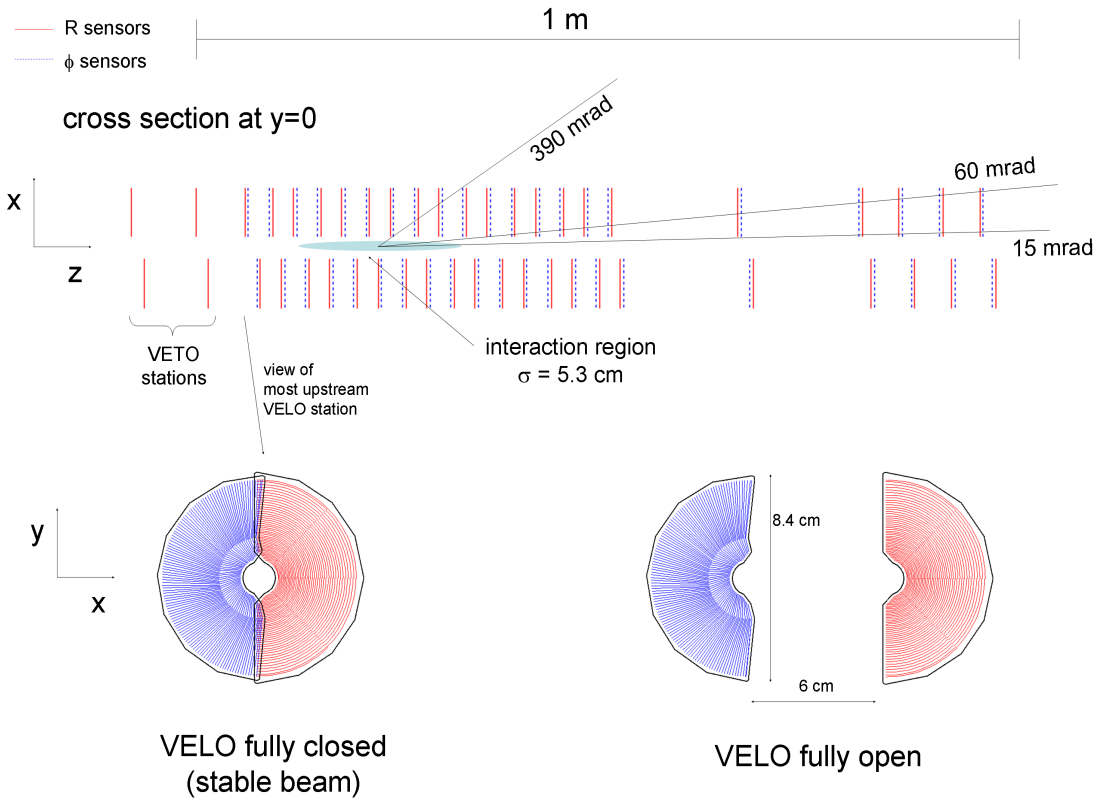

Figure 2.4: The layout of the VELO modules and sensors. The R sensors, which measure the radial position of hits, are shown in red, while ϕ sensors, which measure the azimuthal angle of hits, are shown in blue.

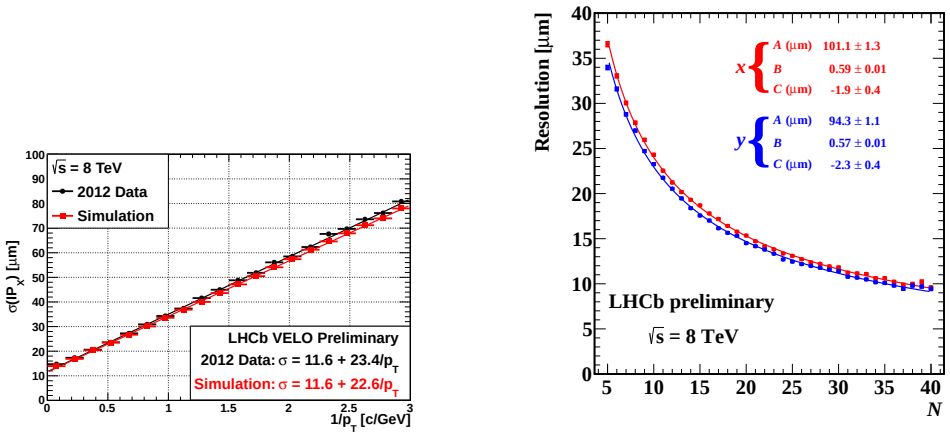

(a) (b)

Figure 2.5: (a) Resolution of the x component of IP measurements as a function of p_T. (b) Resolution of PV x and y coordinates as function of the number of hits

the silicon microstrips.

VELO performance

The performance of the VELO is of critical importance to the majority of LHCb analyses. The spatial resolution of the impact parameter and of the primary vertex in the x and y direction are shown in Figure 2.5. The impact parameter (IP) resolution improves with increasing particle momentum. The resolution on the x component of IP achieves a resolution on IP_x of $< 36\,\mu$m for particles with $p_T > 1\,\text{GeV}/c$. The excellent IP resolution is reflected in the PV resolution. For a PV using 25 tracks in its fit the resolution on the x coordinate of its position is just 13.1 µm, while the resolution on the y coordinate is just 12.5 µm.

2.2.2 The dipole magnet

The dipole magnet at LHCb [35] provides an integrated magnetic field of about 4 Tm in order to displace the trajectories of charged particles and allow their momenta to be measured. A diagram of the magnet is shown in Figure 2.6. It is a warm (not superconducting) magnet consisting of two identical, saddle shaped aluminum conducting coils positioned symmetrically above and below the beam-line. Its polarity can readily be reversed, so as to cancel any asymmetries in the detection efficiency that might fake CP-violation. Throughout data-taking in 2010 and 2011 this has been done regularly,

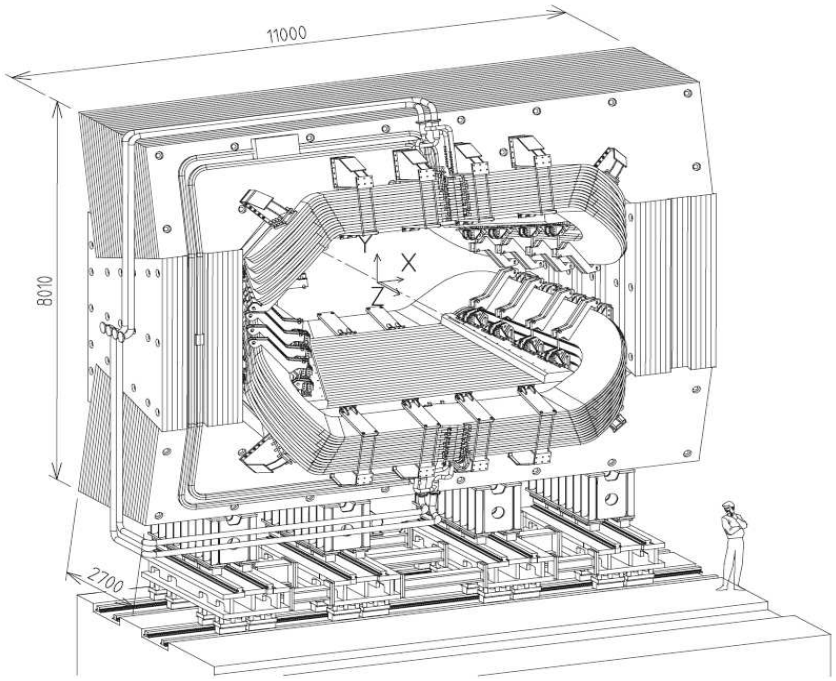

Figure 2.6: A diagram of the LHCb magnet.

and an approximately equal quantity of data has been taken with each polarity.

2.2.3 Tracking system

The tracking stations downstream of the VELO serve to provide measurements of the trajectories of charged particles before and after the magnet, to allow measurement of their momenta. There are four stations: the TT, positioned before the magnet, and T1, T2 and T3 downstream of the magnet. The TT and the inner regions of T1-T3 are subject to very high particle flux, thus they must be very radiation hard, and have sufficiently high granularity as to keep occupancies low enough for reliable pattern recognition. For these reasons they consist of silicon strip sensors. They are collectively referred to as the Silicon Tracker (ST), with the inner regions of T1-T3 alone known as the Inner Tracker (IT). The outer regions of T1-T3, known as the Outer Tracker (OT), suffer significantly less irradiation, and so cheaper straw tube drift-time sensors are used.

The Tracker Turicensis (TT) [36] is a planar tracking station, 150 cm wide and 130 cm high, covering the full angular acceptance of LHCb. It consists of four planes of silicon strip sensors with an (x-u-v-x) layout, shown in Figure 2.7; the x layers have their detection strips aligned vertically, while the u and v layers have theirs rotated

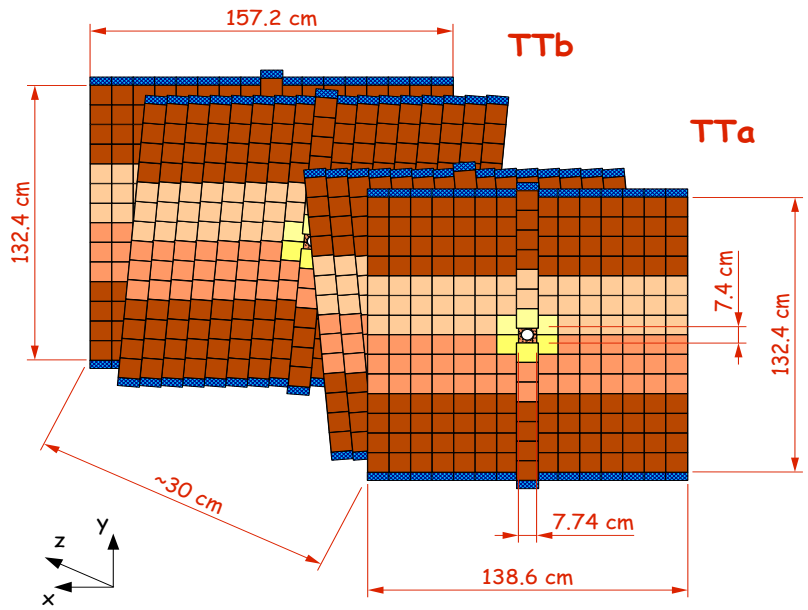

Figure 2.7: The layout of the four detection layers of the TT.

through -5 and $+5$ to the vertical respectively.

The Inner Tacker (IT) [37] makes up the inner region of the three downstream tracking stations T1-T3. The sensors are arranged in a cross shape, 120 cm wide and 40 cm high, about the beam-pipe. Each station has four layers with the same (x-u-v-x) layout as the TT.

The Outer Tracker (OT) [38] is a drift tube detector which completes the coverage of the stations T1-T3. The boundary with the IT is chosen to limit the occupancy to less than 10% at the nominal LHCb luminosity. The four layers of each OT station follow the same geometry as the IT with the inner two layers rotated by $+5$ and -5 . To ensure a maximum drift time of 50 ns (the time taken for two bunch proton crossing), the tube contain a gas mixture of 70% argon and 30% carbon dioxide, and have an inner diameter of 4.9 mm.

Tracking System performance

The track segments found in the VELO are then combined with those in the TT and T1-T3 . The knowledge of the magnetic field is used to estimate the curvature of the particle trajectories as they traverse the detector and thus provide a momentum measurement.

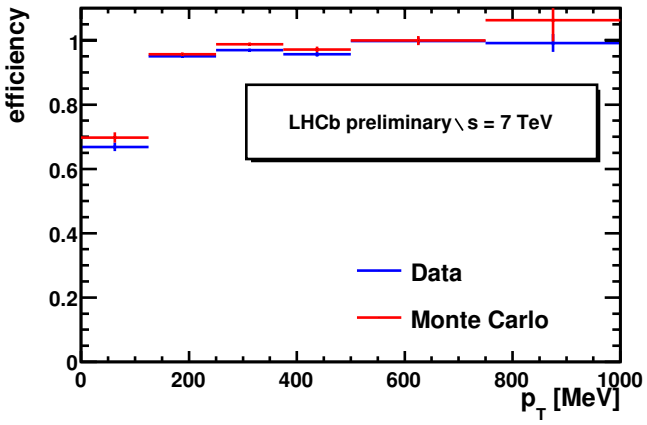

Figure 2.8: Tracking efficiency measured with $K_s^0 \to \pi^+\pi^-$ decays as a function of track transverse momentum.

The ST has achieved a hit resolution of 58 µm, while the OT has a hit resolution of 230 µm [39]. Further, the full tracking system has achieved its target momentum resolution of $\sigma(p)/p = 0.4\%$. The resulting distribution for tracks crossing the whole tracking system is shown in Figure 2.8, where it is compared to the Monte Carlo prediction.

2.2.4 Particle identification

One essential design feature of the LHCb detector is its ability to distinguish different final state charged particles. This is especially important for discriminating between decays that are topologically equivalent but differ only by the species of their final state charged particles. Particle IDentification (PID) is achieved at LHCb by the use of two Ring Imaging CHerenkov (RICH) detectors, a calorimeter system and a muon detector, designed to cover all of the common charged particles (e, μ, π, K, p).

Ring imaging Cherenkov detectors

The two Ring Imaging Cherenkov (RICH) detectors at LHCb provide particle identification for the experiment. To do this they exploit the phenomenon of Cherenkov radiation, whereby a charged particle traversing a dielectric material (radiator) at a velocity greater than the local speed of light in that material emits photons. These photons are produced at an angle to the particles trajectory that is dependent on its velocity, v:

$$\cos\theta_c = \frac{c}{nv} \tag{2.1}$$

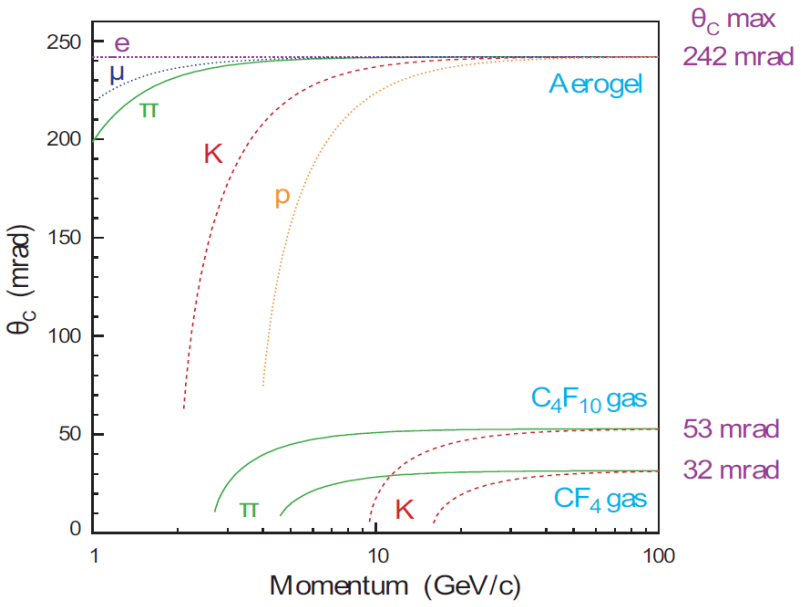

Figure 2.9: The Cherenkov angle of photons produced by different particles in different radiators, as a function of the particle momentum.

where c is the speed of light in vacuum, and n is the refractive index of the material. They are thus emitted in a cone around the particle as it traverses the material, and can be observed as a ring when they intersect a photo-sensitive surface. For a given p each different species of charged particle will produce a ring with a different radius.

There are two RICH detectors in LHCb as shown in figure 2.3: RICH1 [40] is positioned before the magnet and is designed to perform particle identification (PID) for low momentum particles; RICH2 [41] is situated downstream of the magnet, and is designed to perform PID for high momentum particles. The momentum range covered depends on the radiator material used: RICH1 uses aerogel, with $n = 1.03$, and C_4F_{10} gas, with $n = 1.0014$; while RICH2 uses CF_4 gas, with $n = 1.0005$. Figure 2.9 shows the dependence of θ_c on particle momentum for the different radiators and species of particle. Figure 2.10 shows schematics of RICH1 and RICH2.

For a given p each different species of charged particle will produce a ring with a different radius. Thus knowing the p of a given track, one can compare the expected rings with the photons observed and so infer the species of the particle that made the track.

Such a process has a certain rate of mis-identification, whereby it identifies a track as being of a certain species other than its true identity. The efficiency of the PID algorithm

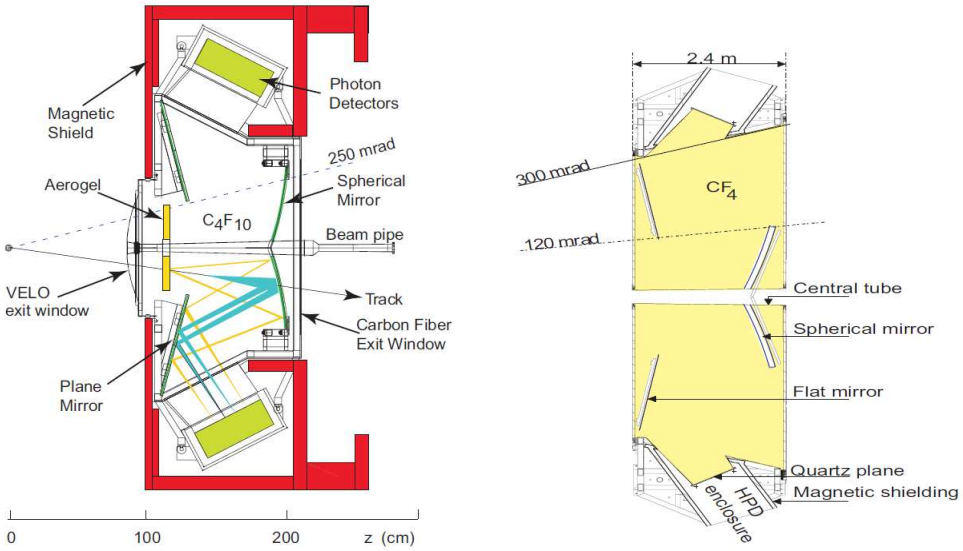

(a) (b)

Figure 2.10: (a) The RICH1 detector in the x-y plane. (b) The RICH2 detector in the x-z plane (top view).

can be checked, on real data, by using decay channels for which the kinematics of the decay products are sufficient to identify them without using the RICH detectors. As an example, the decay $D*+ \to D^0(K\pi)\pi^+$ is used for $\pi - K$ separation, as applying a tight constraint on $m(D^{*+}) - m(D^0)$ is sufficient to select a very clean signal sample. Figure 2.11 shows the efficiency, as a function of momentum, of correctly identifying a K as a K, and wrongly identifying a π as a K.

2.2.5 Calorimeters

The LHCb calorimetry system [42] adopts the classical layout of an Electromagnet Calorimeter (ECAL) followed by a Hadronic Calorimeter (HCAL). The calorimeters are designed to measure the energy and location of photons, electrons and hadrons, providing information for the Level-0 trigger and, ultimately, PID. Two additional sub-detectors, the Scintillating Pad Detector (SPD) and Pre-Shower (PS) are placed before the ECAL to help reject pion backgrounds for signal photons and electrons.

The SPD and the PS are two almost identical planes of scintillator pads, separated by a 15 mm thick lead converter, equal to 2.5 radiation lengths. The role of the SPD is to detect charged particles, and when used together with the ECAL, provides rejection of π^0 and γ backgrounds to e^- signal candidates. In addition, SPD information is used

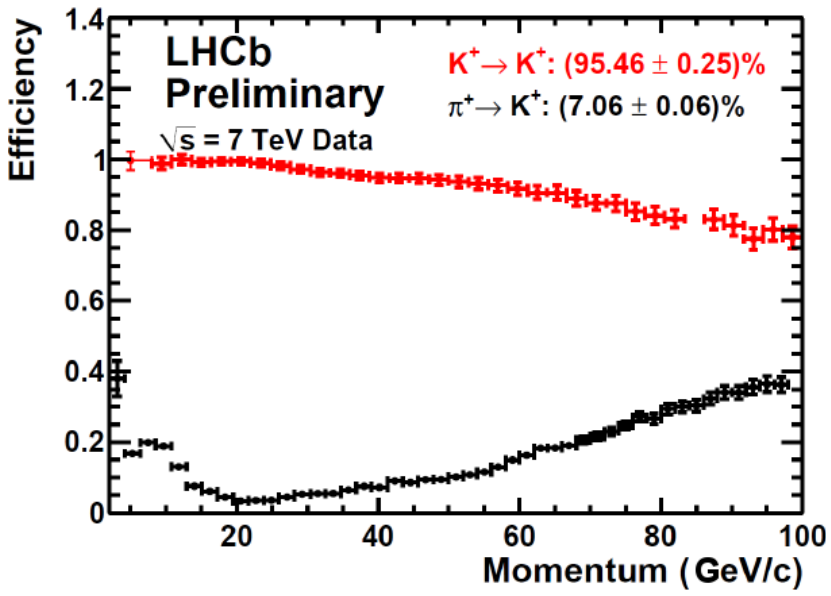

Figure 2.11: The efficiency, as a function of particle momentum, with which the RICH detectors correctly identify a K as a K, and wrongly identify a π as a K.

by the Level-0 trigger to reject high multiplicity events. The PS is designed to detect electromagnetic particles which shower in the lead plate (primarily e^- and γ because of their comparatively short interaction lengths) and is used in conjunction with the ECAL to reject $\pi^\pm$ backgrounds to e^- signal candidates.

The ECAL is comprised of 66 layers, each of which incorporates a 2 mm thick lead absorber and 4 mm thick scintillator tile. The total thickness of the ECAL is 25 X_0 so that it can fully contain electromagnetic showers.

The HCAL is formed of alternating layers of iron absorber and scintillator. However, unlike the ECAL, the scintillator tiles and iron absorbers run parallel to the beam axis instead of perpendicular to it, each with a length corresponding to the hadron interaction length in steel. Figure 2.12 shows a comparison between the internal structures of the HCAL and ECAL sub-detectors.

Calorimeters performance

Using test beam data, the energy resolution of the ECAL is determined to be

$$\frac{\sigma_E}{E} = \frac{9\%}{\sqrt{E}} \oplus 0.8\% \tag{2.2}$$

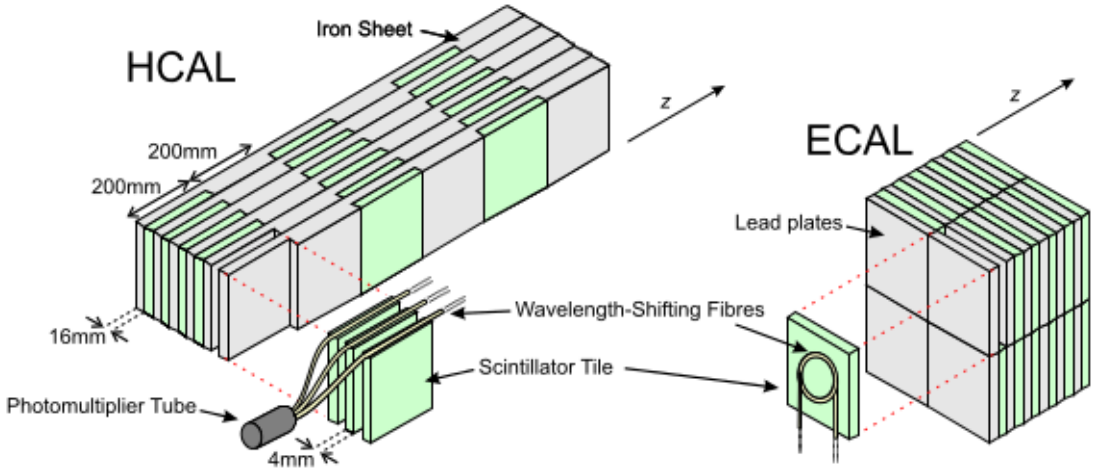

Figure 2.12: The internal structure of the HCAL (left), and ECAL (right).

where E is measured in GeV and $\oplus$ represents the sum in quadrature. For the HCAL, the energy resolution is measured as

$$\frac{\sigma_E}{E} = \frac{69\%}{\sqrt{E}} \oplus 8\% \tag{2.3}$$

2.2.6 Muon chambers

Five muon stations [57] (M1-M5) are used to provide reconstructed muon tracks. Muon detection is vital for any analyses which contain one or more muon. The most notable, perhaps, is the search for the flavour changing neutral current decay $B_s \to \mu^+\mu^-$. In addition, the muon stations are used to search for high transverse momentum tracks for the Level-0 trigger. The M1 station is placed before the calorimeters, while the stations M2-M5 are located after the calorimeter. To reach the M5 station, a muon must have a momentum of at least 6 GeV/c.

All of the muon stations use Multi-Wire Proportional Chambers (MWPC), except for the inner region (R1) of M1 (where the particle flux is too high) which employs triple-GEM (Gas Electron Multiplier) detectors, chosen because of their higher radiation tolerance. Both types of chamber use a mixture of $Ar - CO_2 - CF_4$ gas.

Muon system performance

The layers in each muon chamber are taken as a logical OR to determine the presence of a muon. In doing so the GEMs achieve an efficiency of more than 96%, while the MWPCs achieve an efficiency of more than 95%. The correct PID rate is $> 95\%$ and the

mis-ID rate is just a few % for all momenta, demonstrating the excellent performance of the muon system.

2.3 Trigger system

Due to the high collision rate provided by the LHC only a fraction of events reconstructed in LHCb can be retained. The decision of whether to keep or discard any given event is made by the trigger system. LHCb trigger is organized in three levels: the Level-0 (L0) trigger, and the High Level Triggers HLT1 and HLT2. These are operated in a logical AND mode, such that only events passing L0 are processed by HLT1, and only events passing HLT1 are processed by HLT2. Events failing any of these stages are discarded, while those that pass all three are sent to permanent storage.

In what follows, the term signal refers to a combination of tracks that form the off-line reconstructed and selected b or c hadron candidate. To determine the trigger efficiency, trigger objects are associated to signal tracks. The criteria used to associate a trigger object with a signal track are as follows. An event is classified as TOS (Trigger on Signal) if the trigger objects that are associated with the signal are sufficient to trigger the event. An event is classified as TIS (Trigger Independent of Signal) if it could have been triggered by those trigger objects that are not associated to the signal. TIS events are trigger unbiased except for correlations between the signal candidate decay and the rest of the event, for example when triggering on the other candidate in the event and subsequently looking at the momentum distribution of the signal candidate. The efficiency to trigger an event on the signal alone, ε_{TOS}, is given by $\varepsilon_{TOS} = N_{TIS\&TOS}/N_{TIS}$, where N_{TIS} is the number of events classified as TIS.

2.3.1 Level 0 hardware trigger

The LHC bunch crossing frequency is 40 MHz. LHCb detector at nominal luminosity will see events with at least one visible interaction at a rate of 14 MHz. The purpose of the L0 trigger [44] is to reduce the rate to 1 MHz at which the entire detector is be read out. The L0 trigger reconstructs and selects particles with high transverse momentum in the muon chambers or with high transverse energy in the calorimeter system. It also provides the possibility to veto events which are particularly busy or which have multiple primary vertices. The total latency of the L0 trigger is $4\,\mu s$, while the latency of the hardware algorithms in the calorimeter and muon detectors is $1\,\mu s$.

Level 0 muon trigger

The L0 muon trigger looks for muon tracks with a high transverse momentum (p_T). The track finding algorithm applied in the hardware searches for hits on a straight line through the five stations, giving a high purity muon identification. The expected relative transverse momentum resolution of the L0 muon trigger is about 30%. The L0 muon trigger has two selections: single muon and di-muon. The single muon required a candidate with a minimum p_T of 1.3 GeV/c. The di-muon trigger requires two muon candidates with $|p_T(1)| + |p_T(2)| > 1.5\,\text{GeV}/c$.

The signal efficiency of the single muon trigger is 91.8% for the $B_s \to J/\psi(\mu\mu)\phi(KK)$ events. For the dimuon trigger the signal efficiency is only 65.2%, as many of the $J/\psi \to \mu\mu$ decays have only one μ with sufficiently high transverse momentum. The efficiencies ε_{TOS} for L0 muon and L0 dimuon are shown in Figure 2.13 (a) [50].

Level 0 calorimeter trigger

The Level-0 calorimeter trigger searches for particles with a high transverse energy deposit (E_T) in the calorimeters. It provides candidates for charged hadrons, electrons, photons and neutral pions. The transverse energy is measured in the electromagnetic and hadronic calorimeter. The showers of $e^{\pm}$, γ and single hadrons are relatively narrow, thus a zone of two-by-two calorimeter cells is used, large enough to contain most of the energy and small enough to avoid overlaps between different particles [42]. In case of a hadronic shower, the energy deposited in the Ecal in front of the Hcal is added to the candidate. For each of the candidates, the total E_T is computed. The properties of the showers together with the scintillating pad detector (SPD) and pre-shower detector (PS) information provide a first particle hypothesis. For each particle type, only the candidate with the highest E_T is kept.

An L0 hadron candidate is formed if the transverse energy of a cluster of hadronic type is above 3.5 GeV. This leads to a rate of about 600 kHz. An electron candidate is an Ecal cluster with sufficient transverse energy ($E_T > 2.6$GeV) and measurements in the pre-shower and SPD. A photon candidate is a cluster with $E_T > 2.3$GeV and pre-shower but no SPD measurement. The above requirements reduce the rate to 200 kHz.

The L0 hadron efficiency ε_{TOS} is shown in 2.13 (b) for the two and three prong beauty decays $B^0 \to K^+\pi^-$ and $B^0 \to D^0\pi^-$ and the two, three and four prong charm decays $D^0 \to K^-\pi^+$, $D^+ \to K^-\pi^+\pi^+$ and $D^{*+} \to D^0\pi^+$. The two prong beauty decay is most efficiently triggered by the L0 hadron E_T criterion and the four prong charm decay $D^{*+} \to D^0\pi^+$ is selected with the lowest efficiency [50].

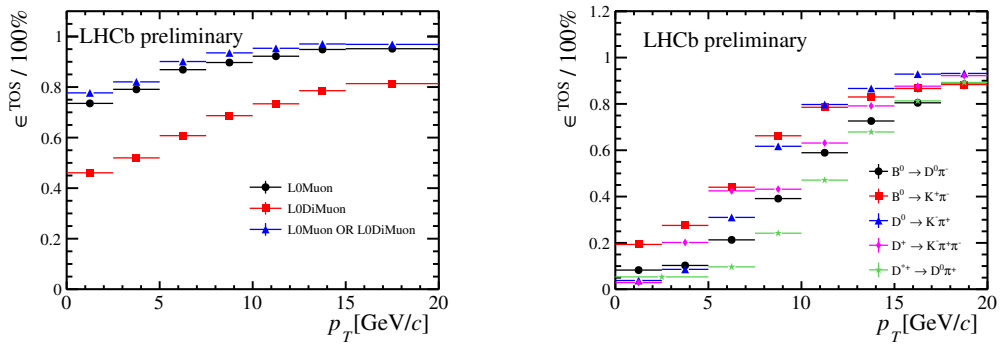

(a) (b)

Figure 2.13: (a) L0 muon trigger efficiency ε_{TOS} for $B^+ \to J/\psi K^+$. (b) L0 hadron trigger efficiency ε_{TOS} for different beauty and charm decay modes.

2.3.2 The online farm

After the hardware trigger decision the full detector is read out at a rate of 1 MHz into the Event Filter Farm (EFF) [45], where the LHCb software trigger operates. The readout scheme, as Figure 2.14 shows, proceeds as follows. A positive L0 trigger decision is sent to the Trigger and Fast Control which sends it back to the front-end electronics of all the sub-detectors. They pick up the information of the relevant events from buffers and send them through the readout network to the Event Filter Farm. The network allows a maximum throughput of 50 Gbytes/s.

The EFF consists of 29000 logical CPU cores. This size of the Event Filter Farm defines the CPU time available for the software trigger. At an input rate of 1 MHz, the software trigger algorithms have 16 ms to process a single event on one CPU.

2.3.3 The High Level Trigger

The High Level Trigger (HLT), is a C++ software application which runs on the Event Filter Farm at a rate of 1 MHz on events accepted by the hardware trigger. In the HLT, the full event information is available.

The high level trigger is divided into two levels, named HLT1 and HLT2. The HLT1 aims at a large reduction of the background rate, performing a partial reconstruction of the event. It uses physics objects from the L0 trigger as seeds to define a region of interest where the reconstruction of particles is performed. This reduces the CPU time needed for decoding and pattern recognition algorithms. At the HLT1 output rate of

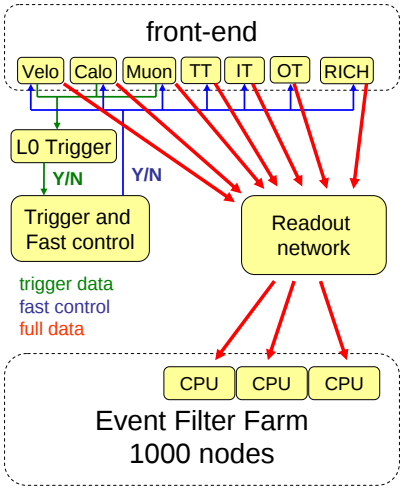

Figure 2.14: General structure of the detector readout.

about 80 kHz in 2012, the HLT2 algorithms perform a full reconstruction of the events, which is as close as possible to the off-line reconstruction. The final HLT2 output rate is about 5 kHz. Though charm physics measurements were previously absent from LHCbs primary goals, approximately 40% of the trigger output is now dedicated to them.

Each of the two HLT stages is composed of several independent parallel channels (lines) that are sequences of event reconstruction algorithms and selection criteria. Each line executes its sequence until the decision of the line is known to be negative, e.g., by the failure of a reconstruction element or selection criterion, or until the sequence is complete and the event accepted by the line. The lines of HLT2 are executed only for events that are accepted by at least one of the lines of HLT1. Events accepted by at least one HLT2 line are preserved in permanent storage. The lines of HLT1 are simple selections based on the properties of one or two reconstructed tracks. The lines of HLT2 can be quite sophisticated, incorporating complicated reconstruction elements and multivariate discriminants, and are generally tailored to the requirements of a group of physics analyses.

Higg Level Trigger 1

The partial reconstruction in HLT1 starts by reconstructing track segments in the vertex detector (VELO). High IP track segments and track segments that can be matched with hits in the muon chambers are then extrapolated into the main tracker. This extrapolation is done using the identical forward tracking algorithm [46] as used in offline

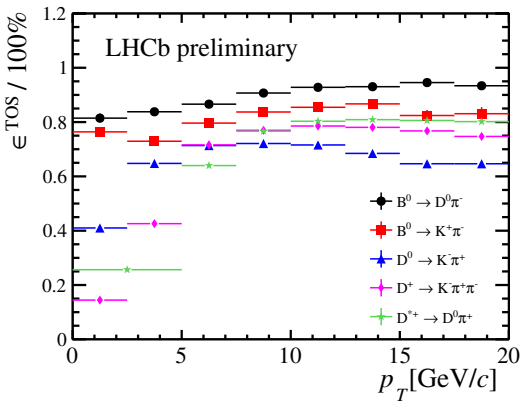

Figure 2.15: Hlt1TrackAllL0 performance: TOS efficiency for various channels as a function of B or D p_T.

processing, however, with reduced search window sizes corresponding to a minimum p_T requirement.

The inclusive beauty and charm trigger line Hlt1TrackAllL0 selects good quality track candidates based on their p_T ($p_T > 1.6\,\text{GeV}/c$) and displacement from the primary vertex. This trigger line gets the dominant part of the HLT1 bandwidth allocated, about 58 kHz. It is the dominant trigger line for most physics channels that do not contain leptons in the final state. The performance of HLT1 for hadronic signatures is shown in Figure 2.15 as a function of resonance p_T.

A similar line exists if the track is matched with hits in the muon chambers [57], Hlt1TrackMuon. This single muon trigger line selects good quality muon candidates with a $p_T > 1\,\text{GeV}$ that are not coming from the primary vertex.

Additionally to the trigger lines discussed above, special lines are implemented to enhance the trigger performance for events containing candidates for high p_T electrons, di-protons, displaced vertices or high E_T jets.

Higg Level Trigger 2

The second software trigger level, HLT2, performs a full event reconstruction for all tracks with a minimum p_T of $300\,\text{MeV}/c$. It reduces the event rate to 5 kHz, which is written to permanent storage. Because the precision and efficiency of HLT2 track reconstruction approach those of LHCbs analysis software, HLT2 lines can use the same methods and selection variables for fully reconstructing signal decays, with the exception of the charged hadron identification. Several exclusive and inclusive selections are

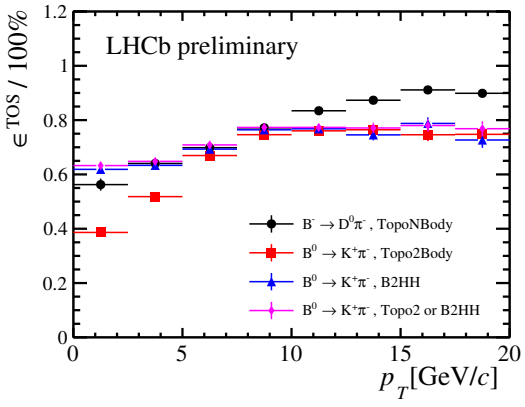

Figure 2.16: HLT2 inclusive beauty trigger performance as a function of B p_T . The efficiency for the exclusive $B^0 \to K^+\pi^-$ trigger line is also given.

performed in this trigger level, the most important ones are in the following briefly discussed.

A multivariate selection is used to trigger B decays into charged hadrons in an inclusive selection based on two, three and four track vertices (B-Topological trigger)[55]. These trigger lines, named Hlt2Topo(N)Body, are based on a BDT classifier that uses discretized input variables [54] which ensures a fast and robust implementation. Figure 2.16 shows the efficiency for the topological trigger lines for $B^0 \to K^+\pi^-$ and $B^0 \to D^0\pi^-$ events as well as the additional efficiency that can be gained by an exclusive selection for $B^0 \to K^+\pi^-$ in the low p_T regime. The output rate of the topological trigger is 2 kHz. The structure and the behavior of this trigger line is very similar to the inclusive D^{*+} trigger developed in this thesis.

Several trigger lines select events with one or two identified muons. The muon identification procedure in HLT2 is identical to the one used in offline analysis [47].

In the 2012 running, about 600 kHz of charm events are produced in the acceptance of the LHCb spectrometer. This high rate implies tight cuts on the invariant mass in exclusive trigger selections. The dominant exclusive selections for prompt charm are the hadronic two body selection Hlt2CharmHadD02HH and three body selection Hlt2CharmHadD2HHH. Only the decay chain $D^{*+} \to D^0\pi^+$ can be selected inclusively. The inclusive D^{*+} line implemented in 2012 was based on a series of loose cuts and it is described in details in the next chapter. The aim of this thesis is the development of a new more efficient algorithm to replace this line. The efficiency of these trigger lines is summarized in Figure 2.17. The total output of the charm trigger in 2012 was about

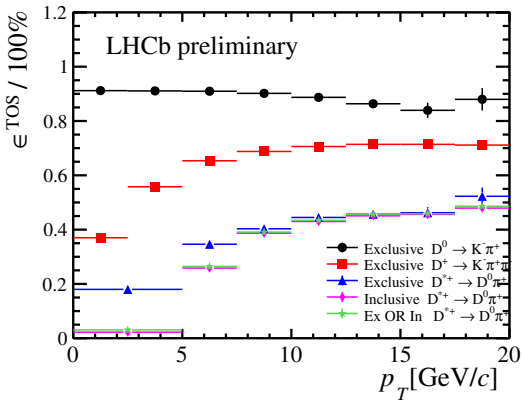

Figure 2.17: HLT2 charm trigger performance for inclusive and exclusive selections.

2 kHz.

2.3.4 Trigger system in 2015

In 2015 LHCb will resume data collection at the greater pp collision energy of $\sqrt{s} =$ 13 TeV. The L0 hardware trigger will be tuned to satisfy its 1 MHz output limit under the new conditions, but its operation will remain unchanged. The HLT software trigger will be substantially reorganized in order to improve the quality of the event reconstruction in HLT2.

The two stages of the HLT1 will be run asynchronously. This allows the deferral of events after the have been accepted by HLT1. In fact, in 2010-2012, the calibration and the fine alignment of detector elements that was used by the HLT2 reconstruction were measured in an earlier data-taking period. Since the calibration and alignment for analysis is always up-to-date, there may be small differences between the measured parameters of identical candidates as reconstructed in HLT2 and as reconstructed for analysis. This can be a source of irreducible systematic uncertainty. By performing the calibration and alignment step before the execution of HLT2, this source of uncertainty is reduced or eliminated. It also gives time to perform a calibration of the particle identification provided by the RICH detectors as well as the tracking detectors. In this way the on-line reconstruction will be performed with the same quality and precision as achieved off-line.

LHCb will be also able to profit from a larger trigger farm. Increased computing resources available in 2015 will allow to record about 12.5 kHz of events to disk.

In parallel to these improvements, a lot of work is ongoing to implement new lines

and to optimize the existing ones. New lines will be introduced for the lepton triggers, especially additional lines with on-line PID can increase the efficiency for electrons and muons. On-line PID will also allow to improve the efficiency at low p_T for the inclusive ϕ trigger. The topological B trigger will gain almost a factor 2 in efficiency exploiting new multivariate techniques. In this context the development of an inclusive D^{*+} trigger based on multivariate techniques takes placed. In fact, the current inclusive D^{*+} trigger, based on linear cuts, suffer for low efficiency. The work in this thesis aims to replace this trigger.

Figure 2.18 shows the comparison between the 2012 and the 2015 trigger system.

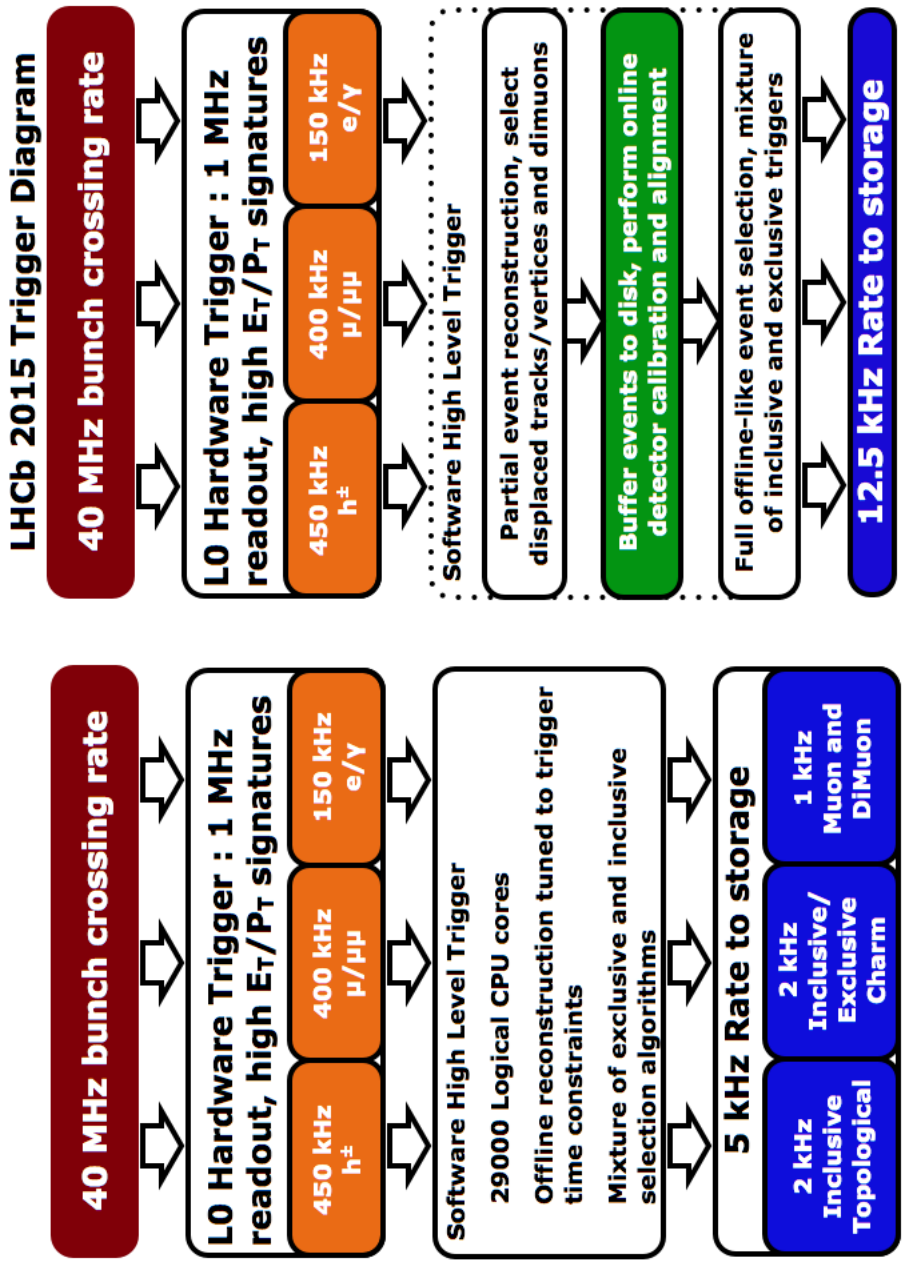

Figure 2.18: (a) The trigger system in 2012. (b) The trigger system in 2015.

Chapter 3

An inclusive multivariate technique based trigger

The aim of this thesis is the implementation of a new HLT2 trigger line for the online selection of the events with the production of a D^{*+}. A series of studies has to be performed to develop and optimize an ad-hoc algorithm which has to select signal events with a good efficiency in a very small amount of time.

To recognize the signal with respect to the background events the kinematics and the topological properties of D^{*+} candidates need to be well understood. The first section of this chapter describes the properties of the D^{*+} decay channels.

The second section presents the event reconstruction strategy. This reconstruction strategy is in common with an already implemented inclusive D^{*+} trigger line. This should be then replaced by the work developed with this thesis. This current line is described in details in the third section. In the last section the trigger strategy developed for this new line is presented.

In this chapter, the terms of D^{*+} and D^0 include their charge conjugates D^{*-} and $\bar{D}^0$, if not specified otherwise.

3.1 $D^{*+} \to D^0 \pi^+$ decay channel

The D^{*+} meson is a vector meson composed by a heavy c valence quark and a light d valence anti-quark. The rest mass of the D^{*+} meson is $m_{D^{*+}} = (2010.28 \pm 0.13)\text{MeV}/c^2$. It decays via strong interaction. Table 3.1 shows its decay modes [10].

We select events with a D^{*+} exploiting the $D^{*+} \to D^0 \pi^+$ decay channel, which has a branching ratio of $(67.7 \pm 0.5)\%$ [10]. Strong decay to the D^0 meson occurs by emitting a

Decay modes	Fraction (Γ_i/Γ)	Decay momentum (MeV/c)
$D^0\pi^+$	$(67.7 \pm 0.5)\%$	39
$D^+\pi^0$	$(30.7 \pm 0.5)\%$	38
$D^+\gamma$	$(1.6 \pm 0.4)\%$	136

Table 3.1: The D^{*+} decay channels

charged pion whose momentum is low due to the small mass difference between D^{*+} and D^0 of $(140.66 \pm 0.10)\,\mathrm{MeV}/c^2$ [10]. The low momentum pion is usually called *soft pion* and is symbolized as π_s. The peculiar kinematics in the decay of the D^{*+} meson leads to a narrow internal width $\Gamma = (96 \pm 22)\,\mathrm{keV}/c^2$ [10]. Thus, the width of the invariant mass of the reconstructed D^{*+} is solely defined by the experimental momentum resolution.

3.1.1 D^0 decay modes

A D^0 meson consists of two valence quarks, a light u quark and a heavy c quark. Its rest mass is $m_{D^0} = (1864.86 \pm 0.13)\,\mathrm{MeV}/c^2$ [10]. Since the D^0 is the lightest charmed hadron, it decays only through weak processes. Due to the large mass of the W and Z bosons, weak decay is much more unlikely than strong or electromagnetic decay, and hence occurs less rapidly. Therefore the D^0 mean lifetime is much longer than respect to the D^{*+}, resulting in a long mean decay length of $c\tau = (122.9 \pm 0.5)\mu\mathrm{m}$ [10], $\sim 4\,\mathrm{mm}$ in the laboratory frame. The D^0 can decay into many different decay channels. In Table 3.2 the decay modes considered in this thesis are listed.

3.2 Decay event reconstruction

The peculiarity of this trigger line is the use of a multivariate analysis tool to on-line select the signal events. In order to completely exploit the potential of this complex tool it is necessary to carry out some preliminary steps. First of all it is necessary to choose how this trigger line will reconstruct the D^{*+} candidates. This is not trivial, due to the kinematics of the D^{*+} decay chain and the inclusive nature of this line.

The selection is designed to reconstruct the candidates exploiting the information deriving from the VELO and the Tracking System. It defines all the possible combinations of two tracks to form a Secondary Vertex (SV), which is the point in 3-dimensional space where the D^0 particle decays. Thus in case of 3 or 4 bodies decay the D^0 is only partially reconstructed. This choice allows this trigger line to be inclusive. Inclusive here means

Decay mode	Fraction (Γ_i/Γ)	Decay momentum (MeV/c)
$K^-\pi^+$	$(3.88 \pm 0.05)\%$	867
$K^-\pi^+\pi^-\pi^+$	$(8.08\pm^{0.21}_{0.19})\%$	813
$K^-\pi^+\pi^0$	$(13.9 \pm 0.5)\%$	844
$K^0_S\pi^+\pi^-$	$(2.82 \pm 0.19)\%$	842
$K^0_S K^+ K^-$	$(4.45 \pm 0.34) \times 10^{-3}$	544
$\phi\rho^0$	$(7.0 \pm 0.6) \times 10^{-4}$	250
$\phi\pi^+\pi^-$	$(2.4 \pm 2.4) \times 10^{-5}$	614
$K^-K^+\pi^+\pi^-$	$(2.43 \pm 0.12) \times 10^{-3}$	677
$\pi^+\pi^-$	$(1.401 \pm 0.027) \times 10^{-3}$	922
$\mu^+\mu^-$	$< 1.4 \times 10^{-7}$ CL=90%	926
$\pi^+\pi^-\mu^+\mu^-$	$< 3 \times 10^{-5}$ CL=90%	894
$K^-\mu^+\nu_\mu$	$(3.30 \pm 0.13)\%$	864
$\pi^-\mu^+\nu_\mu$	$(2.37 \pm 0.24) \times 10^{-3}$	924

Table 3.2: The D^0 decay modes

that the trigger line is inherently designed to be efficient across the full range of the D^{*+} decay topologies which can be reconstructed inside the LHCb detector acceptance. This means that the kinematical properties of the D^0 are not fully reconstructed in case of 3 or 4 bodies decays.

Once the D^0 is reconstructed it is combined with a third track, the soft pion π^+_s, in order to eventually define the D^{*+} particle. Because of the short D^{*+} lifetime, within the detector resolution the D^{*+} is produced at the Primary Vertex (PV), which is the proton-proton collision vertex in 3-dimensional space. At this point a D^{*+} candidate is defined. It is important to note the difference between candidate and event. As candidate we refer to the reconstructed D^{*+} with its decay chain, as event we refer to proton-proton collision with all its interaction products. Each event can contain multiple candidates. Once one candidate is recognized as signal, the whole event is then selected.

Typical kinematics variables used for the trigger selectiom are: the maximum distance of closest approach between two tracks, called DOCA, of the helicity angle ϑ which is defined as the angle between the track's momentum in its mothers frame and the mother's momentum in the laboratory frame (see Figure 3.1) and of the flight distance which is defined as the distance in millimeters between two particle vertices. In this thesis the flight distance of a particle is always defined as the distance between the primary vertex and the decay vertex of that particle. The Impact Parameter (IP) d_0 is

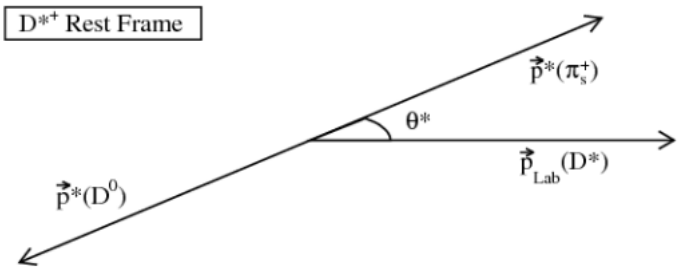

Figure 3.1: Pictorial illustration of the π_s^+ $cos\vartheta$.

Figure 3.2: Schematic view of the $D^{*+} \to D^0\,(K^-\pi^+)\pi_s^+$ decay

the distance of closest approach between the Primary Vertex and the prolonged particle trajectory. The full reconstruction performed in HLT2 allows the selections to use error information on values like flight distance and impact parameters, thus we prefer to cut on their χ^2 rather than their raw values as is done in HLT1, when possible. Figure 3.2 shows the topology of a $D^{*+} \to D^0\,(K^-\pi^+)\pi_s^+$ decay, d_0^K and d_0^π represent the impact parameters of the K^- and π^+ particles from the D^0 decay.

3.3 Current inclusive D^* trigger

Prompt charm candidates (produced at the primary interaction vertex) are selected and collected by LHCb using a combination of exclusive and inclusive high level triggers in conjunction with low level hardware triggers. Although highly successful, HLT2 lines for exclusive reconstruction of decay modes are necessarily limited. As shown in previous

Variable	Cut value
Track IP [mm]	> 0.1
Number VELO hits/track	> 9
Number missed VELO hits/track	< 3
Number OT+IT $\times 2$ hits/track	> 16
Track IP χ^2	> 16
Track p_T [GeV/c]	> 1.7
Track P [GeV/c]	> 10
Track χ^2/ndf	> 2.5

Table 3.3: HLT1 Hlt1TrackAllL0 line cuts

section, inclusive selections that do not depend on a complete reconstruction of signal decays can allow for efficient selection of a broader range of decay modes, including modes for which a full reconstruction is impossible, such as every decay with a neutral particle.

The HLT2CharmHadD02HHXDst_hhX line is the current inclusive trigger line dedicated to the selection of events with the production of a D^{*+} [48]. It has been developed and used in the 2012 data collection. This line reconstructs every track that pass any L0 alley and the Hlt1TrackAllL0 HLT1 line. Hlt1TrackAllL0 accepts events that were accepted by any L0 channel and that have at least one track that satisfies a number of track quality criteria [50], that is displaced from every reconstructed PV in the event (impact parameter with respect to each PV > 0.1 mm), and that has a relatively large estimated p_T ($p_T > 1.7\,\text{GeV}/c$). Table 3.3 shows the list of the Hlt1TrackAllL0 cuts. HLT2CharmHadD02HHXDst_hhX has been associated to the Hlt1TrackAllL0 because this HLT1 line selects tracks that are typically produced by the decay products of c and b hadrons and are excellent signatures of long-lived heavy hadrons.

The current line exploits the same candidate reconstruction strategy described in the previous section. The selection of signal events is made by a series of linear cuts, which necessarily have to be loose for the inclusive nature of the line. Partial D^0 decay candidates are reconstructed as two-track vertices that are significantly displaced from all PVs. For the mass of the D^0 it is possible to take in account the missing daughters using the so called *corrected-mass* [49], defined as follows:

$$m_{cor} = \sqrt{m^2 + |p_T^{miss}|^2} + |p_T^{miss}| \tag{3.1}$$

where m is the mass and p_T^{miss} is the missing momentum transverse to the direction

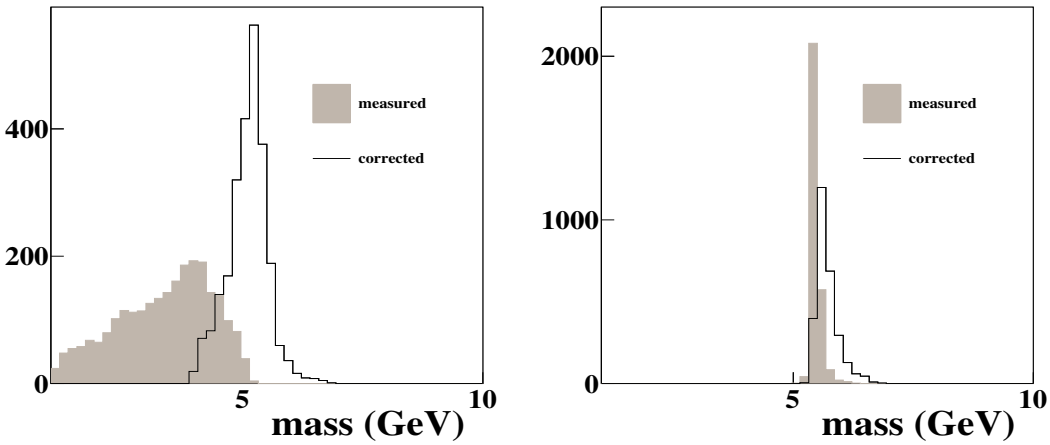

Figure 3.3: B-candidate masses and corrected masses (line) from $B \to K\pi\pi$ decays: (left) HLT2 2-body trigger candidates; (right) HLT2 3-body topological trigger candidates.

of flight of the candidate assuming it originates from its best PV. Figure 3.3 shows the performance of *corrected-mass* in the case of B-candidate masses from $B \to K\pi\pi$ decays. For cases where there are missing daughters, the corrected-mass distributions are fairly narrow and peak near the B mass. When the trigger candidate is formed from all of the daughters, the corrected-mass distributions, as expected, are slightly wider and shifted upwards by a small amount as compared with the mass distributions. A loose cut on the corrected mass of the D^{*+} is then setted.

These two-track vertexes are then combined with π^+ candidates to form D^{*+} candidates, and additional basic kinematic and reconstruction quality criteria are applied to the system. For true D^{*+} decays, the small mass difference between the reconstructed D^{*+} and D^0 candidates peaks strongly at the true value, even when the D^0 decays are not fully reconstructed. In Table 3.4 all the required cuts are listed. Figure 3.4 shows the mass difference distribution between the reconstructed D^{*+} and D^0 candidates. The peak at the true value of $140.66\,\mathrm{MeV}/c^2$ is clearly visible. A large tail at higher values also appears due to not fully reconstructed candidates and background candidates. The rate of this trigger line in 2012 was about 840 Hz [56].

3.4 Strategy for a new D^{*+} trigger

Being based only on a series of loose cuts, the current inclusive D^{*+} trigger can collect a wide set of different signals, but also a lot of background candidates.

In 2015 LHCb will resume data collection at the greater pp collision energy of $\sqrt{s} =$

Particle	Variable and value
D^0 daughters	Track $\chi^2 < 3$
D^0 daughters	DOCA < 0.1mm
D^0 daughters	$p_T > 300$MeV/c
D^0 daughters	$P > 3$GeV/c
D^0	Vertex $\chi^2 > 20$
D^0	χ^2 flight distance > 100
D^0	Corrected mass < 3500MeV/c^2
D^0	χ^2 vertex < 10
D^0	Track $\chi^2 < 2.25$
π_s^+	$p_T > 300$MeV/c
π_s^+	$P > 3$GeV/c
π_s^+	Track $\chi^2 < 2.25$
π_s^+	χ^2 IP < 9
D^{*+}	Mass < 2500MeV/c^2
D^{*+}	DOCA < 100mm
D^{*+}	$p_T > 3.75$GeV/c
D^0 and D^{*+}	$M(D^{*+}) - M(D^0) < 285$MeV/c^2

Table 3.4: Current trigger line cuts

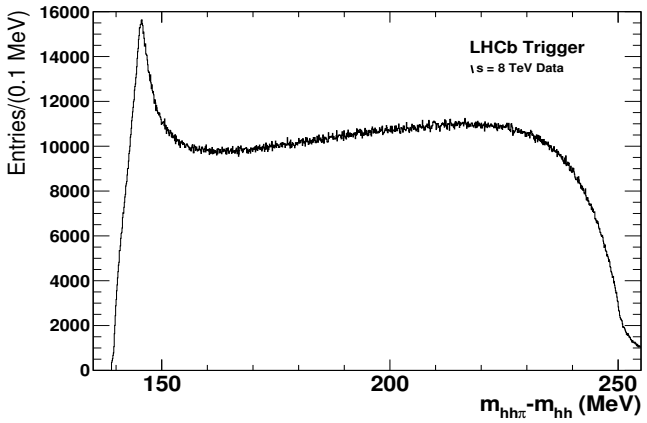

Figure 3.4: Mass difference distribution of reconstructed candidates for the current HLT2 inclusive D^{*+} line

13 TeV. This will lead also to a great increase in the luminosity and thus to the number of events, in particular of background events [51]. The goal of this thesis is to replace this trigger line with a multivariate technique-based one. The use of a supervised learning algorithm should allow to maintain the inclusive nature of the line but with a better rejection of the background candidates. The goal is to collect a sample with higher efficiency on signal and better purity, key demand considering the new environment LHCb has to face from 2015. The trigger strategy for the new line is described in the following.

As for the old trigger, all those tracks that pass any L0 alley and the Hlt1TrackAllL0 HLT1 line are the input for this line. Tracks selected by Hlt1TrackAllL0 are then combined to reconstruct the D^{*+} candidates. The reconstruction strategy has been described in details on section 3.2. While the reconstruction is performed, some cuts on the kinematic variables of the candidates are required. We refer to them as preliminary cuts. In the reconstruction stage every possible combination of two particles is considered, and this leads to a huge combinatorial background. Introducing these loose cuts only candidates which are kinematically similar to the expected signal are selected and sent to the next stage.

The last and more selective phase is indeed made by the multivariate selection tool. This tool exploits the discrimination power of some variables to separate the signal from the background candidates. Thus, we have to use as input variables the best discriminating ones between background and signal. But the inclusive nature of this trigger forces us to choose only variables not correlated with properties which depend on the particular D^{*+} decay chain, such as the masses.

Among the all possibles multivariate tools this trigger line is based on the Bonsai Boosted Decision Tree (see section 4.3.3) for its adaptability to the HLT2 peculiarities. This tool is in turn directly based on the Boosted Decision Tree multivariate technique. All the reconstructed candidates selected by the preliminary cuts are then analyzed and recognized as signal or background. Only the events with a reconstructed signal candidates will be eventually recorded and saved on disk.

Chapter 4

Trigger implementation

Having presented the trigger strategy we can move to the implementation of the trigger line. Studies to find the best configuration and setup are presented in this chapter.

In the first section we define the background-like and the signal-like samples used for these studies. The same samples are also exploited for the multivariate tool training.

Exploiting the kinematics peculiarities of the D^0 decay modes we apply some preliminary cuts on the dataset to decrease the combinatorial background, otherwise too large. In the second section we present these preliminary cuts and their effects on the variables distributions.

The key point of this trigger line is the use of a multivariate analysis tool, the Boosted Decision Tree (BDT). A brief description of this method and its implementation in the trigger software will follow in the third section.
Also in this chapter, the terms of D^{*+} and D^0 include their charge conjugates D^{*-} and $\bar{D}^0$, if not specified otherwise.

4.1 Signal and Background samples

The studies to optimize the preliminary cuts and train the BDT are performed on signal and background samples of off-line reconstructed events. We do not expect any significant difference when we will implement the HLT2 line, as on-line variables used at HLT2 level have off-line-like quality.

The background sample is a set of real 2012 events collected with the Minimum Bias trigger, i.e. a trigger which applies very loose selection on the events.

For the signal, among the several D^0 decay modes we use 13 Monte Carlo samples, available in the LHCb data repository (bookkeeping). They cover all the possible kind

Decay mode	$\sqrt{s}$ [TeV]	Simulated condition year
$D^{*+} \to D^0(K^-\pi^+)\pi_s^+$	8	2012
$D^{*+} \to D^0(K^-\pi^+\pi^-\pi^+)\pi_s^+$	8	2012
$D^{*+} \to D^0(K^-\pi^+\pi^0)\pi_s^+$	7	2011
$D^{*+} \to D^0(K_S^0(\pi^+\pi^-)\pi^+\pi^-)\pi_s^+$	7	2011
$D^{*+} \to D^0(K_S^0(\pi^+\pi^-)K^+K^-)\pi_s^+$	8	2012
$D^{*+} \to D^0(\phi(\mu^+\mu^-)\rho^0(\pi^+\pi^-))\pi_s^+$	7	2011
$D^{*+} \to D^0(\phi(\mu^+\mu^-)\pi^+\pi^-)\pi_s^+$	7	2011
$D^{*+} \to D^0(K^-K^+\pi^+\pi^-)\pi_s^+$	7	2011
$D^{*+} \to D^0(\pi^+\pi^-)\pi_s^+$	7	2011
$D^{*+} \to D^0(\mu^+\mu^-)\pi_s^+$	8	2012
$D^{*+} \to D^0(\pi^+\pi^-\mu^+\mu^-)\pi_s^+$	7	2011
$D^{*+} \to D^0(K^-\mu^+\nu_\mu)\pi_s^+$	8	2012
$D^{*+} \to D^0(\pi^-\mu^+\nu_\mu)\pi_s^+$	7	2011

Table 4.1: The Monte Carlo signal samples

of decay mode in 2, 3 or 4 bodies, channels with high branching ratio as well as channels not foreseen in the Standard Model. The list of these decays modes is shown in Table 4.1, in Table 3.2 the respective branching ratios [10]. MC samples cover both 2011 and 2012 conditions, when the energy in the center of mass frame was 7 and 8 TeV respectively.

These simulated samples are built with two different versions of Pythia, 6 and 8 [52]. This could lead to differences in the variables distributions of different samples not due to the physics of the events but to the different versions of the generator. To check that no bias is introduced due to the simultaneous use of dataset obtained with two different versions, we compare the distributions of the same signal sample, $D^{*+} \to D^0(K^-\pi^+)\pi_s^+$, once obtained with Pythia 6 and once with Pythia 8. Some distributions are shown as example in Figure 4.1 and 4.2. In Figure 4.1 variables distributions of the D^{*+} particle are plotted, in blue generated with Pythia 6, in red with Pythia 8. The same distributions are shown in Figure 4.2 for the D^0 particle. From these plots we can infer that the use of Monte Carlo samples obtained with different Pythia versions does not introduce any bias in our analysis. In fact the distributions are well compatible, only in the primary vertex χ^2 a slight difference is visible. We get a little better reconstruction quality of the primary vertex with Pythia 8. It is something expected because of a different algorithm in the simulation of the primary vertex between the two versions, but, due to the small difference between the two distributions, this does not affect our analysis.

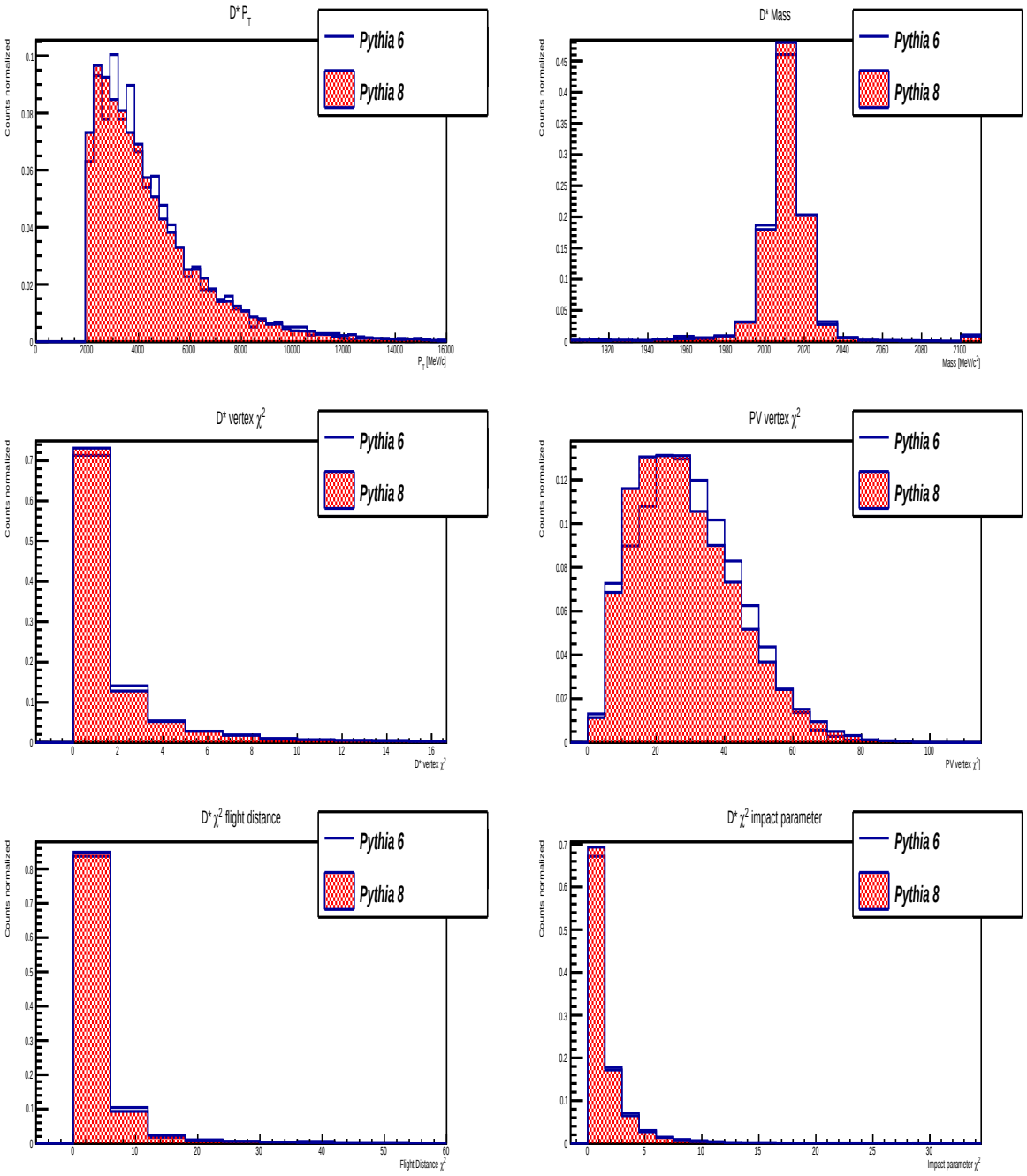

Figure 4.1: Comparison between D^{*+} distributions of $D^{*+} \rightarrow D^0(K^-\pi^+)\pi_s^+$ signal sample obtained with Pythia 6 (blue) and Pythia 8 (red). From top left, clockwise: p_T, mass, primary vertex χ^2, χ^2 impact parameters, χ^2 flight distance, vertex χ^2.

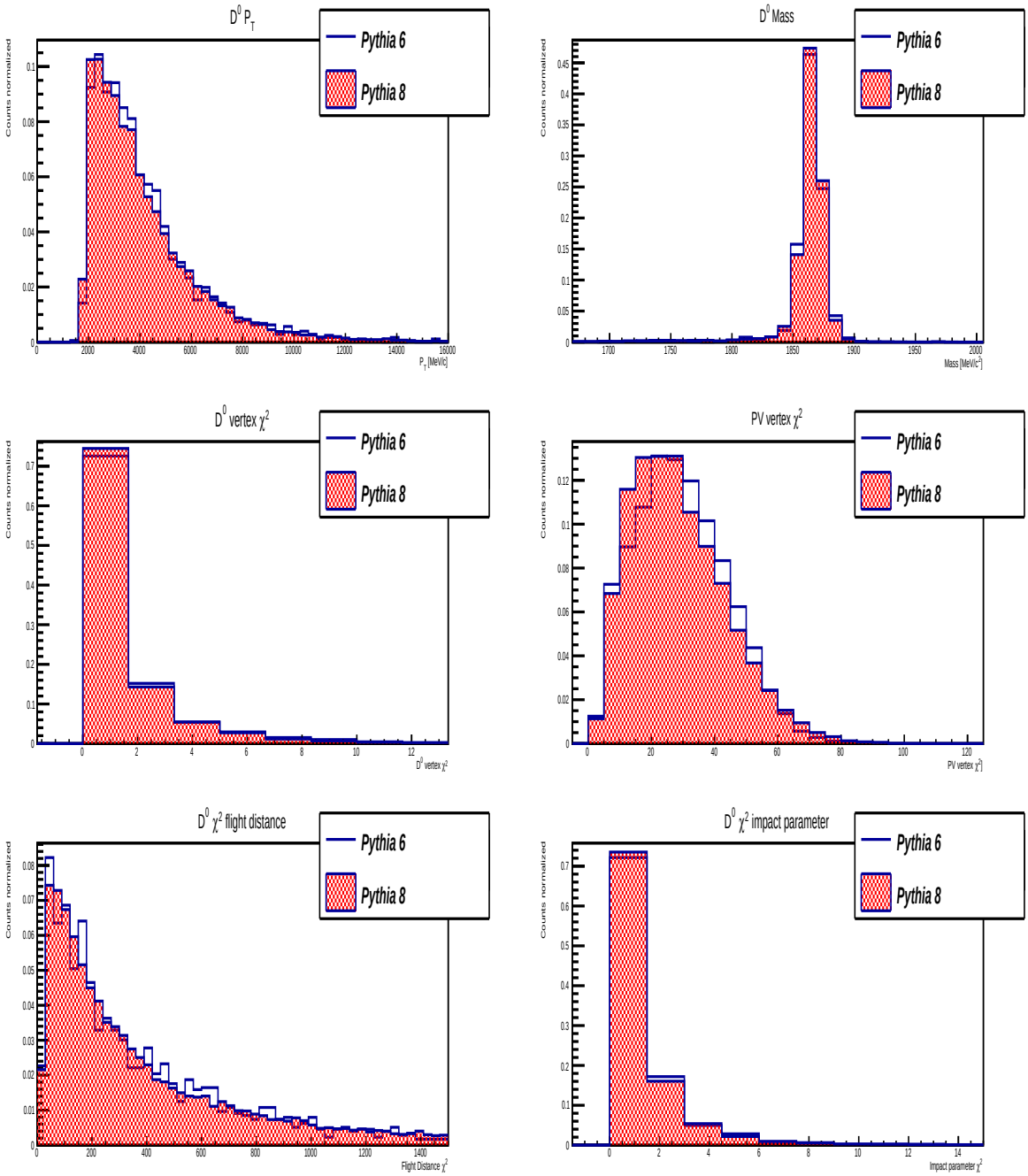

Figure 4.2: Comparison between D^0 distributions of $D^{*+} \to D^0(K^-\pi^+)\pi_s^+$ signal sample obtained with Pythia 6 (blue) and Pythia 8 (red). From top left, clockwise: p_T, mass, primary vertex χ^2, χ^2 impact parameters, χ^2 flight distance, vertex χ^2.

Particle	Variable and value
D^0 daughters	Track $\chi^2 < 3$
D^0 daughters	$p_T > 200\text{MeV}/c$
D^0 daughters	χ^2 distance wrt PV > 4
D^0	Corrected mass $< 2100\text{MeV}/c^2$
D^{*+}	Mass $< 2500\text{MeV}/c^2$
D^{*+}	$p_T > 2\text{GeV}/c$
D^0 and D^{*+}	$M(D^{*+}) - M(D^0) < 800\text{MeV}/c^2$
D^0 and D^{*+}	χ^2 vertex < 100

Table 4.2: The preliminary cuts

4.2 Preliminary cuts

If in the MB sample we accept any reconstructed candidate, for each event we find about 6.5×10^4 D^{*+} candidates. It is something expected as we are considering each possible combinations of any two tracks in the final state to form the D^0. Thus we have to apply some preliminary cuts in order to remove the combinatorial background.

The cuts have to be enough loose so the real discrimination between signal and background is left to the BDT. But from the other hand they have to be enough tight to significantly decrease the combinatorial background and to keep enough small the final rate of the trigger line.

We apply some cuts both on the tracks from the D^0 decays and on the D^0 and D^{*+} particles themselves. We consider only tracks well reconstructed requiring a track χ^2 less than 3, with a lower bound of $200\,\text{MeV}/c$ on the p_T and displaced with respect to the primary vertex as they come from the secondary vertex. We require both the primary vertex and the secondary vertex to be well reconstructed, selecting only those with a vertex χ^2 less than 100. We put a loose higher bound on the D^0 corrected mass ($2.1\,\text{GeV}/c^2$) and on the D^{*+} mass ($2.5\,\text{GeV}/c^2$), besides a lower bound to its p_T of $2\,\text{GeV}/c$. We also consider only candidates with a difference of mass between the D^{*+} and the D^0 lower than $800\,\text{MeV}/c^2$, quantity that carries information on the π_s. In Table 4.2 all the preliminary cuts are listed. After this selection we get about 23 D^{*+} candidate per event, to be compare with 6.5×10^4 without cuts.

The same preliminary cuts applied to the Minimum Bias data sample, Table 4.2, are also applied to the Monte Carlo signal samples. We need to be sure that the selected events are really signal events. So we require that the candidates come from real $D^{*+} \rightarrow$

Decay mode	Efficiency
$D^{*+} \to D^0(K^-\pi^+)\pi_s^+$	$0,82 \pm 0,02$
$D^{*+} \to D^0(K^-\pi^+\pi^-\pi^+)\pi_s^+$	$0,95 \pm 0,02$
$D^{*+} \to D^0(K^-\pi^+\pi^0)\pi_s^+$	$0,87 \pm 0,01$
$D^{*+} \to D^0(K_S^0(\pi^+\pi^-)\pi^+\pi^-)\pi_s^+$	$0,90 \pm 0,03$
$D^{*+} \to D^0(K_S^0(\pi^+\pi^-)K^+K^-)\pi_s^+$	$0,90 \pm 0,04$
$D^{*+} \to D^0(\phi(\mu^+\mu^-)\rho^0(\pi^+\pi^-))\pi_s^+$	$0,89 \pm 0,04$
$D^{*+} \to D^0(\phi(\mu^+\mu^-)\pi^+\pi^-)\pi_s^+$	$0,90 \pm 0,03$
$D^{*+} \to D^0(K^-K^+\pi^+\pi^-)\pi_s^+$	$0,92 \pm 0,02$
$D^{*+} \to D^0(\pi^+\pi^-)\pi_s^+$	$0,71 \pm 0,02$
$D^{*+} \to D^0(\mu^+\mu^-)\pi_s^+$	$0,86 \pm 0,02$
$D^{*+} \to D^0(\pi^+\pi^-\mu^+\mu^-)\pi_s^+$	$0,93 \pm 0,04$
$D^{*+} \to D^0(K^-\mu^+\nu_\mu)\pi_s^+$	0.87 ± 0.04
$D^{*+} \to D^0(\pi^-\mu^+\nu_\mu)\pi_s^+$	$0,88 \pm 0,03$

Table 4.3: Preliminary cuts efficiencies for Monte Carlo signals

$D^0\pi_s^+$ decays within the detector acceptance. Table 4.3 shows the efficiencies of these cuts for some signals, defined as the ratio between the events before and after the cuts.

These cuts have been tuned to reduce sculpting the combinatorial background and the signal. To check if the preliminary cuts introduce any bias in the variables, we compare the distributions, both for the Minimum bias and the signal samples for every particles and each variables before and after these cuts. We look for any strange trend caused by the cuts in the various distributions. As an example in the Figures 4.3, 4.4, 4.5, 4.6 and 4.7 we plot some distributions for each particle involved in the $D^{*+} \to D^0(K^-K^+\pi^+\pi^-)\pi_s^+$ decay channel. In blue distributions without cuts, in red with cuts. Figure 4.3 shows the p_T, the mass, the vertex χ^2, the primary vertex χ^2, the χ^2 flight distance and the χ^2 impact parameter for the reconstructed D^{*+} particle. In Figure 4.4 the same distributions for the D^0 particle. In the D^{*+} p_T the effect of the $2\,\mathrm{GeV}/c$ cut is visible and influences also the D^0 p_T. The mass distributions remain unchanged by the large cuts, as expected. It happens also for the other variables, and it is exactly what we would expected. Figure 4.5, 4.6 and 4.7 show the p_T, the cosine of the helicity angle and the χ^2 impact parameter of the π_s and of the two tracks from the D^0 decay. For the π_s is visible a pronounced difference in the p_T; it is due to the cut on the D^{*+} mother. The displacement in the p_T and χ^2 impact parameter tracks distributions are due to the really loose cuts applied, not directly visible in Figure 4.5.

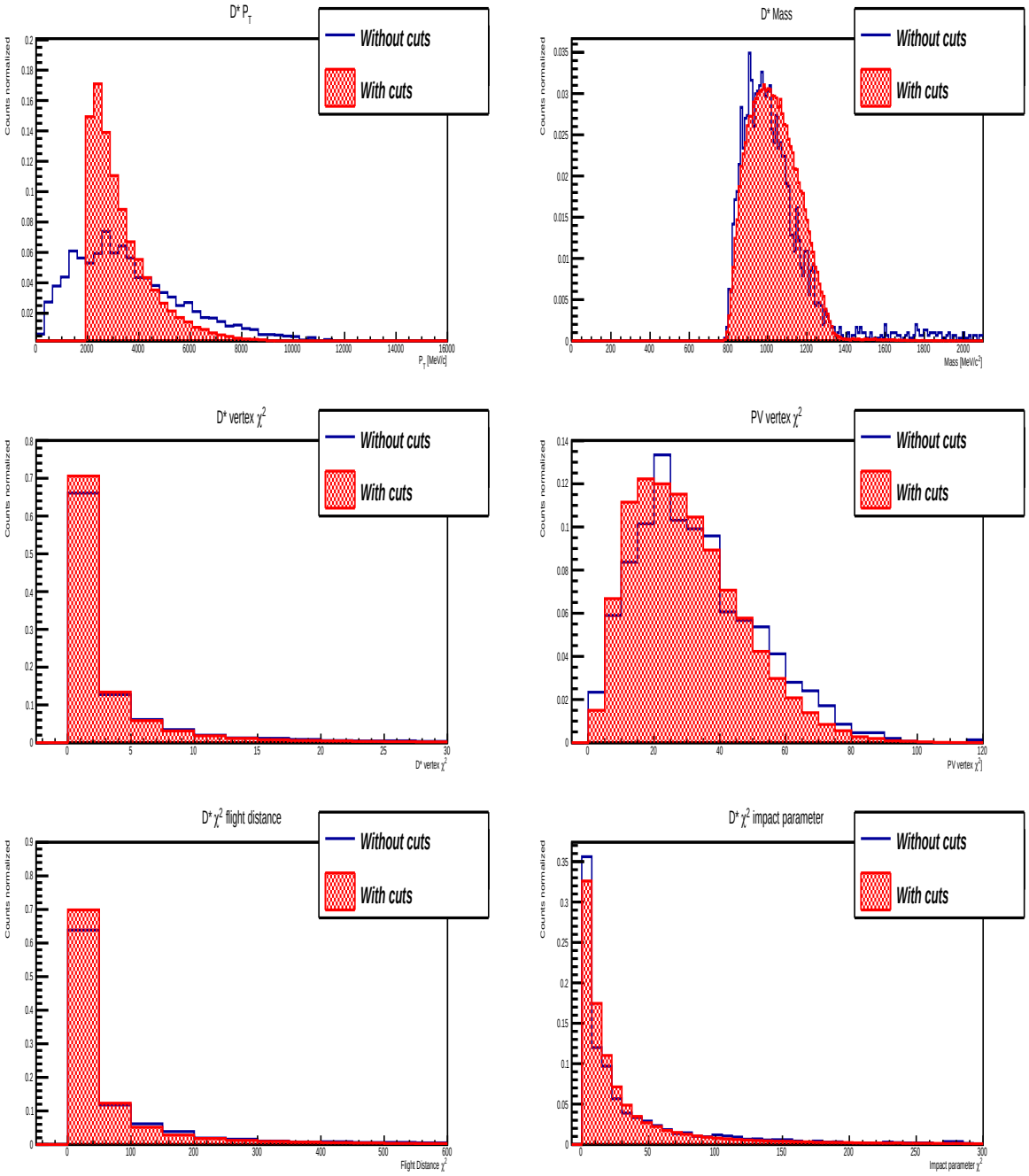

Figure 4.3: Comparison between D^{*+} distributions of $D^{*+} \to D^0(K^-K^+\pi^+\pi^-)\pi_s^+$ signal sample obtained without preliminary cuts (blue) and with cuts (red). From top left, clockwise: p_T, mass, primary vertex χ^2, χ^2 impact parameters, χ^2 flight distance, vertex χ^2.

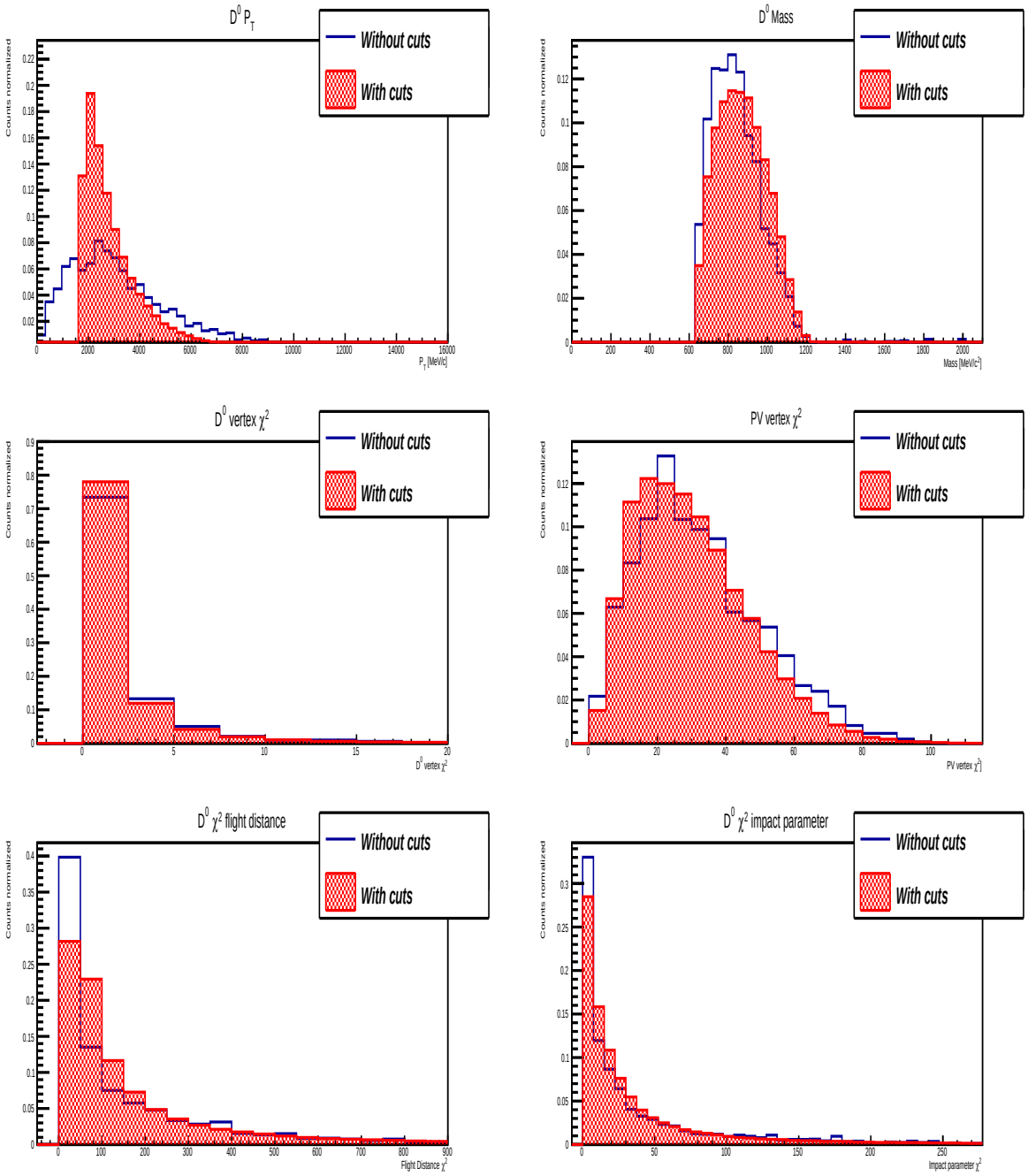

Figure 4.4: Comparison between D^0 distributions of $D^{*+} \to D^0(K^-K^+\pi^+\pi^-)\pi_s^+$ signal sample obtained without preliminary cuts (blue) and with cuts (red). From top left, clockwise: p_T, mass, primary vertex χ^2, χ^2 impact parameters, χ^2 flight distance, vertex χ^2.

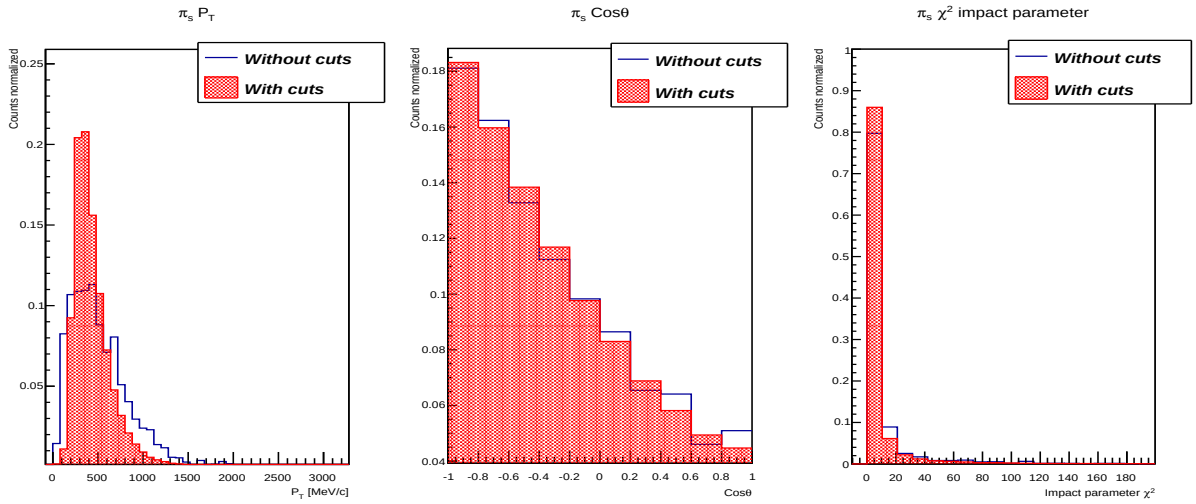

Figure 4.5: Comparison between π_s^+ distributions of $D^{*+} \to D^0(K^-K^+\pi^+\pi^-)\pi_s^+$ signal sample obtained without preliminary cuts (blue) and with cuts (red). From left: p_T, cosine of the helicity angle, χ^2 impact parameters.

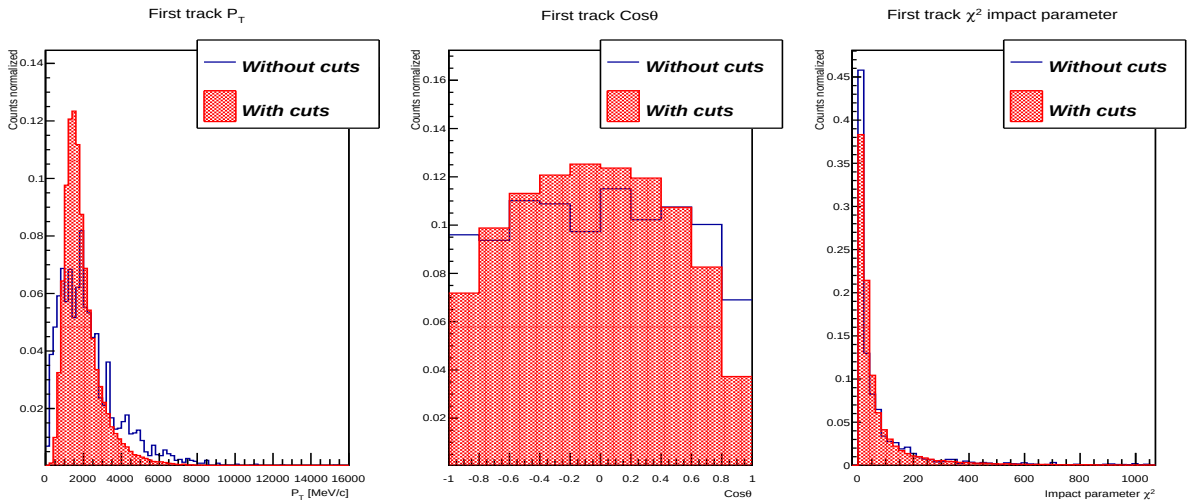

Figure 4.6: Comparison between the first track from the D^0 decay distributions of $D^{*+} \to D^0(K^-K^+\pi^+\pi^-)\pi_s^+$ signal sample obtained without preliminary cuts (blue) and with cuts (red). From left: P_T, cosine of the helicity angle, χ^2 impact parameters.

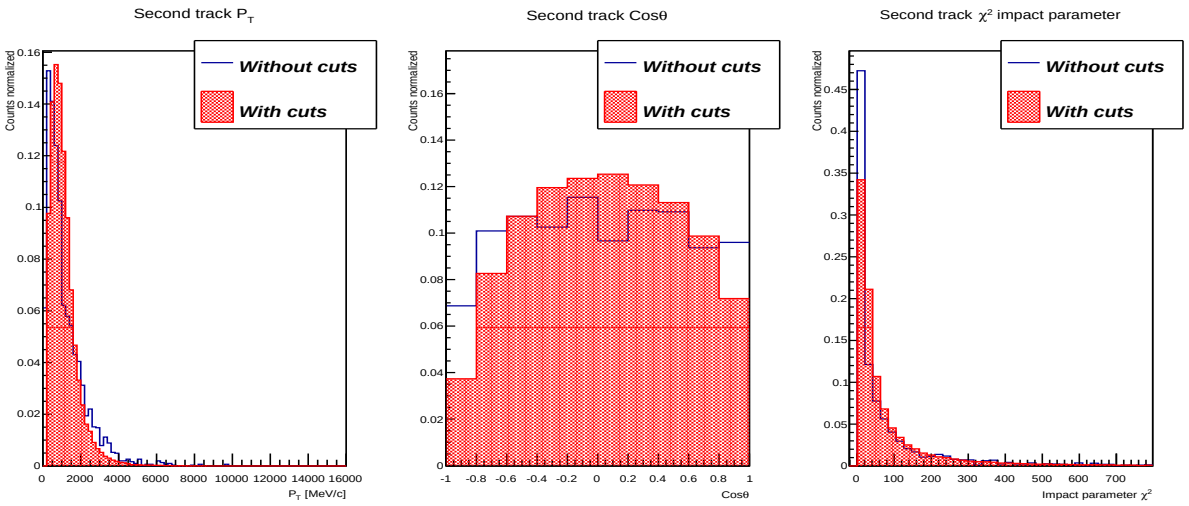

Figure 4.7: Comparison between the second track from the D^0 decay distributions of $D^{*+} \to D^0(K^-K^+\pi^+\pi^-)\pi_s^+$ signal sample obtained without preliminary cuts (blue) and with cuts (red). From left: P_T, cosine of the helicity angle, χ^2 impact parameters.

The same variables distributions for the D^{+*} and the D^0, with the primary vertex χ^2 replaced by the DOCA, are shown in Figure 4.8 and 4.9 for the Minimum Bias sample. In this case the preliminary cuts heavily change the shape of the variables, e.g. the mass. This is expected, as we are selecting only some percent of the background candidates, only those more signal-like. But of course we need to check that we are not selecting a background too similar to the signal. In Figure 4.10 we compare the D^0 mass distribution between the background (red) and the $D^{*+} \to D^0(K^-\pi^+)\pi_s^+$ (blue). The separation of the two samples is clear, which means that the variables still have discriminating power.

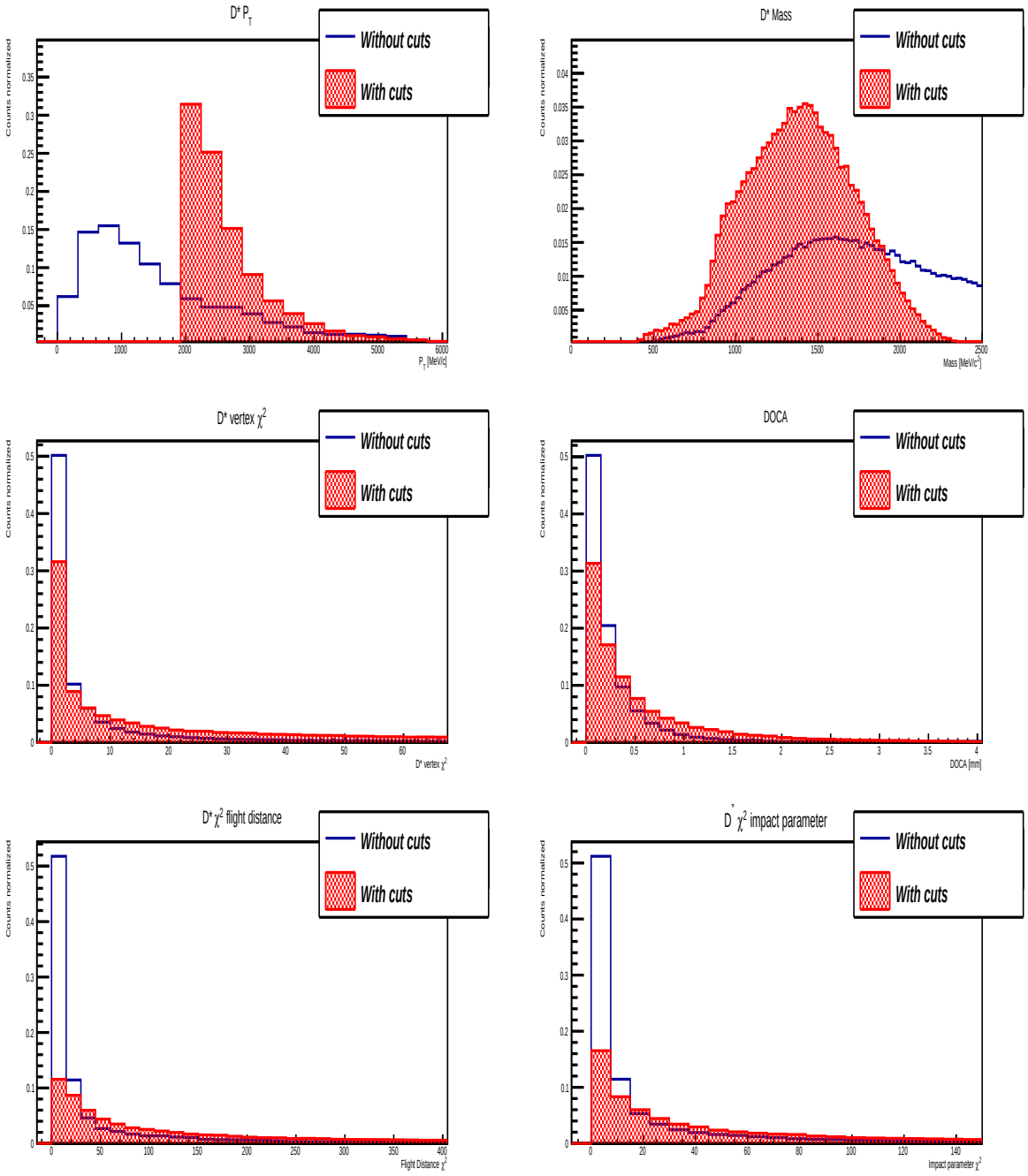

Figure 4.8: Comparison between D^{*+} distributions of the Minimum Bias sample obtained without preliminary cuts (blue) and with cuts (red). From top left, clockwise: p_T, mass, DOCA, χ^2 impact parameters, χ^2 flight distance, vertex χ^2.

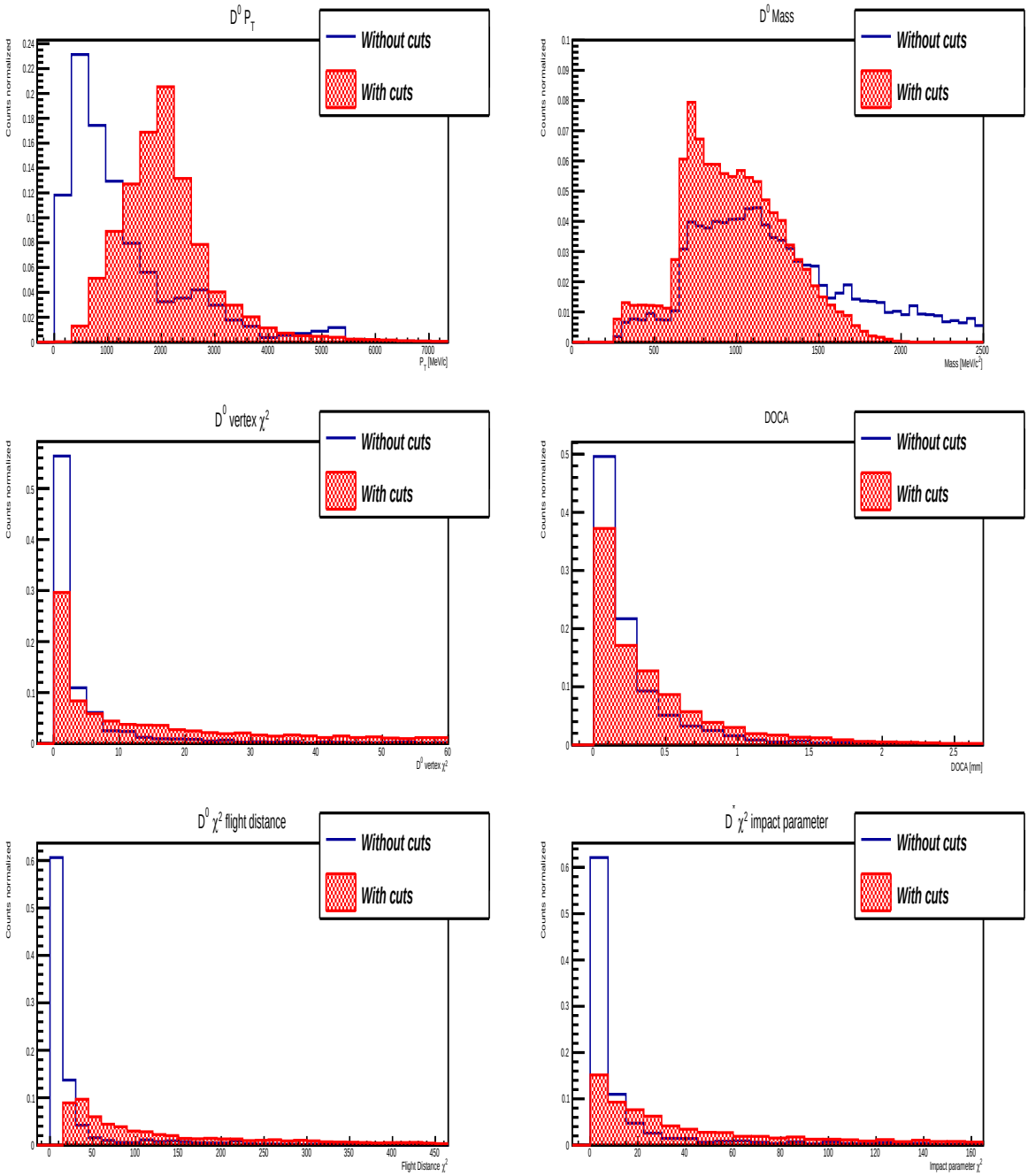

Figure 4.9: Comparison between D^0 distributions of the Minimum Bias sample obtained without preliminary cuts (blue) and with cuts (red). From top left, clockwise: p_T, mass, DOCA, χ^2 impact parameters, χ^2 flight distance, vertex χ^2.

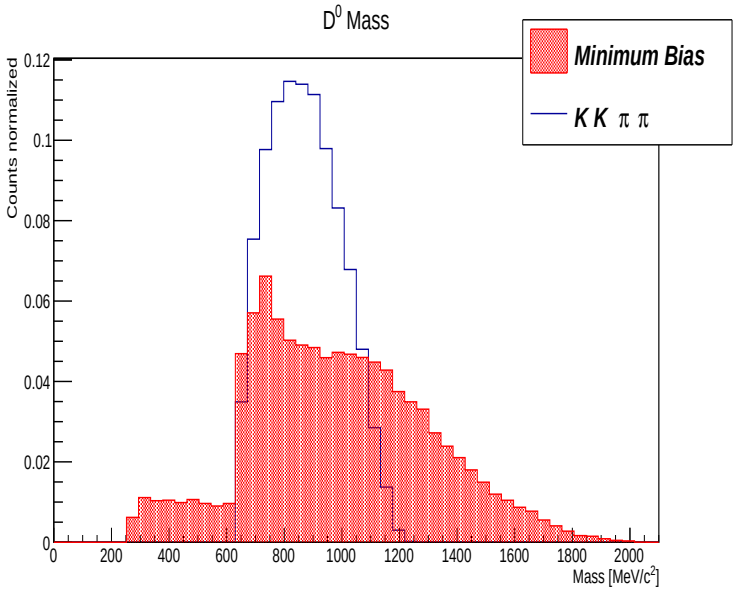

Figure 4.10: Comparison between the D^0 mass distributions of the Minimum Bias sample (red) and the $D^{*+} \to D^0(K^-K^+\pi^+\pi^-)\pi_s^+$ signal sample (blue).

4.3 Boosted Decision Tree

The bulk of the rejection power of this trigger line is achieved through a multivariate classifier. All multivariate techniques belong to the family of supervised learning algorithms. They make use of training events, for which the desired output is known, to determine the mapping function that describes a decision boundary. They are intensely used in high-energy physics where, with the search for ever smaller signals in ever larger data sets, it has become essential to extract a maximum of the available information from the data. The multivariate package used in this thesis is the Toolkit for Multivariate Analysis (TMVA) [53], which provides a ROOT-integrated environment for the processing, parallel evaluation and application of multivariate classification.

The specific multivariate technique chosen for this trigger line is the Boosted Decision Tree (BDT). A decision tree is a multivariate classifier that is built by performing repetitive one-dimensional splits of the data. In Figure 4.11 a schematic view of a decision tree is shown. It requires a set of input variables and a signal-like and a background-like data sample. In the training stage the separation criteria for each node are defined. Starting from the root node, a sequence of binary splits using the discriminating variables is applied to the data. Each split uses the variable that at this node gives the best

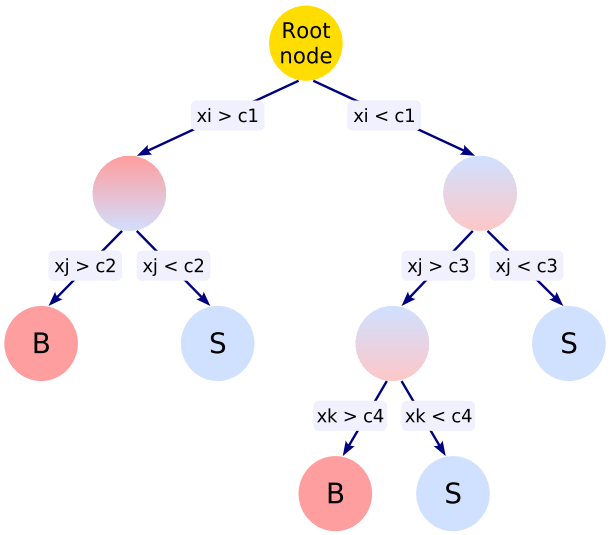

Figure 4.11: Schematic view of a decision tree. Starting from the root node, a sequence of binary splits using the discriminating variables x_i x_j x_k is applied to the data. The leaf nodes at the bottom end of the tree are labeled S for signal and B for background.

separation between signal and background when being cut on. The leaf nodes at the bottom end of the tree are labeled as signal or background depending on the majority of events that end up in the respective nodes. In this, they are similar to rectangular cuts. However, whereas a cut-based analysis is able to select only one hypercube as region of phase space, the decision tree is able to split the phase space into a large number of hypercubes, each of which is identified as either signal-like or background-like. A weak point of decision trees is their instability with respect to statistical fluctuations in the training sample from which the tree structure is derived. A small change in the training data can produce a large change in the tree. This is remedied by the use of boosting, in this thesis the AdaBoost algorithm in particular. The training events which were misclassified (a signal event fell on a background leaf or viceversa) have their weights increased (boosted) and a new tree is formed. This procedure is then repeated for the new tree. In this way many trees are built up, the so called forest is formed. Boosting increases the statistical stability of the classifier and typically also improves the separation performance compared to a single decision tree.

4.3.1 Input variables

The first step to train the BDT is the definition of the background and of the signal sample. As background we can simply use the candidates reconstructed with the preliminary cuts from the Minimum Bias data sample as defined in section 4.2. For the signal sample the question is more tricky. We have to deal with 13 samples at the same time, thus we need to find the best way how to include each one in a single dataset. One possibility would be to weight each Monte Carlo sample with its branching ratio. In this way we would obtain a dataset similar to the expected physical one, but we would lose efficiency for the most rare decays. Instead, we choose to use the same proportion of events from each Monte Carlo signal sample in order to train the BDT to recognize also the rare decays modes.

To exploit the most out of the potential of the BDT we have to carefully choose the input variables. To preserve the inclusive nature of this trigger we have to choose only variables which ensure that the multivariate classifier is learning common D^{*+} decay traits and not a large sum of specific ones. Thus, for example, we avoid to use the mass of the particles as input variable because, in the way we reconstruct the candidates, it heavily change from channel to channel. Moreover, we have to use variables less correlated as possible. In fact the use of two correlated variables does not lead to any new information compared to the use of a single one. But at the same time we have to look for the best discriminating variables between the background and the signal.

To do so, we compare the background variables distributions to every signal variables distributions for each particle involved in the decay chain. Once studied all the plots, we select a total of seven input variables which are the most discriminating among the possible ones. These are the D^{*+} DOCA, the D^{*+} flight distance, the D^0 flight distance and vertex χ^2, the π_s^+ p_T and $cos\vartheta$ and the sum of the p_T of the two tracks. The D^{*+} variables allow to check the vertex quality thanks to the DOCA variable and to discriminate long lived particle with respect to the D^{*+} thanks to the flight distance. The long lifetime of the D^0 is exploited using the D^0 flight distance; the D^0 vertex χ^2 allows to require only the well reconstructed particles. Both the p_T and the $cos\vartheta$ of the π_s^+ show a great separation between the background and the signal. The p_T for the signal is much better peaked with respect to the background. It is due to the kinematics of the D^{*+} decay, the difference of mass between the D^{*+} and the D^0 is small and it leads to a low π_s^+ momentum. The $cos\vartheta$ distribution is sensitive to the polarization of the particle. For the π_s^+ for a full reconstructed decay (as for $D^{*+} \to D^0(K^-\pi^+\pi^0)\pi_s^+$) it is flat because the π_s^+ is not polarized. In the case of not completely reconstructed candidates there is a peak for $\vartheta = \pi$, due to the not fully reconstructed D^{*+} p_T. In the

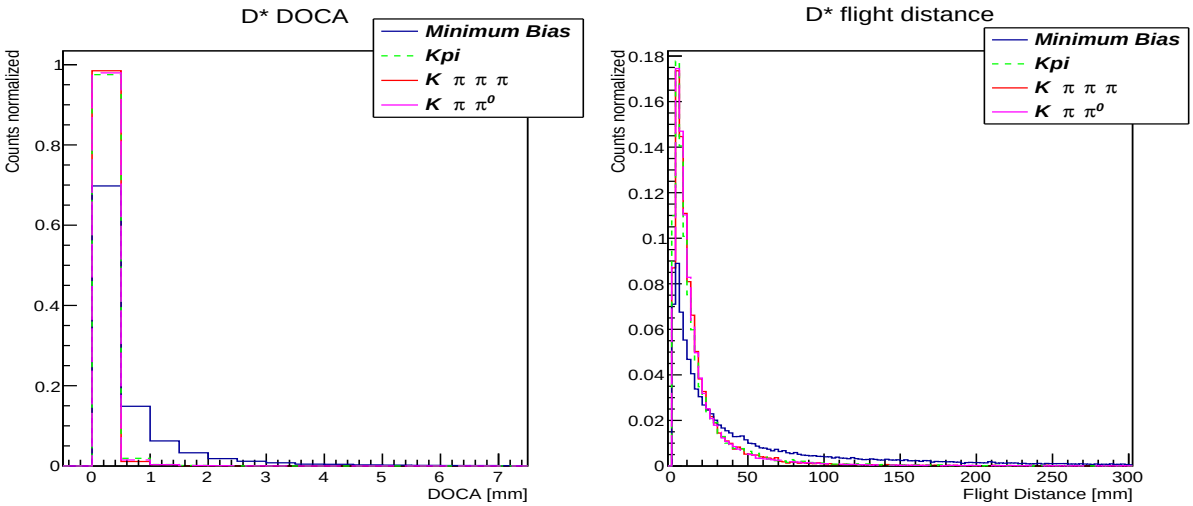

Figure 4.12: D^{*+} distributions of the $D^{*+} \rightarrow D^0(K^-\pi^+)\pi_s^+$ (green), $D^{*+} \rightarrow D^0(K^-\pi^+\pi^-\pi^+)\pi_s^+$ (red), $D^{*+} \rightarrow D^0(K^-\pi^+\pi^0)\pi_s^+$ (pink) MC signal sample and of the Minimum Bias data sample (blue). From left: P_T, flight distance.

$Cos\vartheta$ background distribution instead, it is visible a double peak distribution. Values of $\vartheta = 0$ and $\vartheta = \pi$ are preferred. The sum of p_T of the two tracks allows to discriminate the tracks really coming from the D^0 which on average with a higher transverse momentum with respect to the background.

To show the behavior of these discriminating variables we plot the comparison between the background sample (blue) and three different kinds of Monte Carlo signal samples: $D^{*+} \rightarrow D^0(K^-\pi^+)\pi_s^+$ (green), $D^{*+} \rightarrow D^0(K^-\pi^+\pi^-\pi^+)\pi_s^+$ (red) and $D^{*+} \rightarrow D^0(K^-\pi^+\pi^0)\pi_s^+$ (pink). In Figure 4.12 are shown the D^{*+} DOCA and flight distance, in Figure 4.13 the D^0 vertex χ^2 and flight distance, in Figure 4.14 the π_s p_T and $cos\vartheta$ and in Figure 4.15 the sum of the p_T of the two tracks.

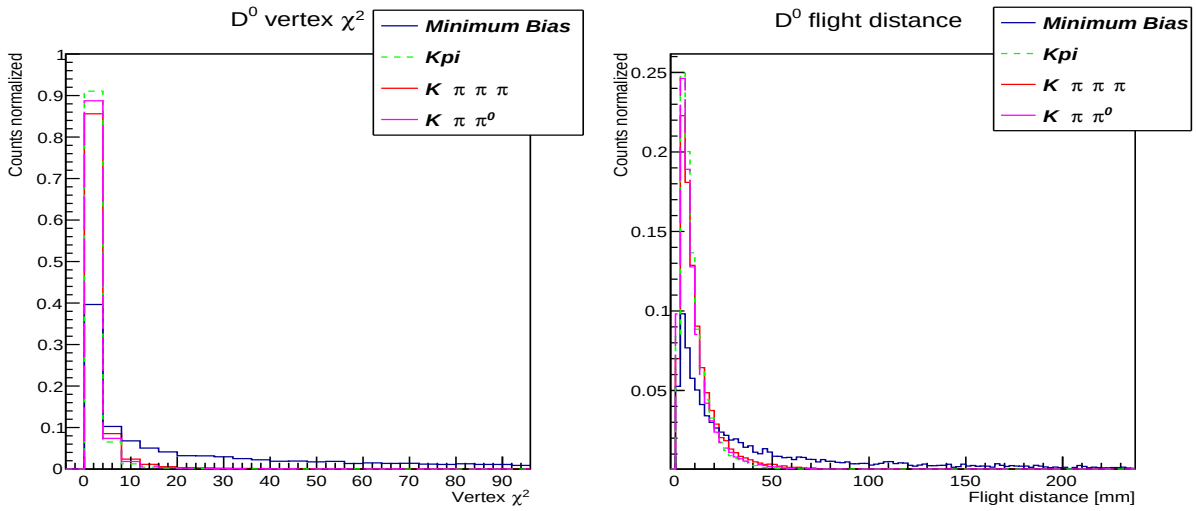

Figure 4.13: D^0 distributions of the $D^{*+} \to D^0(K^-\pi^+)\pi_s^+$ (green), $D^{*+} \to D^0(K^-\pi^+\pi^-\pi^+)\pi_s^+$ (red), $D^{*+} \to D^0(K^-\pi^+\pi^0)\pi_s^+$ (pink) MC signal sample and of the Minimum Bias data sample (blue). From left: vertex χ^2, flight distance.

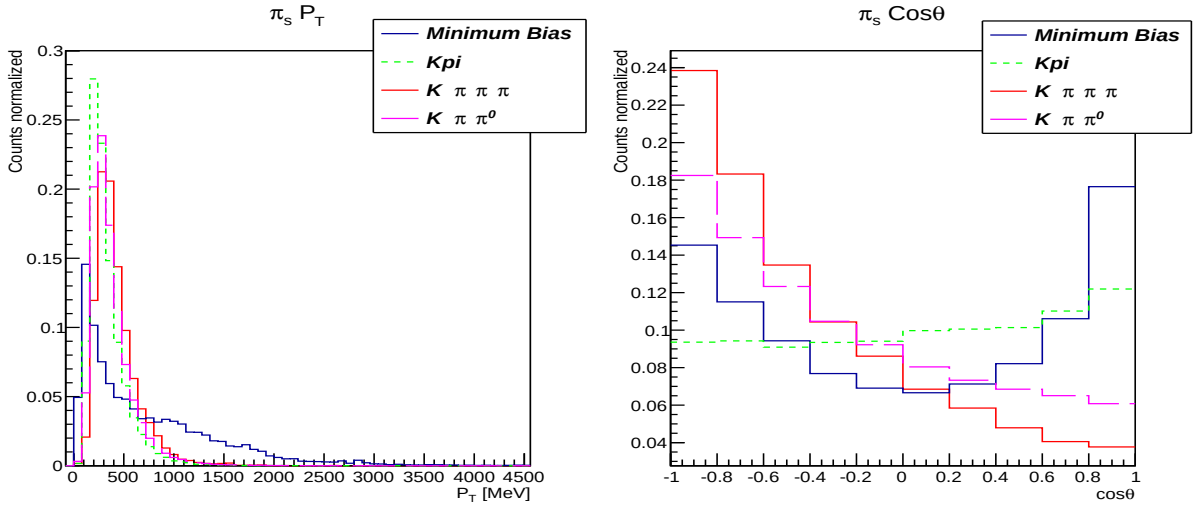

Figure 4.14: π_s^+ distributions of the $D^{*+} \to D^0(K^-\pi^+)\pi_s^+$ (green), $D^{*+} \to D^0(K^-\pi^+\pi^-\pi^+)\pi_s^+$ (red), $D^{*+} \to D^0(K^-\pi^+\pi^0)\pi_s^+$ (pink) MC signal sample and of the Minimum Bias data sample (blue). From left: P_T, cosine of the helicity angle.

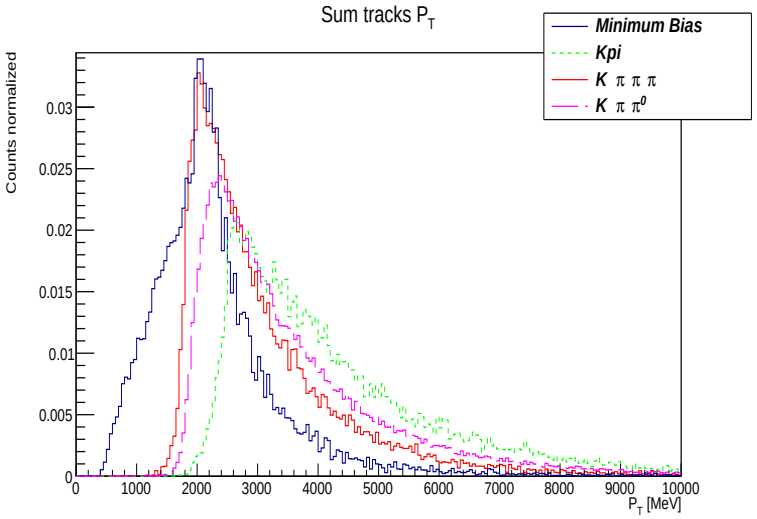

Figure 4.15: Sum of the two tracks p_T distributions of the $D^{*+} \to D^0(K^-\pi^+)\pi_s^+$ (green), $D^{*+} \to D^0(K^-\pi^+\pi^-\pi^+)\pi_s^+$ (red), $D^{*+} \to D^0(K^-\pi^+\pi^0)\pi_s^+$ (pink) MC signal sample and of the Minimum Bias data sample (blue).

4.3.2 The BDT training

Once defined the background and the signal dataset and the input variables in the way explained in the previous section we are able to move to the BDT training. Figure 4.16 shows the D^{*+} input variables, in blue the background sample superimposes to the signal sample obtained merging all the 13 Monte Carlo samples (red). The same for the D^0, π_s^+ and tracks in Figure 4.17, 4.18 and 4.19 respectively.

At the beginning of the analysis, the training sample is split into two sub-samples. The split of the given sample is necessary to provide statistical independence for the training and testing phase. The training phase sets a weight to each n-dimensional region of the phase space of the n input variables, which is evaluated through a series of decision trees exploiting the signal and the background samples as described in section 4.3. These weights carry the information about the background or signal nature of the reconstructed candidates which belong to these phase space regions. Once the training is finished, a testing phase starts with the second sample, when the test events are classified using the weight files previously built. The testing results are really important, they are used to measure the performance of the BDT and to optimize its parameters.

For the training we used 240000 candidates for the background and 240000 for the signal sample. Figure 4.20 shows the linear correlation among the input variables for

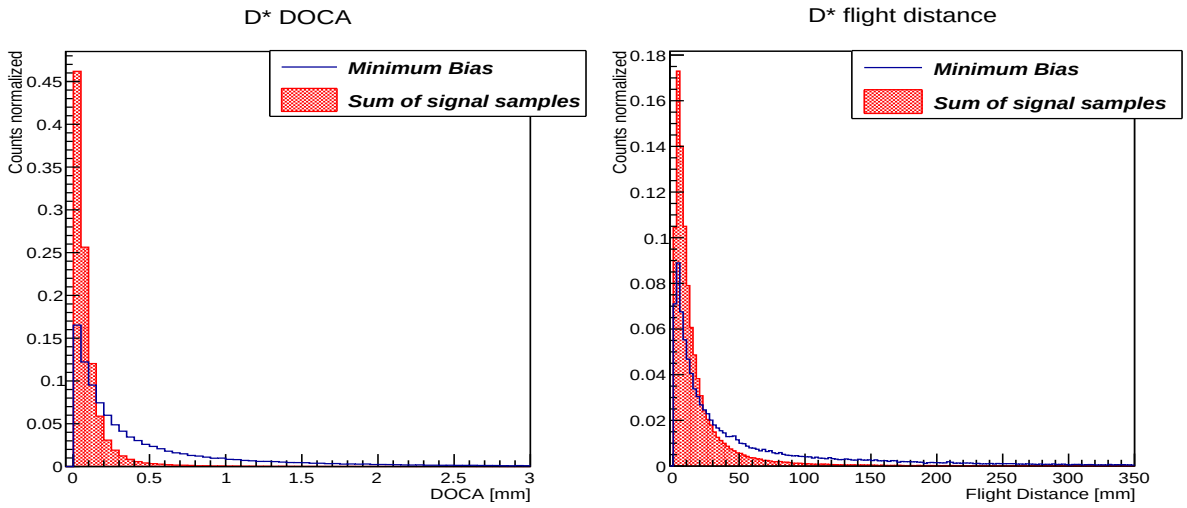

Figure 4.16: D^{*+} input variables. Blue background, red signal sample. From left: P_T, flight distance.

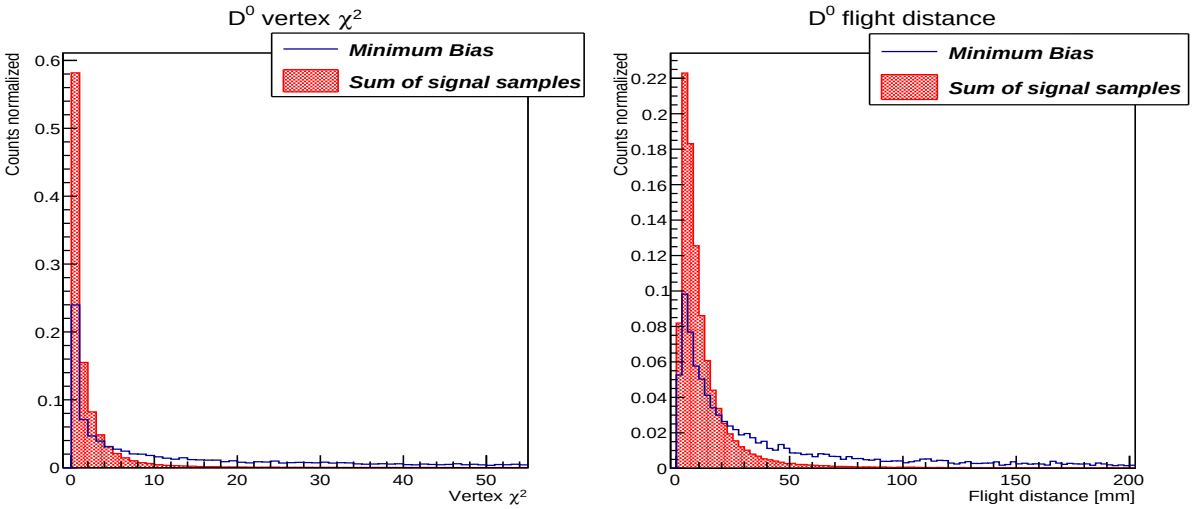

Figure 4.17: D^0 input variables. Blue background, red signal sample. From left: vertex χ^2, flight distance.

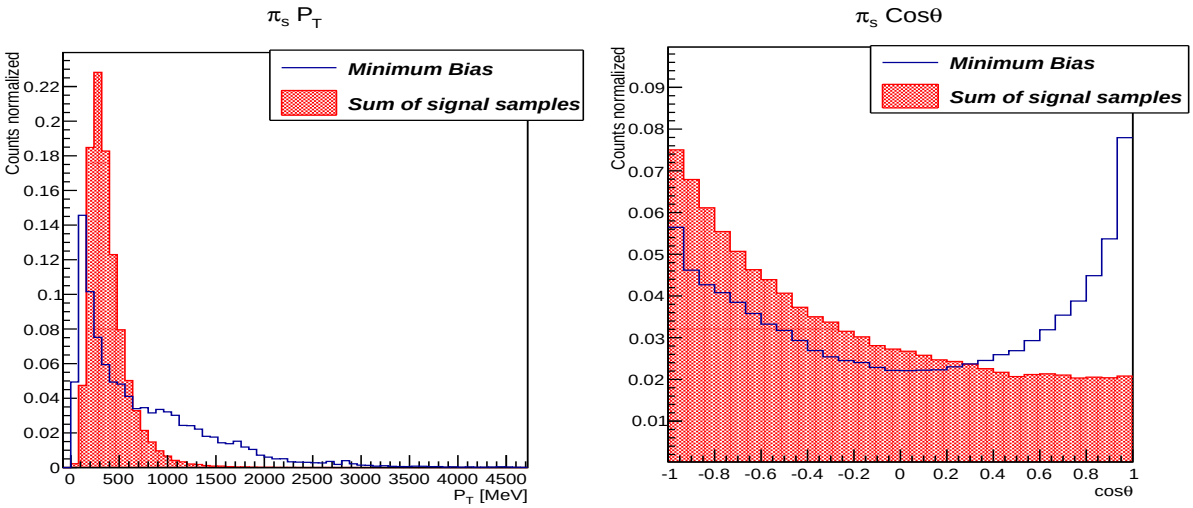

Figure 4.18: π_s^+ input variables. Blue background, red signal sample. From left: P_T, cosine of the helicity angle.

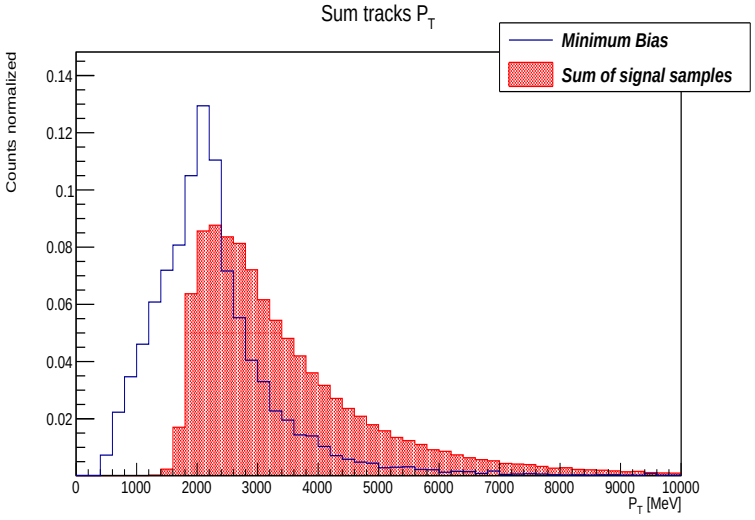

Figure 4.19: Sum of the two tracks p_T input variable. Blue background, red signal sample

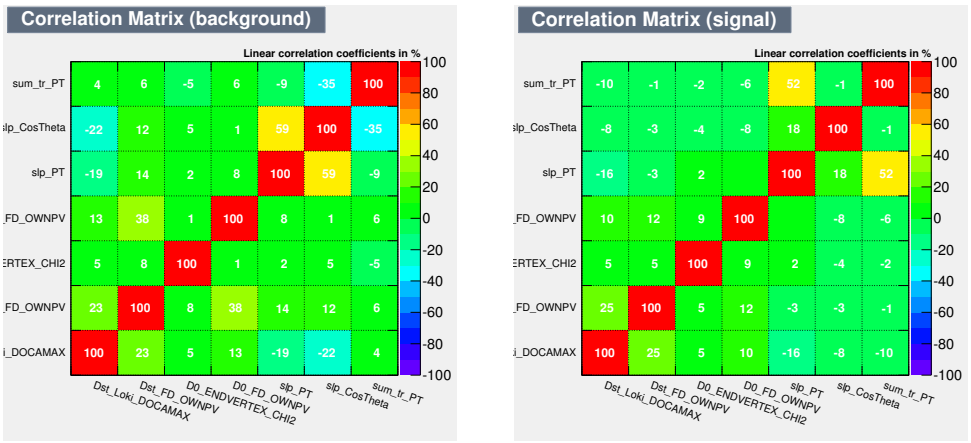

(a) (b)

Figure 4.20: Input variables correlation for the background (a) and the signal sample (b)

background (left) and for signal (right). The only remarkable, but still acceptable correlations, are between the π_s^+ $cos\vartheta$ and p_T for the background sample and between the π_s^+ and the two tracks p_T for the signal sample. In Figure 4.21 the so-called overtraining check plot is shown. It is used to get a more detailed view on the performance of the separation criteria. An overtraining check is based on the classifier response for the signal and background candidates of both training and testing samples. All four distributions are superimposed such that the differences between training and testing can be seen. If great differences are present it could mean that the multivariate classifier suffers of overtraining. It occurs when a machine learning problem has too few degrees of freedom, because too many model parameters of an algorithm were adjusted to too few data points. When this happens, the BDT learns so well the properties of the specific training samples that it loses the ability of separate signal and background in any other sample. Thus, this plot is therefore a measure for the trustworthiness of the training process. The distributions created during the training and the testing sessions result very similar, suggesting that the training phase has successfully completed. Figure 4.21 shows also the good separation obtained between background (red) and signal (blue).

Another important plot is shown in Figure 4.22. It represents the signal and the background efficiency and the signal purity as function of the BDT output. It is the key plot to choose the BDT response cut value to discriminate signal from background. All the candidates marked with a weight smaller than the selected cut value are classified as background and viceversa. Of course we want to choose a cut value which maximizes the

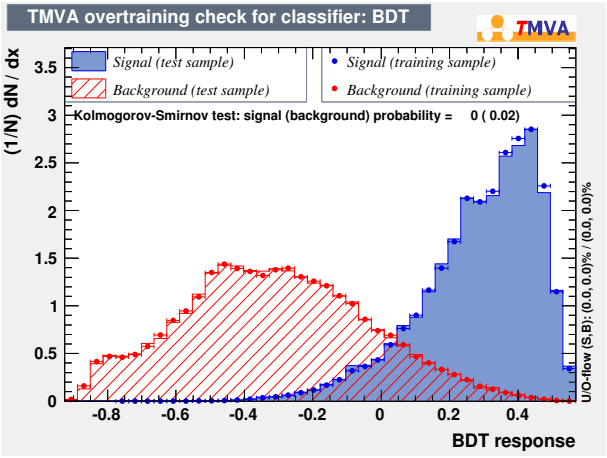

Figure 4.21: Classifier response for boosted decision trees

background rejection for the signal efficiency. A good estimator is the signal significance, which is the ratio between signal and the uncertainty on the whole dataset ($\frac{S}{\sqrt{S+B}}$); in this case it is maximum at a BDT cut value of 0. This cut will be adjusted in next chapter taking into account the output rate of the trigger.

4.3.3 Bonsai Boosted Decision Tree

The multivariate selection algorithms are complexed tools. Given an input, they return an output evaluated in a really difficult way to understand and control. It leads to some concerns which need to be addressed prior to using such a classifier in an HLT algorithm. One difficulty that needs to be overcome is that the selected signal n-dimensional regions of the multivariate space could be small relative to the resolution or stability of the detector. This could cause the signal to oscillate in and out of these regions resulting in a less efficient and very difficult to control trigger [54]. Another concern is that the BDT due to its complexity, can take a long time to evaluate the response for each event. Any HLT algorithm must run in the on-line environment; thus, it must be extremely fast.

To overcome these issues, we decide to move to a Bonsai Boosted Decision Tree (BBDT) [54]. The proposed way to address these concerns is to discretize all of the variables used in the BDT. It means to define a finite number of intervals with fixed limits for every input variables. The value of variable is then set to the midpoint between these limits. This limits where the BDT can split the data and permits a better control of the growth and shape of the decision tree. For this reason this method is called Bonsai Boosted Decision Tree. It has been already successfully implemented for the topological

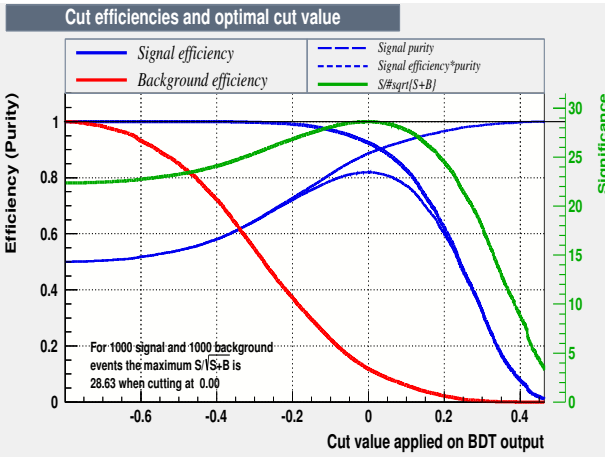

Figure 4.22: Signal and background efficiency and signal purity as function of the BDT cut value

B trigger in LHCb [55].

There are some constraints driving the choice of the these intervals. The minimum width should be greater than the variable detector resolution and large with respect to its expected on-line variations. The discretization should reflect the properties of the training signal distributions that have to be exploited. For example, as the BBDT is meant to be inclusive, the discretization should ensure that the BBDT learns the common traits shared by all signals of a given type, such as a long D^0 lifetime or a peaked π_s^+ p_T distribution.

Discretization means that the data are binned. Thus, the n-dimensional phase space of the input variables is subdivided into a finite and limited number of possible keep regions ($\sim$ 250000). The BBDT response values, each corresponding to one of these regions, are then stored in memory. Then the complex operations that a BDT have to run in order to obtain a response for each candidate can be converted into a simple one dimensional look up table. This speeds up the whole system, one dimensional array of response values speeds are extremely fast. For the possibility to control the growth of the decision tree and the considerable speed up that it permits, the BBDT perfectly fits for our purpose.

In Table 4.4 the input variables discretization is shown. The criteria that have been met for the choice of the splitting values are: the interval have to be greater than the LHCb resolution and as much dense as possible where the variable variation is more pronounced, to not to lose information carried by the variable distributions. But at the same time it is also important to limit the number of bins, to maintain small the

Particle	variable	Limits of allowed interval
D^*	DOCA [mm]	0, 0.05, 0.1, 0.5, 5
D^*	Flight distance [mm]	0, 5, 10, 20, 50, 100, 1000
D^0	Vertex χ^2	0, 1, 2, 5, 10, 100
D^0	Flight distance [mm]	0,10, 30, 40, 50, 100, 300, 2000
π_{sl}	$Cos\vartheta$	-1,-0.75,-0.5,-0.25,0,0.25,0.50,1
π_{sl}	p_T [MeV/c]	0, 50, 100, 300, 750, 1500, 5000
$\sum_{i=1}^{2} tr_i$	p_T [MeV/c]	0, 1000, 1500, 2000, 3000, 5000, 10000, 30000

Table 4.4: Variables discretization: limits of the intervals

dimension of the look up table small in order to be able to store it in the PC memory. IP resolution reaches 14 µm for tracks with a large transverse momentum, ~ 50 µm for tracks with a small transverse momentum. This allows the choice of 50 µm as smallest width for the DOCA discretization. The D^{*+} and D^0 flight distance discretization is chosen in order to well describe their rapid decrease as function of the distance. It is important to keep this information to well discriminate the real particles from fake particles and background. LHCb has an excellent momentum resolution of $\frac{\delta p}{p} = 0.5\%$ over a wide momentum range. This allows us to use 50 MeV/c as smallest width for the π_s^+ p_T discretization.

Once discretized the input variables we move to the BBDT training. The background and signal samples are the same as before. Figure 4.23 shows the discrete D^{*+} DOCA and flight distance distributions for the background (blue) and for the signal (red). With the same color the comparison between the discrete D^0, π_s^+ and tracks background and signal distributions in Figure 4.24, 4.25 and 4.26 respectively.

We train the BBDT with the same options used for the BDT training. The only difference with respect to the BDT training is the discretization of the input variables. In Figure 4.27 the overtraining check plot is shown. In the discretization process there is an inevitably loss of information about the discrimination power of the input variables, which could lead to a loss in the BBDT power separation between background and signal. But this effect does not appear in our training, the separation performance with respect to the BDT (Figure 4.21) are very similar. In Figure 4.28, where the signal and the background efficiency and the signal purity as function of the BBDT response is shown, it appears even more clear. Comparing this figure with the same plot for the BDT (Figure 4.22), we can conclude that the separation and the efficiency performance of the two methods, BDT and BBDT are comparable. Considering all the advantages of the BBDT, previously listed, we will base our trigger line on this tool.

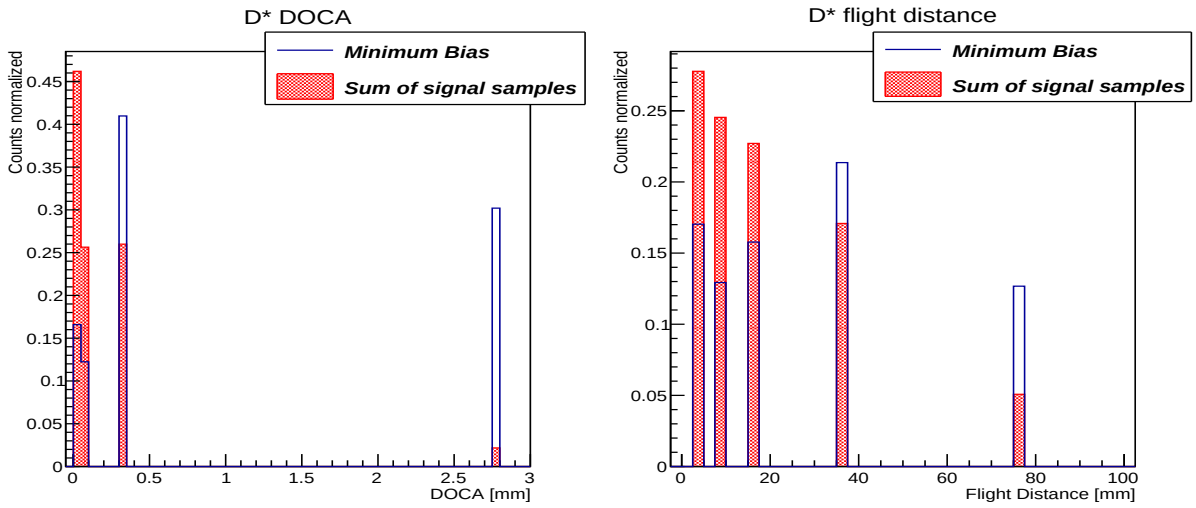

Figure 4.23: D^{*+} discrete input variables. Blue background, red signal sample. From left: P_T, flight distance.

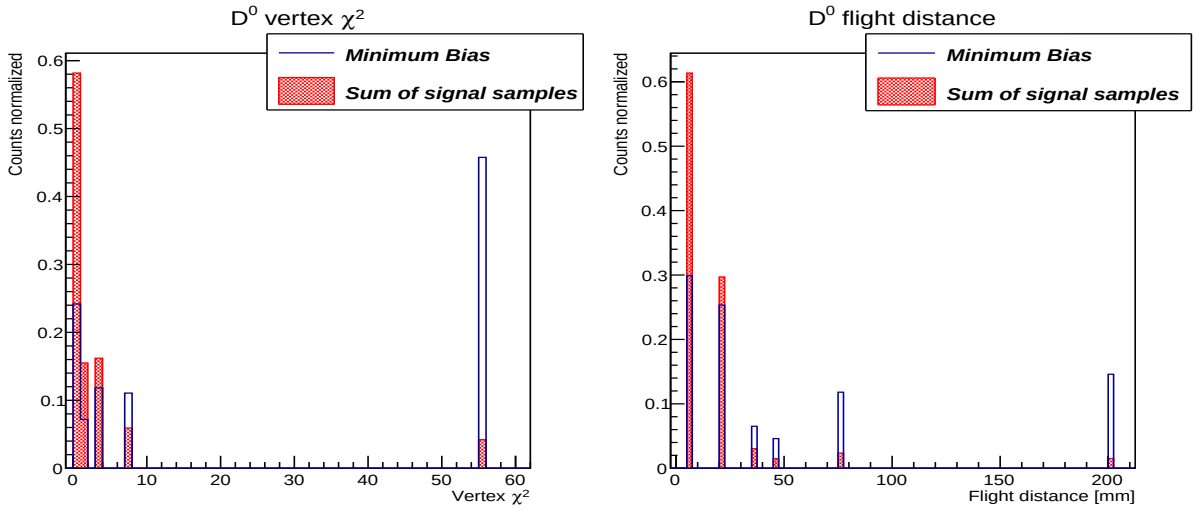

Figure 4.24: D^0 discrete input variables. Blue background, red signal sample. From left: vertex χ^2, flight distance.

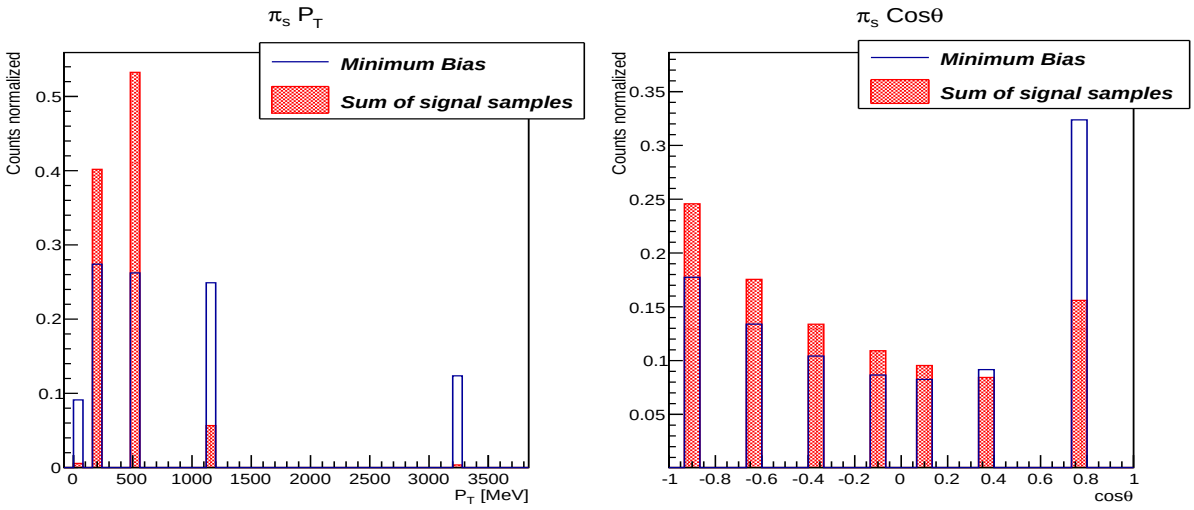

Figure 4.25: π_s^+ discrete input variables. Blue background, red signal sample. From left: P_T, cosine of the helicity angle.

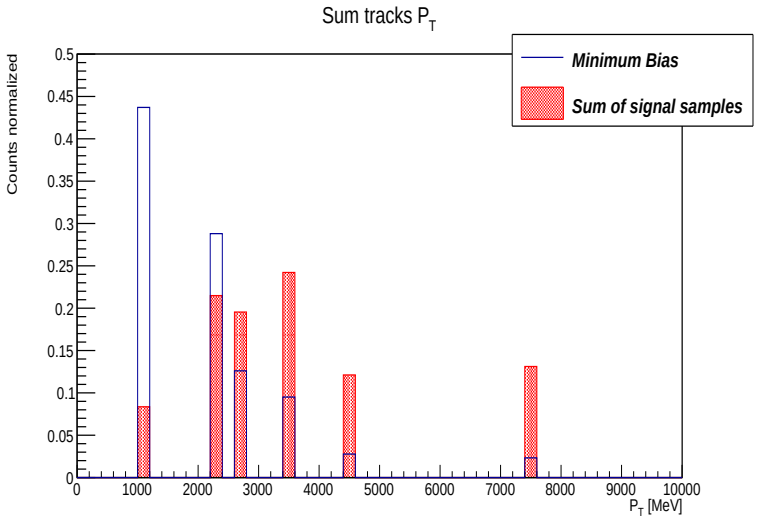

Figure 4.26: Sum of the two tracks p_T discrete input variable. Blue background, red signal sample

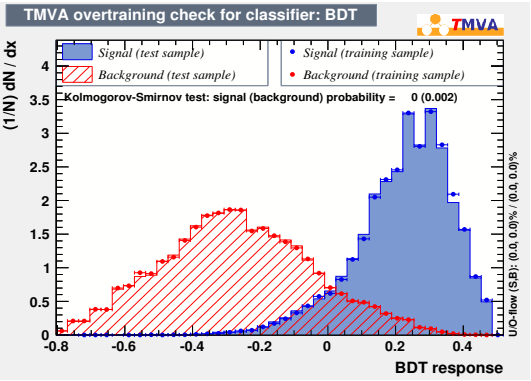

Figure 4.27: Classifier response for the Bonsai boosted decision trees

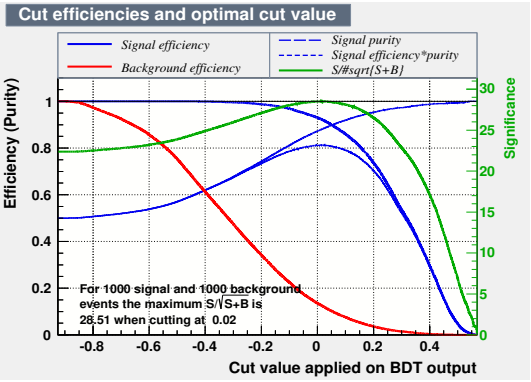

Figure 4.28: Signal and background efficiency and signal purity as function of the BBDT cut value

Chapter 5

Trigger performance

The most important features for a trigger are the final acquisition rate and the efficiency on signals. Each HLT2 line has to collect events within a well defined rate. In 2012 the total trigger rate after the HLT2 was about 5 kHz [48], about 2 kHz of which dedicated to charm lines.

In 2015, due to the greater pp collision energy, the events production rate will increase. This means that also the trigger performance have to improve, in order to get at least the same background rejection, as introduced in Chapter 2. The rate for charm triggers will be enhanced up to 6 kHz, about 2.5 kHz of which dedicated to the inclusive D^{*+}. [56]

Thus the trigger developed in this thesis, which will collect events starting from the 2015 collision run, must at least equal the performance of the current D^{*+} inclusive trigger. Using the 2012 dataset we check the performances of the multivariate technique based D^{*+} trigger and compare them to the 2012 performances of the current line. The first section of this chapter explains how we get the trigger rate and efficiencies for some signal channels and shows the results. The second section describes some studies on the variables distributions of the candidates.

We will perform the same performances tests on 2015 Monte Carlo minimum bias and signals samples as soon as they will be produced.

5.1 Background and signal efficiency

All the studies on efficiency and rate that we present for the HLT2 trigger developed in this project have been made using candidates off-line reconstructed, using all the sub-detectors information and exploiting all the computation power. However, these

numbers are a faithful estimate of the on-line efficiencies and rates. In fact, at the HLT2 stage the candidates are fully reconstructed, there are only small differences with respect to off-line tracking where the limitations come from the computing time requirements [57].

We are interested on both the efficiency on background, which gives us an estimate on the final rate, and the efficiency on the different signals. To get the efficiency on background we exploit the Minimum Bias sample already used for BBDT training. After applying the L0 and the HLT1, we reconstruct the events requiring the preliminary cuts. As the last step is the application of the BBDT, we analyze the efficiency of this step as function of the BBDT cut value. The efficiencies for each trigger level are then evaluated as the ratio between the number of events that pass that level with respect to the number of events that pass the previous trigger level.

For what concerns the L0 we select only events that pass any L0 selection. The evaluated efficiency on background for the L0 is $(0.845 \pm 0.003)\%$. Another filter selects only events that pass the HLT1TrackAllL0 HLT1 trigger line. Its efficiency is $(5.68 \pm 0.10)\%$. All the events coming from the HLT1TrackAllL0 line are then passed to the preliminary cuts stage. Here all the D^{*+} candidates are reconstructed using the reconstruction strategy described in section 3.2. Only the candidates that pass the preliminary cuts are then analyzed by the BBDT. The variables used as input by the BBDT are discretized following the discretization table (Table 4.4) and each candidate is assigned to one region of the phase space of the input variables, each one corresponding to a BBDT output value. The efficiency for different BBDT output values is then evaluated.

The trigger selects the whole event anytime a signal candidate is found, but multiple signal candidates can been contained into the event. To obtain the efficiency for the preliminary cuts and the BBDT phases thus we need to convert the number of candidates into number of events. To do so we use the event number and the run collision number; using the combination of the two we get an univocal way to check if a signal candidates is part of an already selected event.

The evaluated efficiency for the preliminary cuts is $(83.3 \pm 2.0)\%$. For the BBDT phase it is included between $(17.8 \pm 0.9)\%$ with a BBDT cut of 0.31 and $(0.4 \pm 0.1)\%$ with a 0.45 BBDT cut. In Table 5.1 the efficiency for each level and for different BBDT output cuts are listed. The absolute efficiency is shown besides the efficiency with respect to the previous level.

Once we know the efficiency for each trigger level we can get the relative rate. In fact the output rate of the L0 is set to 1 MHz [58], thus we can evaluate the rate for each

Trigger level	Number of events	ε wrt previous level	ε_{abs}
No trigger	7610836	1	1
L0	64345	$(8.45\pm0.03) \times 10^{-3}$	$(8.45\pm0.03) \times 10^{-3}$
HLT1	3653	$(5.68\pm0.10) \times 10^{-2}$	$(4.80\pm0.08) \times 10^{-4}$
Preliminary cuts	3044	$(83.1\pm2.0) \times 10^{-2}$	$(4.00\pm0.12) \times 10^{-4}$
BBDT cut 0.31	483	0.18 ± 0.01	$(7.11\pm0.41) \times 10^{-5}$
BBDT cut 0.33	350	0.13 ± 0.01	$(5.15\pm0.33) \times 10^{-5}$
BBDT cut 0.35	236	0.09 ± 0.01	$(3.47\pm0.30) \times 10^{-5}$
BBDT cut 0.37	150	0.055 ± 0.005	$(2.21\pm0.20) \times 10^{-5}$
BBDT cut 0.39	69	0.025 ± 0.003	$(1.02\pm0.13) \times 10^{-5}$
BBDT cut 0.41	50	0.018 ± 0.003	$(7.36\pm1.07) \times 10^{-6}$
BBDT cut 0.43	30	0.011 ± 0.002	$(4.42\pm0.82) \times 10^{-6}$
BBDT cut 0.45	11	0.004 ± 0.001	$(1.61\pm0.49) \times 10^{-6}$

Table 5.1: The efficiencies on background for each trigger level and some BBDT output cuts

level as:

$$rate[i] = rate[i-1] * \varepsilon[i] \tag{5.1}$$

where i indicates the i-th trigger level. Table 5.2 shows the rates for each level and some BBDT output cut values, the errors are statistical. We set 1 MHz as output rate of the L0, neglecting any errors. Thus the error for each level is underestimated.

In 2012 the HLT2CharmHadD02HHXDst_hhX rate was about 840 Hz [56]. Thus, if we set our BBDT output cut value at 0.41 we get a final rate of 870 ± 25, compatible with the current trigger line rate. The cut at this BBDT value allows us to compare also the efficiency on signals of our trigger line to the current trigger ones. These efficiencies on signals describe the power of the trigger line to correctly recognize and select the signal candidates.

To get these efficiencies we apply our trigger selection to the Monte Carlo signal samples, requiring the D^{*+} candidates to be matched to the true candidates. The efficiency is evaluated exactly as for the background sample. For the current trigger line it has been possible to evaluate the efficiency on signal only for the 2012 samples. In fact only these events carry information about the HLT2CharmHadD02HHXDst_hhX trigger line, as this selection was introduced only in 2012. Table 5.3 shows the efficiencies for the preliminary cuts and different BBDT cuts values for the $D^{*+} \to D^0(\mu^+\mu^-)\pi_s^+$ decay chain. Last line of the table shows the efficiency for the current line. We have

Trigger level	rate [Hz]
L0	1×10^6
HLT1	$(56.8 \pm 1.0) \times 10^3$
Preliminary cuts	$(47.3 \pm 1.4) \times 10^3$
BBDT cut 0.31	$(8.41 \pm 0.25) \times 10^3$
BBDT cut 0.33	$(6.09 \pm 0.18) \times 10^3$
BBDT cut 0.35	$(4.11 \pm 0.12) \times 10^3$
BBDT cut 0.37	$(2.61 \pm 0.08) \times 10^3$
BBDT cut 0.39	$(1.20 \pm 0.04) \times 10^3$
BBDT cut 0.41	870 ± 25
BBDT cut 0.43	522 ± 15
BBDT cut 0.45	192 ± 5

Table 5.2: Rates on background for each trigger level and some BBDT output cuts

to compare the absolute efficiency of our line at BBDT output cut value of 0.41 to the HLT2CharmHadD02HHXDst_hhX absolute efficiency. Tables 5.4, 5.5 and 5.6 show the same quantities for the $D^{*+} \to D^0(K^+\pi^-\pi^+\pi^-)\pi_s^+$, $D^{*+} \to D^0(K_s^0(\pi^+\pi^-)K^+K^-)\pi_s^+$ and $D^{*+} \to D^0(K^+\mu^-\nu_\mu)\pi_s^+$ decay modes. These tables show that our trigger line gains in efficiency for the 4 bodies decays with respect to the current line (0.10 ± 0.01 and 0.05 ± 0.01 versus 0.038 ± 0.003 and 0.020 ± 0.001), while we lose a little in efficiency for 3 and 2 bodies decays.

These results are encouraging, even though only preliminary and obtain on off-line reconstructed events. We gain about a factor 2 in efficiency for the 4 bodies hadronic decays modes with respect to the current inclusive trigger line. With more studies on the preliminary cuts we expect a little improvement in the performance also for the 3 and 2 bodies decays modes.

5.2 Variables distributions of selected events

Applying our trigger selection to the Minimum Bias sample we can obtain a dataset similar to the one we could obtain on-line. In this section we give a first glimpse to the variables distributions of the events collected by our trigger line, to check if the developed line is affected by some macroscopic bias.

We first compare the minimum bias candidates recognized as signal by the BBDT, thus with BBDT output greater than 0 with respect to the minimum bias candidates

	Number of events	ε wrt previous level	ε_{abs}
L0 & HLT1	2861	1	1
Preliminary cuts	2461	0.86 ± 0.02	0.86 ± 0.02
BBDT cut 0.31	762	0.31 ± 0.01	0.27 ± 0.01
BBDT cut 0.33	638	0.26 ± 0.01	0.22 ± 0.01
BBDT cut 0.35	496	0.20 ± 0.01	0.17 ± 0.01
BBDT cut 0.37	365	0.15 ± 0.01	0.13 ± 0.01
BBDT cut 0.39	263	0.11 ± 0.01	0.27 ± 0.01
BBDT cut 0.41	**202**	$\mathbf{0.08 \pm 0.01}$	$\mathbf{0.07 \pm 0.01}$
BBDT cut 0.43	123	0.055 ± 0.004	0.043 ± 0.004
BBDT cut 0.45	67	0.029 ± 0.003	0.023 ± 0.0003
HLT2CharmHadD02HHXDst_hhX		$\mathbf{0.120 \pm 0.003}$	$\mathbf{0.120 \pm 0.003}$

Table 5.3: Efficiency of HLT2 on signal: $D^{*+} \to D^0(\mu^+\mu^-)\pi_s^+$

	Number of events	ε wrt previous level	ε_{abs}
L0 & HLT1	3962	1	1
Preliminary cuts	3775	0.95 ± 0.02	0.95 ± 0.02
BBDT cut 0.31	1777	0.47 ± 0.01	0.45 ± 0.01
BBDT cut 0.33	1473	0.39 ± 0.01	0.37 ± 0.01
BBDT cut 0.35	1140	0.29 ± 0.01	0.28 ± 0.01
BBDT cut 0.37	812	0.22 ± 0.01	0.20 ± 0.01
BBDT cut 0.39	581	0.15 ± 0.01	0.15 ± 0.01
BBDT cut 0.41	**388**	$\mathbf{0.10 \pm 0.01}$	$\mathbf{0.10 \pm 0.01}$
BBDT cut 0.43	208	0.055 ± 0.004	0.052 ± 0.004
BBDT cut 0.45	111	0.029 ± 0.003	0.028 ± 0.003
HLT2CharmHadD02HHXDst_hhX		$\mathbf{0.038 \pm 0.003}$	$\mathbf{0.038 \pm 0.003}$

Table 5.4: Efficiency of HLT2 on signal: $D^{*+} \to D^0(K^+\pi^-\pi^+\pi^-)\pi_s^+$

	Number of events	ε wrt previous level	ε_{abs}
L0 & HLT1	3962	1	1
Preliminary cuts	3775	0.90 ± 0.04	0.90 ± 0.04
BBDT cut 0.31	283	0.29 ± 0.02	0.27 ± 0.02
BBDT cut 0.33	229	0.24 ± 0.02	0.22 ± 0.02
BBDT cut 0.35	174	0.18 ± 0.02	0.17 ± 0.01
BBDT cut 0.37	104	0.11 ± 0.01	0.10 ± 0.01
BBDT cut 0.39	79	0.08 ± 0.01	0.08 ± 0.01
BBDT cut 0.41	**53**	$\mathbf{0.06 \pm 0.01}$	$\mathbf{0.05 \pm 0.01}$
BBDT cut 0.43	28	0.03 ± 0.01	0.03 ± 0.01
BBDT cut 0.45	14	0.015 ± 0.004	0.013 ± 0.003
HLT2CharmHadD02HHXDst_hhX		$\mathbf{0.020 \pm 0.001}$	$\mathbf{0.020 \pm 0.001}$

Table 5.5: Efficiency of HLT2 on signal: $D^{*+} \to D^0(K_s^0(\pi^+\pi^-)K^+K^-)\pi_s^+$

	Number of events	ε wrt previous level	ε_{abs}
L0 & HLT1	1262	1	1
Preliminary cuts	1094	0.87 ± 0.04	0.87 ± 0.04
BBDT cut 0.31	338	0.31 ± 0.02	0.27 ± 0.02
BBDT cut 0.33	261	0.24 ± 0.02	0.21 ± 0.01
BBDT cut 0.35	193	0.18 ± 0.01	0.15 ± 0.01
BBDT cut 0.37	145	0.13 ± 0.01	0.11 ± 0.01
BBDT cut 0.39	102	0.09 ± 0.01	0.08 ± 0.01
BBDT cut 0.41	**58**	$\mathbf{0.05 \pm 0.01}$	$\mathbf{0.05 \pm 0.01}$
BBDT cut 0.43	29	0.027 ± 0.005	0.02 ± 0.004
BBDT cut 0.45	5	0.004 ± 0.002	0.003 ± 0.002
HLT2CharmHadD02HHXDst_hhX		$\mathbf{0.107 \pm 0.002}$	$\mathbf{0.107 \pm 0.002}$

Table 5.6: Efficiency of HLT2 on signal: $D^{*+} \to D^0(K^+\mu^-\nu_\mu)\pi_s^+$

recognized as background, with BBDT output less than 0. With this study we can evaluate the separation power of the BBDT. Then we will compare the minimum bias candidates recognized as signal by the BBDT with a tighter BBDT output of 0.3 with respect to a Monte Carlo signal sample, in order to study in details the signal properties.

Figure 5.1 shows some D^0 and D^{*+} variables distributions, in red for candidates recognized by the BBDT as background (BBDT cut value < 0), in blue for candidates recognized as signal (BBDT cut value > 0). The most interesting distribution is the difference of mass between the D^{*+} and the D^0, called Delta M. It is the most discriminating variable between signal and background, even if the candidate is only partially reconstructed. For signal candidates the peak is at $(145.42 \pm 0.01)\,\mathrm{MeV}/c^2$. Delta M distribution of figure 5.1 shows that the signal-like Minimum Bias candidates (blue) tend to gather more around the true value. This means that the BBDT correctly recognizes the signal candidates as signal. However, with a so soft BBDT output cut most candidates are still background.

It would be interesting to study the variables distributions obtained with a BBDT cut value of 0.41, the value that allows to get the same rate of the current trigger line. Unfortunately the available statistic for the Minimum Bias sample is small with respect to the absolute efficiency of this trigger, resulting in just about a hundred of selected candidates. Thus, we have to restrict ourselves to the choice of a softer BBDT output cut.

Figure 5.2 shows the same variables of Figure 5.1; in blue for candidates recognized by the BBDT as signal with a BBDT cut value > 0.3, in red the $D^{*+} \to D^0(K^+K^-\pi^+\pi^-)\pi_s^+$ Monte Carlo candidates. The Delta M distribution for the signal-like Minimum Bias candidates is correctly much more peaked at $(145.42 \pm 0.01)\,\mathrm{MeV}/c^2$

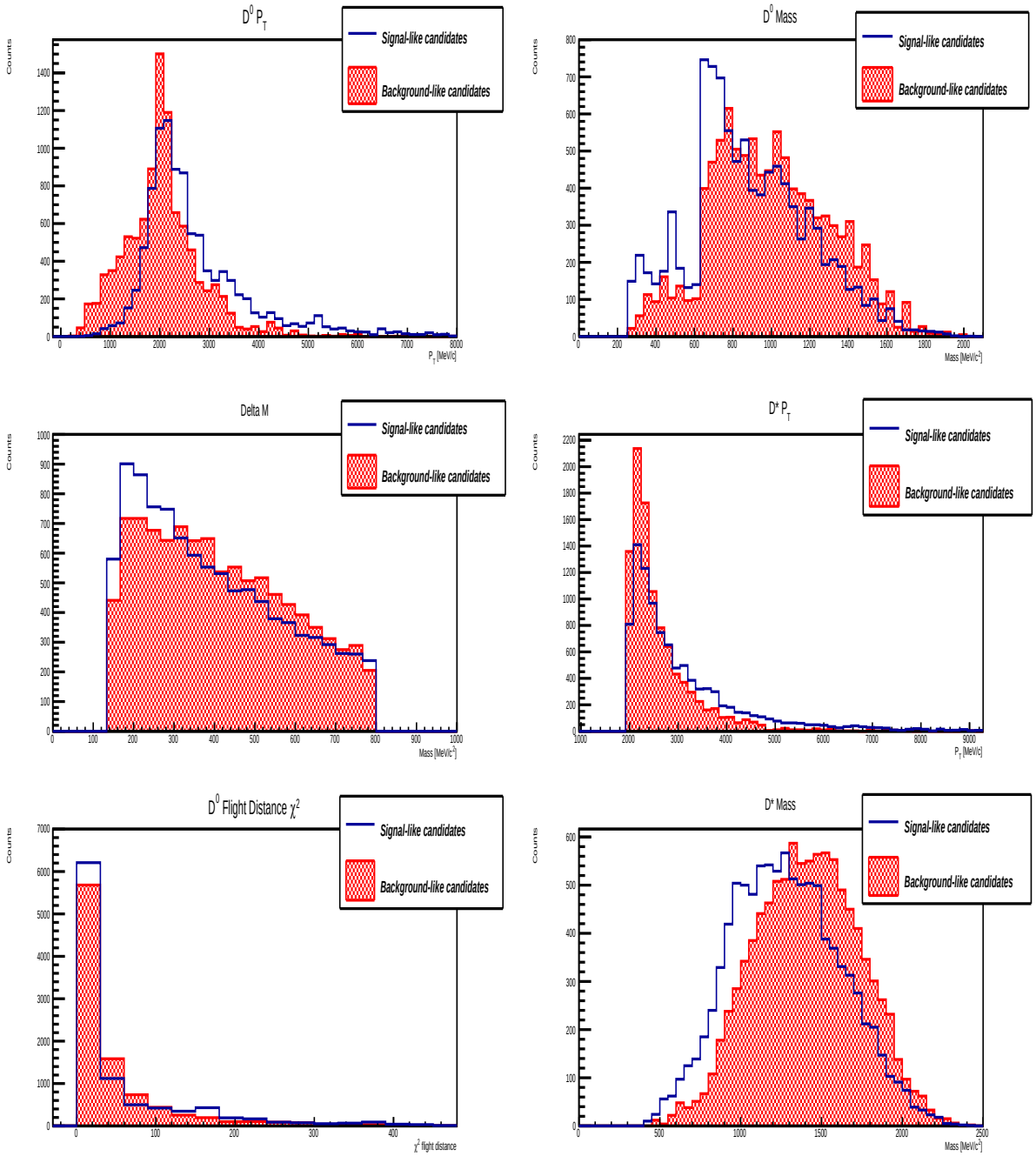

Figure 5.1: Variables distributions: in red for candidates recognized by the BBDT as background, BBDT cut value < 0 and in blue for candidates recognized as signal, BBDT cut value > 0. From top left, clockwise: D^0 p_T, D^0 mass, D^{*+} p_T, D^{*+} mass, D^0 flight distance χ^2 and Delta M between D^{*+} and D^0.

with respect to the BBDT cut > 0 sample. Background candidates are still present, in fact the Delta M Monte Carlo signal distribution is significantly more peaked at the true value. The presence of background candidates, which can be easily separated from signal, is necessary in order to be able to fit the discriminating variables distributions in the analysis phase.

A double peak appears in the D^0 p_T distribution, where, besides the expected peak at about $2\,\mathrm{GeV}/c$, another peak at about $4\,\mathrm{GeV}/c$ is visible. This trend in the D^0 p_T then leads to a similar behavior also in the D^{*+} p_T. This kind of distribution is due to the way we reconstruct the candidates, with only two tracks in the final state also for 3 and 4 bodies decay and to the use of the sum of the two tracks p_T as input variable. In fact in case of 3 and 4 bodies decay the D^0 is only partially reconstructed, thus the D^0 p_T is lower with respect to the 2 bodies decay modes, which are fully reconstructed. This is clearly visible in Figure 5.3, where the sum of the two tracks p_T is plotted for different decays modes. The BBDT, trained using the same proportion of candidates from each Monte Carlo signal sample, learns this kind of structure and reproduces it also in the selection of the candidates.

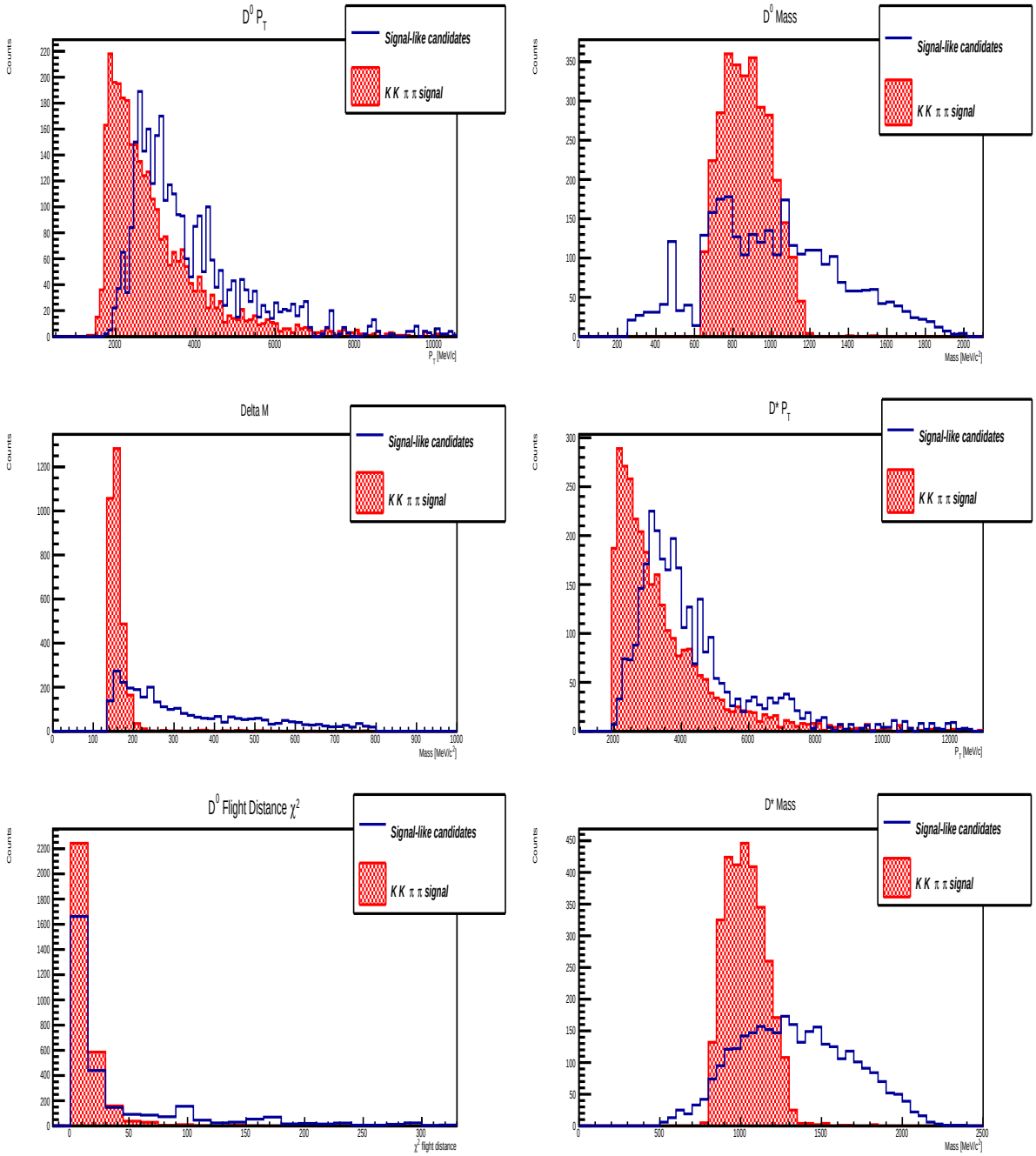

Figure 5.2: Variables distributions: in blue for candidates recognized by the BBDT as signal with a BBDT cut value > 0.3, in red the $D^{*+} \to D^0(K^+K^-\pi^+\pi^-)\pi_s^+$ Monte Carlo candidates. From top left, clockwise: D^0 p_T, D^0 mass, D^{*+} p_T, D^{*+} mass, D^0 flight distance χ^2 and Delta M between D^{*+} and D^0.

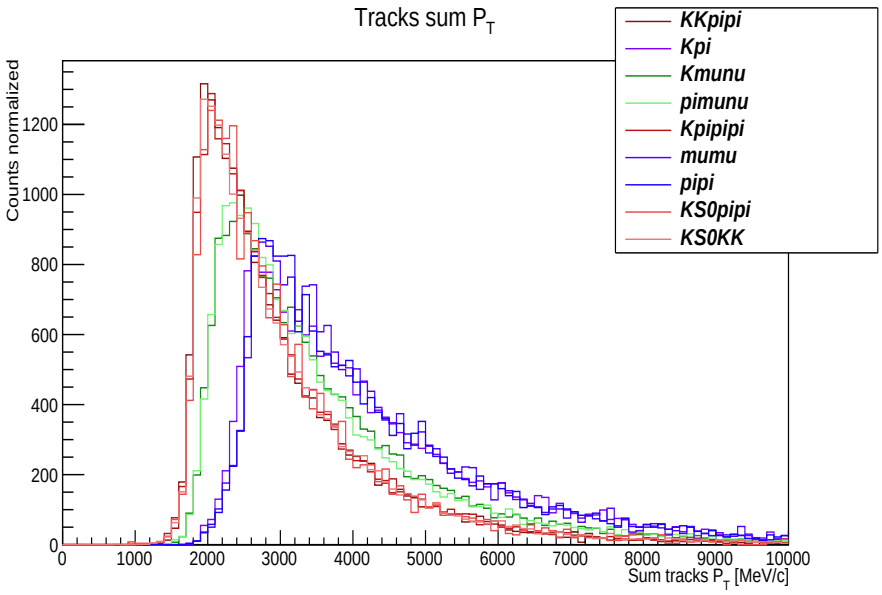

Figure 5.3: Sum of two tracks p_T for different decays modes. It is visible how the 2 bodies decays modes peak are at higher value with respect to the 3 bodies decays, which in turn are at higher value with respect to the 4 bodies ones.

Chapter 6

Conclusion

This thesis presented the development of a multivariate technique-based trigger for the inclusive selection of events with a D^{*+} meson at LHCb. This trigger will play an important role in measurements in the charm sector, such as the D^0 mixing and CP-violation parameters. With respect to the current trigger, which is based on a set of rectangular cuts, we decided to exploit the discrimination power of a multivariate technique.

We defined the event reconstruction strategy combining two tracks in the final state to make the D^0 vertex allowing for missing particles, to which a slow pion is added to form the D^{*+}. After the candidates reconstruction we introduced a set of preliminary cuts to decrease the combinatorial background. The final selection of the signal candidates is then performed by the multivariate tool Bonsai Boosted Decision Tree.

Exploiting 13 different Monte Carlo signal samples and a Minimum Bias background sample we tuned the preliminary cuts and studied their effect on the variables distributions. With our technique we have a very high background rejection, only $\sim 4‰$ of background candidates surivive, while almost 90% of the signal candidates are kept with no bias on the sample. Comparing the background and the signal variables distributions we then chose the best set of input variables for the BDT training, obtaining a good separation between signal and background in the training test. We then introduced the Bonsai Boosted Decision Tree algorithm and explained why it is fit-for-purpose for the on-line running conditions faced by a large-scale data acquisition system. With the BBDT training we got almost the same discrimination power that we obtained with the BDT. The trigger rate was studied as function of the BBDT output value. The efficiency on different signal samples as function of BBDT cut has been evaluated and the results are listed in Table 6.1

Selection	Absolute efficency wrt L0&HLT1			
	$D^0_{\mu\mu}$	$D^0_{K\pi\pi\pi}$	$D^0_{K^0_sKK}$	$D^0_{K\mu\nu_\mu}$
Preliminary cuts	0.86 ± 0.02	0.95 ± 0.02	0.90 ± 0.04	0.87 ± 0.04
BBDT cut 0.31	0.27 ± 0.01	0.45 ± 0.01	0.27 ± 0.02	0.27 ± 0.02
BBDT cut 0.35	0.17 ± 0.01	0.28 ± 0.01	0.17 ± 0.01	0.15 ± 0.01
BBDT cut 0.39	0.27 ± 0.01	0.15 ± 0.01	0.08 ± 0.01	0.08 ± 0.01
BBDT cut 0.41	$\mathbf{0.07 \pm 0.01}$	$\mathbf{0.10 \pm 0.01}$	$\mathbf{0.05 \pm 0.01}$	$\mathbf{0.05 \pm 0.01}$
BBDT cut 0.43	0.043 ± 0.004	0.052 ± 0.004	0.03 ± 0.01	0.02 ± 0.004
Current trigger	$\mathbf{0.120 \pm 0.003}$	$\mathbf{0.038 \pm 0.003}$	$\mathbf{0.020 \pm 0.001}$	$\mathbf{0.107 \pm 0.002}$

Table 6.1: Efficiency of HLT2 on different signal, $D^0_{\mu\mu}$ stands for $D^{*+} \to D^0(\mu^+\mu^-)\pi^+_s$, $D^0_{K\pi\pi\pi}$ for $D^{*+} \to D^0(K^+\pi^-\pi^+\pi^-)\pi^+_s$, $D^0_{K^0_sKK}$ for $D^{*+} \to D^0(K^0_s(\pi^+\pi^-)K^+K^-)\pi^+_s$, $D^0_{K\mu\nu_\mu}$ for $D^{*+} \to D^0(K^+\mu^-\nu_\mu)\pi^+_s$

The efficiencies on signal indicate that we built a trigger line more efficient for 4 bodies decays with respect to the current trigger and less efficient for 2 and 3 bodies decays. However, the efficiencies for 2 and 3 bodies decays are still quite comparable. This means that the technology we designed is competitive and it represents a good starting point from which start for a better optimization. These are the results of this preliminary study. We are studying other preliminary cuts and BBDT selections combinations in order to optimize the efficiency and the rate at the same time.

The implementation on the LHCb software through the look-up table, is ongoing. Once a stable and working version will be ready, we will get the efficiencies for the 2012 using the on-line reconstructed variables. Thus it will be possible to compare them to the current inclusive D^{*+} trigger without any bias due to the different reconstruction precision.

As soon as the 2015 Monte Carlo Minimum Bias and signal samples will be ready we will repeat all the studies presented in this thesis, in order to adapt the developed trigger line to the new conditions in which it will be implement. Both the preliminary cuts and the BBDT output cut will be optimized to obtain the trigger rate used in the next data taking.

Bibliography

[1] Y. Nir and N. Seiberg, Should squarks be degenerate?, Phys. Lett. B309 337, arXiv:hep-ph/9304307, 1993.

[2] M. Leurer, Y. Nir, and N. Seiberg, Mass matrix models: the sequel, Nucl. Phys. B420 468, arXiv:hep-ph/9310320, 1994.

[3] A. F. Falk et al., D0 D0 mass difference from a dispersion relation, Phys. Rev. D69 114021, arXiv:hep-ph/0402204, 2004.

[4] E. Golowich, J. Hewett, S. Pakvasa, and A. A. Petrov, Implications of $D^0 - \bar{D}^0$ mixing for new physics, Phys. Rev. D76 095009, arXiv:0705.3650, 2007.

[5] J P Baud et al. The LHCb Data Management System. J. Phys.: Conf. Ser. 396 032023, 2012.

[6] F. Halzen and A. D. Martin. Quarks & Leptons. John Wiley and Sons, 1984.

[7] Van Dyck Jr, Robert S., Paul B. Schwinberg, and Hans G. Dehmelt. "New high-precision comparison of electron and positron g factors." Physical Review Letters 59.1 (1987): 26.

[8] Augustin, J-E., et al. "Discovery of a Narrow Resonance in e+ e-Annihilation." Physical Review Letters 33.23 (1974): 1406.

[9] The LHCb Collaboration. CP violation in charm and beauty decays at LHCb. arXiv:1301.3082 [hep-ex], 2013.

[10] Particle Data Group Collaboration, C. Amsler et al., Particle physics summary tables, Phys. Lett. B667 (2008) 31 100.

[11] P. W. Higgs. Broken symmetries, massless particles and gauge fields. Phys. Lett., 12:132133, 1964.

[12] The ATLAS Collaboration. An update to the combined search for the Standard Model Higgs boson with the ATLAS detector at the LHC using up to 4.9 fb^{-1} of pp collision data at s = 7 TeV. ATLAS-CONF-2012-019, 2012.

[13] The CMS Collaboration. Combined results of searches for a Higgs boson in the context of the standard model and beyond-standard models. CMS PAS HIG-12-008, 2012.

[14] The ATLAS Collaboration. Evidence for the spin-0 nature of the Higgs boson using ATLAS data. arXiv:1307.1432 [hep-ex], 2013.

[15] T. Lee and C.-N. Yang, Question of Parity Conservation in Weak Interactions, Phys. Rev. 104, 254, 1956.

[16] R. Garwin, L. Lederman, and M. Weinrich, Observations of the Failure of Conservation of Parity and Charge Conjugation in Meson Decays: The Magnetic Moment of the Free Muon, Phys. Rev. 105, 1415, 1957.

[17] K. Nakamura et al. Review of Particle Physics. J. Phys. G., 37, 2011. 075021.

[18] G. Goldhaber et al., Phys. Rev. Lett. 37(1976) 265

[19] I. Peruzzi et al., Observation of a Narrow Charged State at 1876 MeV/c2 Decaying to an Exotic Combination of Kπ π. Phys. Rev. Lett. 37, 569, 1976

[20] J. H. Cristenson et al. Evidence for the 2π decay of the K_2^0 meson. Phys. Rev. Lett. 13:138140, 1964.

[21] The BaBar Collaboration. Evidence for $D^0 - \bar{D}^0$ Mixing. Phys. Rev. Lett. 98, 211802, 2007.

[22] The BELLE Collaboration. Evidence for $D^0 - \bar{D}^0$ Mixing. Phys. Rev. Lett. 98, 211803, 2007.

[23] The CDF Collaboration. Evidence for $D^0 - \bar{D}^0$ Mixing Using the CDF II Detector. Phys. Rev. Lett. 100, 121802, 2008.

[24] The LHCb Collaboration, Observation of $D^0 - \bar{D}^0$ Oscillations. Phys. Rev. Lett. 110, 101802, 2013.

[25] The LHCb Collaboration, Measurement of $D^0 - \bar{D}^0$ Mixing Parameters and Search for CP Violation Using $D^0 \to K^+\pi^-$ Decays. Phys. Rev. Lett. 111, 251801, 2013.

[26] The LHCb Collaboration, Measurements of Indirect CP Asymmetries in $D^0 \to K^-K^+$ and $D^0 \to \pi^-\pi^+$ Decays. Phys. Rev. Lett. 112, 041801, 2014.

[27] Lyndon Evans and Philip Bryant (editors). LHC Machine. JINST, 3, 2008. S08001.

[28] CERN: The European Organization for Nuclear Research. http://www.cern.ch.

[29] The ATLAS Collaboration. Luminosity Public Results. https://twiki.cern.ch/twiki/bin/view/AtlasPublic/LuminosityPublicResults.

[30] S. Chatrchyan et al. The CMS experiment at the CERN LHC. JINST, 3(S08004), 2008.

[31] G. Aad et al. The ATLAS Experiment at the CERN Large Hadron Collider. JINST, 3(S08003), 2008.

[32] K. Aamodt et al. The ALICE experiment at the CERN LHC. JINST, 3(S08002), 2008.

[33] A. Augusto Alves Jr et al. The LHCb Detector at the LHC. JINST, 3(S08005), 2008.

[34] LHCb Technical Design Report: Vertex Locator. CERN-LHCC-2001-011.

[35] LHCb Technical Design Report: Magnet. CERN-LHCC-2000-007.

[36] J. Gassner et al. Layout and Expected Performance of the LHCb TT Station. CERNLHCb-2003-140.

[37] LHCb Technical Design Report: Reoptimized Detector Design and Performance. CERN-LHCC-2003-030.

[38] LHCb Technical Design Report: Outer Tracker. CERN-LHCC-2001-024.

[39] A high-performance tracking system for the LHCb spectrometer. https://indico.cern.ch/conferenceDisplay.py?confId=149003

[40] N. Brook et al. LHCb RICH 1 Engineering Design Review Report. CERN-LHCb-2004-121, October 2005.

[41] M. Adinolfi et al. LHCb RICH 2 engineering design review report. CERN-LHCb-2002-009, March 2002.

[42] LHCb Technical Design Report: Calorimeters. CERN-LHCC-2000-036.

[43] LHCb Technical Design Report: Muon System. CERN-LHCC-2001-010.

[44] LHCb Technical Design Report: LHCb Trigger System. CERN-LHCC-2000-037.

[45] LHCb Online Technical Design Report. CERN-LHCC-2002-011, (2002).

[46] O. Callot and S. Hansmann-Menzemer, The forward tracking: Algorithm and performance studies, LHCb-2007-015 2007.

[47] F. Archilli et al., Performance of the Muon Identification at LHCb, JINST 8, 2013.

[48] The LHCb collaboration. The LHCb prompt charm triggers. arXiv:1311.7585v1 [hep-ex], 2013.

[49] The SLD Collaboration. A Measurement of R_b using a Vertex Mass Tag. arXiv:hep-ex/9708015v1 [hep-ex], 1997.

[50] R. Aaij et al., The LHCb trigger and its performance in 2011, JINST 8 (2013) P04022, arXiv:1211.3055.

[51] The LHCb collaboration. The LHCb trigger system: performance and outlook. PoS EPS-HEP2013 (2013) 504.

[52] PYTHIA. http://home.thep.lu.se/torbjorn/Pythia.html.

[53] TMVA 4. Toolkit for Multivariate Data Analysis with ROOT. arXiv:physics/0703039, 2009

[54] V. V. Gligorov and M. Williams. Efficient, reliable and fast high-level triggering using a bonsai boosted decision tree. arXiv:1210.6861v1, 2012.

[55] V. V. Gligorov, C. Thomas and M. Williams. The HLT inclusive B triggers. LHCb-PUB-2011-016, 2011.

[56] Plans for the Turbo stream and Tesla. http://indico.cern.ch/event/256184/session/1/contribution/5

[57] Roel Aaij and Johannes Albrecht. Muon triggers in the High Level Trigger of LHCb. LHCb-PUB-2011-017, 2011

[58] J. Albrecht, V. V. Gligorov, G. Raven, S. Tolk. Performance of the LHCb High Level Trigger in 2012. arXiv:1310.8544 [hep-ex], 2013